

See discussions, stats, and author profiles for this publication at: <https://www.researchgate.net/publication/336529361>

Transmission Line Model for Material Characterization using Terahertz Time-Domain Spectroscopy

Thesis · July 2019

DOI: 10.13140/RG.2.2.29689.21603

CITATIONS

0

READS

339

1 author:



Farah Vandrevala

University at Buffalo, State University of New York

17 PUBLICATIONS 48 CITATIONS

[SEE PROFILE](#)

Transmission Line Model for Material Characterization using Terahertz Time-Domain Spectroscopy

by

Farah Vandrevala

July 9, 2019

A dissertation submitted to the
faculty of the Graduate School of
the University at Buffalo, The State University of New York
in partial fulfillment of the requirements for the degree of

Doctor of Philosophy

Department of Electrical Engineering

Copyright by

Farah Vandrevala

© 2019

Acknowledgements

I am deeply grateful for the invaluable help and guidance of my Ph.D. advisor, Dr. Erik Einarsson, throughout my doctoral term. His advice and suggestions on my research and in the correct presentation of the results were integral to the work of this dissertation. His tireless and patient mentoring helped me navigate some of the tricky aspects of being a researcher, and will undoubtedly continue to help me in my future career.

I would like to thank Dr. Jonathan Bird, and Dr. Josep Jornet for agreeing to serve on my dissertation committee. Collaborating with them throughout my Ph.D. program provided me with helpful and critical reviews of my work. In addition, I would like to thank all administrative members of the Department of Electrical Engineering, especially Dr. Katharine Bartelo, whose support and encouragement helped me through some difficult times.

I am also appreciative of the help, support, and friendship of my fellow, current, and former group members, in addition to many other collaborators. Working and learning with them was a great pleasure.

Finally, none of this would have been possible without the support of my parents. I am particularly indebted to my mother, Mrs. Dinaz Vandrevala, for her unconditional acceptance and unwavering love. I owe my success to her faith in me.

Contents

Acknowledgements	iii
List of Figures	ix
List of Tables	x
Abstract	xi
1 Introduction	1
1.1 Terahertz time-domain system: An overview	2
1.1.1 THz generation and detection	2
1.1.2 THz-TDS data acquisition	4
1.2 THz-TDS measurement geometries	6
1.2.1 Transmission geometry	6
1.2.2 Reflection geometry	7
1.3 Motivation for this dissertation	8
2 Substrate Thickness Determination	11
2.1 Motivation	11
2.2 THz beam spot size measurement	12
2.3 Fractional Reflection Measurement Method	14
2.4 Conclusion	18
3 Substrate Parameter Extraction	20
3.1 Motivation	20

3.2	Time domain analysis	21
3.2.1	Estimating substrate parameters	21
3.2.2	Aligning the data in time	23
3.2.3	Windowing the time domain data	24
3.3	Frequency domain analysis	24
3.3.1	Fourier transform	24
3.4	Frequency calibration	27
3.5	Transfer function	29
3.6	Deriving the complex refractive index	30
3.7	Conclusion	33
4	Transmission Line Model	36
4.1	Complex reflection coefficients	37
4.2	Transmission line equivalent	38
4.3	Extracting material properties for bulk samples	39
4.3.1	Perfect dielectric	40
4.3.2	Lossy dielectric	42
4.3.3	Bulk conductors	43
4.3.4	Thin metal films	49
4.4	Conclusion	53
5	Graphene Characterization	54
5.1	Motivation	54
5.2	Graphene sample preparation: An overview	55
5.3	THz-TDS measurement of graphene	56
5.4	Extracting complex properties of graphene	56
5.5	Conductivity models	58
5.5.1	Kubo formalism	58
5.5.2	Drude model	61
5.5.3	Drude–Smith model	61
5.5.4	Real part fitting	63
5.6	Complex dielectric function extraction	64

5.7	Importance to graphene-based plasmonics	65
5.8	Conclusion	66
6	Conclusion	68
6.1	Thickness measurement application	69
6.2	Complete determination of material type	69
A	TAS7500TS THz-TDS Operating Procedure	71
B	Spot Size Measurement for the LiNbO₃ Emitter	77
C	Python Code	80
	Bibliography	96

List of Figures

1.1	Electromagnetic spectrum showing some THz spectroscopy applications, such as (clockwise from left) study of carrier dynamics in semiconductors and nanostructures, libration modes in water, and collective modes in proteins and amino acids [9].	2
1.2	THz pulse generation schemes [15]	3
1.3	THz pulse detection methods [15]	4
1.4	The Advantest TAS7500TS “turn-key” THz–TDS system.	5
1.5	THz light pulses, and femtosecond laser pulses at the detector	5
1.6	THz–TDS system in transmission geometry	6
1.7	THz–TDS in reflection geometry	9
2.1	Normalized intensity of the beam profile along the x -axis	13
2.2	Derivative of the normalized intensity of the beam profile along the x -axis. The solid line denotes the Gaussian fit.	14
2.3	Fractional reflection at substrate step-edge	15
2.4	Main, stage, and echo pulse positions for each edge	16
2.5	Calculated thickness for different substrates	17
2.6	SEM image of the cross-section of Si(LR) substrate, $L_{\text{avg}} = 305.1 \mu\text{m}$	18
3.1	Ray diagram showing reflections and key parameters of substrate illuminated by a THz beam from below.	21
3.2	Windowed time domain data for different substrates	25
3.3	Power spectrum of the different substrates	27
3.4	Phase spectrum of the different substrates	28

3.5	Reflectance spectrum for different substrates	29
3.6	Residual plot of peak and trough positions for different substrates	30
3.7	Transfer function for different substrates	31
3.8	Complex refractive index for different substrates	33
3.9	Complex dielectric function for different substrates	34
3.10	Dielectric function ratio for different substrates	34
4.1	Experimental setup for a sample on top of a substrate	37
4.2	Transmission line model with loads representing the interface of each side of the substrate	38
4.3	Complex reflection coefficients and complex impedance values for the air–substrate–air interfaces.	41
4.4	Complex dielectric function for substrate and air	42
4.5	Complex refractive index for substrate and air	43
4.6	Complex reflection coefficients and complex impedance for the substrate–water interface.	44
4.7	Complex dielectric function for water	45
4.8	Complex refractive index for water	46
4.9	Transmission line model for bulk metal on top of the substrate.	47
4.10	Input reactance variation with frequency [57]	47
4.11	Equivalent reactance seen by the incident THz wave depending on its wavelength . .	48
4.12	Comparison of refractive index of Si(HR) when extracted with respect to air at the back and with respect to Al mirror.	49
4.13	Experimental setup for a thin film on the substrate	50
4.14	Transmission line model for a thin-film at the substrate–air interface.	50
4.15	Complex reflection coefficients, and complex impedance for the substrate–nickel interface.	51
4.16	Complex conductivity of Ni.	52
4.17	Complex dielectric function of Ni.	53
5.1	Optical micrograph of two representative graphene samples	56
5.2	Raman spectra of two representative graphene samples	56
5.3	Ray diagram for THz light incident on the graphene-on-substrate system.	57
5.4	Transmission line model for graphene at the substrate–air interface.	57
5.5	Complex reflection coefficients of the two representative graphene samples	58

5.6	Complex impedance for the two representative graphene samples.	59
5.7	Complex conductivity for the two representative graphene samples.	60
5.8	Drude and Drude-Smith model fitting to extracted complex surface conductivity of Type A graphene.	62
5.9	Drude–Smith model fitting to only the real part of the extracted complex surface conductivity for the representative graphene samples.	64
5.10	Complex dielectric function for two representative graphene samples	65
5.11	Graphene bowtie antenna array designed to resonate at 1 THz	66
5.12	Electric field simulations for plasmon excitation in graphene patch antenna for different scattering times.	67
6.1	Time-domain spectroscopy and mapping measurement results	69
6.2	Complex impedances of different materials	70
A.1	Optical bench setup for all geometries	74
A.2	Adapter plates attached to the emitter and detector modules	75
A.3	Reflection base plate to be used in upside reflection geometry	75
A.4	Screenshot of successful initialization	76
B.1	Normalized intensity of the beam profile along the x -axis	78
B.2	The points are the derivative of the normalized intensity of the beam profile along the x -axis. The solid line denotes the Gaussian fit.	79

List of Tables

2.1	THz beam spot size for the 4 THz emitter	14
2.2	Substrate thickness	17
3.1	Substrate parameters from time-domain data	23
5.1	Extracted parameters for Type A graphene	63
5.2	Real part fitting parameters for both representative graphene samples	63
B.1	THz beam spot size for the 4 THz emitter	78

Abstract

Terahertz time-domain spectroscopy (THz-TDS) relies heavily on knowing precisely the thickness or the refractive index of a material. In practice, one of these values is assumed to be known, or their product is numerically optimized to converge on suitable values. Both approaches are prone to error, and may mask some real features or properties of the material being studied. To eliminate these errors, we use THz-TDS in reflection geometry to accurately and independently determine the thickness by illuminating the step-edge of a substrate atop a metal stage. This method relies solely on the relative time delay among two reflected pulses, and therefore forgoes the need for optimization or assumption of substrate parameters.

One of the biggest stumbling blocks of moving THz characterization out of research laboratories and into industrial applications is the oversimplification of the data analysis process, which requires prior knowledge of the material being dielectric or conductive. In this dissertation, we present a generalized transmission line model that enables fast determination of the material type for an unknown sample without making any prior assumptions. Moreover, it helps us understand the pseudo-dispersion effect seen in non-dispersive intrinsic substrates when they are terminated with a bulk conductor.

Extremely thin materials can have properties that are far superior to their bulk counterparts. Hence, two-dimensional materials are the focus of research efforts in the quest for novel devices. Graphene's ability to support surface plasmon polaritons (SPPs) in the THz frequency range is of particular interest in the design of nanoscale plasmonic antennas. Since a dielectric-conductor interface is required to excite and sustain SPPs, a negative dielectric function becomes a defining property for graphene, but proper graphene characterization is imperative to guide the antenna design, and evaluate its performance. We use THz-TDS to determine the complex dielectric function and related optical properties of graphene based on its extracted complex conductivity.

CHAPTER 1

Introduction

“One day, Sir, you will tax it.”

These were Michael Faraday’s words to the Chancellor of Exchequer when asked about the practical value of electricity. Not only was Michael Faraday right about mains electricity (typically, 50 or 60 Hz), but also the entire radio spectrum. In March of this year, the Federal Communications Commission created a new category of experimental licenses for use of frequencies between 95 GHz and 3 THz to allow companies to legally test and sell post-5G wireless technology equipment.¹ Until recently, terahertz (THz) technology has been more *taxing* than *taxable*. However, change is afoot.

According to [1], there is an annual growth rate between 9% and 21% in the number of publications and patent applications related to terahertz technology. This is a testament to the ongoing interest in a new generation of systems capable of coherent, time-domain, and time-resolved detection. Additionally, the global terahertz technology market is expected² to grow with a compound annual growth rate of 28.4%, from \$84.5 million in 2015 to \$491 million by 2022.

The terahertz frequency range, typically defined as being from 0.1 to 10 THz, contains several interesting interactions between light and matter in physical, chemical, and biological systems. The photon energies in this range are approximately from 0.4 to 40 meV. As seen in Figure 1.1, this makes the THz region particularly attractive for the study of systems having characteristic lifetimes in the picosecond range, such as the low-frequency dielectric relaxation of liquids [2,3], and hydrated

¹FCC to offer Experimental Licenses between 95 GHz and 3 THz, Medium.com, March 19, 2019.

²Terahertz Technology - Global Market Outlook (2016-2022) by Stratistics MRC

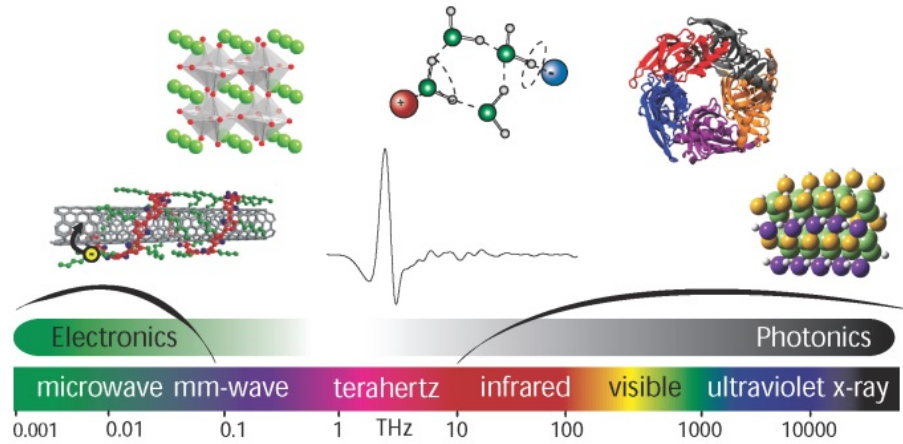


Figure 1.1: Electromagnetic spectrum showing some THz spectroscopy applications, such as (clockwise from left) study of carrier dynamics in semiconductors and nanostructures, libration modes in water, and collective modes in proteins and amino acids [9].

biological matter [4–6]. Moreover, there is growing interest in moving THz research from being purely scientific inside the laboratory to application-oriented in industry [1]. One example of this is using terahertz time-domain spectroscopy (THz-TDS) to monitor the thickness of paint during its drying process to optimize costs [7]. Many more applications and avenues of future research are discussed in [8].

1.1 Terahertz time-domain system: An overview

1.1.1 THz generation and detection

A major inflection point that led to THz research becoming more mainstream was the development of the femtosecond laser [10]. This paved the way for spectroscopy in the THz range through the use of photoconductive dipole antennas, or non-linear optics for the generation of ultra-short pulses of THz light [11]. Photoconductivity of semiconductors is one source of THz radiation [12]. In this process, when a femtosecond optical pulse is absorbed through inter-band transitions in a semiconductor, charge carriers are produced, which are then accelerated either by an externally applied dc electric field or through the built-in electric field in the semiconductor. The transient current that is formed emits THz radiation capable of propagating either on a transmission line or in free-space [13]. Another method of THz radiation generation is through optical rectification. In this method, a difference frequency is generated between the frequency components of an optical excitation pulse when it

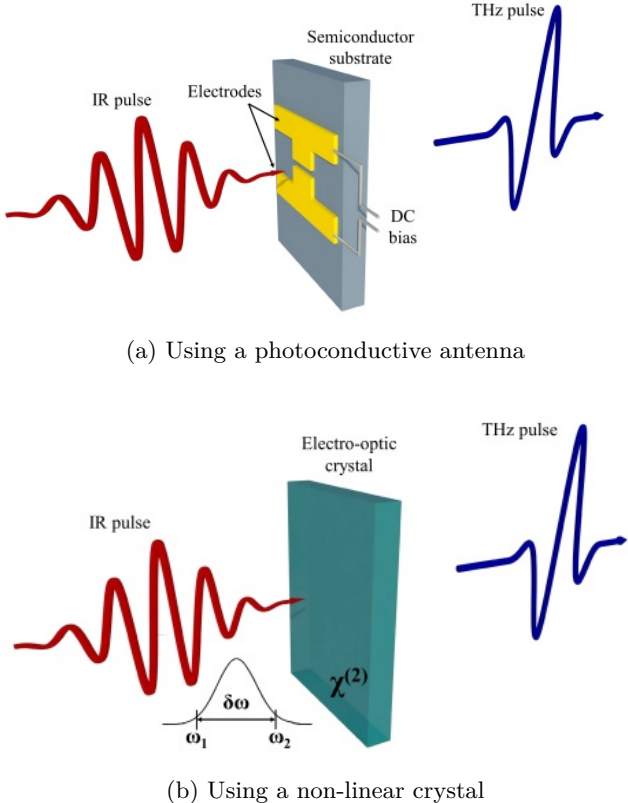


Figure 1.2: THz pulse generation schemes [15]

is passed through a non-centrosymmetric crystal. Since this process is non-resonant, the spectral bandwidth is only limited by the duration of the optical excitation pulse [14]. Figure 1.2 shows the two THz generation schemes.

Detection of THz radiation is very similar to the generation process, and therefore identical materials are used for the emitters and detectors. This is shown in Figure 1.3. In the case of photoconductive antennas, an optical probe pulse and a THz pulse interact simultaneously with a switch [16]. The probe pulse generates charge carriers and the THz pulse drives them to form a current. An electric field is generated when the optical probe pulse and THz pulse overlap, and the entire THz waveform can be obtained by sampling the time delay between the optical probe and THz pulses [17]. An alternate method of detection is through the electro-optic (EO) effect, which produces a birefringence in materials with inverted symmetry when biased by the electric field associated with the THz radiation [18]. The induced birefringence causes polarization of the optical probe beam to rotate. This is measured by the optical power transmitted by the EO crystal used in combination

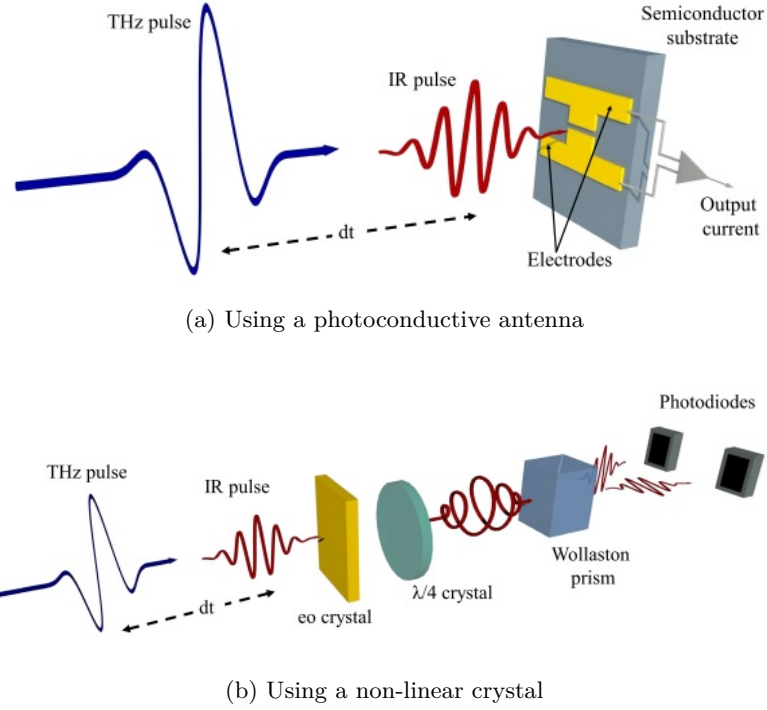


Figure 1.3: THz pulse detection methods [15]

with two crossed polarizers. The entire waveform is obtained through a similar sampling scheme to that used in the case of photoconductive detection [19].

1.1.2 THz-TDS data acquisition

In the Applied Nanomaterials Lab at the University at Buffalo, we host the Advantest TAS7500TS, which is a “turn-key” THz-TDS system shown in Figure 1.4. It consists of a 1550 nm infrared laser capable of emitting 50 fs pulses at a 50 MHz repetition rate. The THz detector is a GaAs photoconductive antenna. The THz emitter is either an InGaAs photoconductive antenna with an operating range of 0.1 to 4 THz, or a LiNbO₃ waveguide, which provides a spectral range of 0.5 to 7 THz. The operating principle for signal acquisition is the same, regardless of the emitter type. Typically, the train of pulses emitted by the femtosecond laser is split in two parts: one part is used to excite THz radiation in the emitter while the other part is used as a gate signal on the detector [20]. Our system, though, has two synchronized lasers, both of which generate femtosecond pulses, but with a repetition rate of one carefully tuned with respect to the other. This controls the time delay of the pulse arrival at the detector. The detector will sense the incident THz radiation



Figure 1.4: The Advantest TAS7500TS “turn-key” THz–TDS system.

only during the time period of the femtosecond pulse. By measuring the THz field $E_{\text{THz}}(t)$ at different time instants, i.e., at different arrival times of the femtosecond pulses, and connecting the independent measurements together, we can reproduce the shape of the THz pulse [21]. This is shown in Figure 1.5. The accuracy of this method relies on having precise synchronization between the THz field and the femtosecond pulses used to gate the detector. Since this optical sampling measures the time-varying electric field of the THz pulse, and not merely its intensity, the measurement is sensitive only to the coherent radiation, which is phase-locked to the repetition rate of the femtosecond laser. Therefore, the sampling is not affected by thermal radiation, and THz detection can be achieved at room temperature [21].

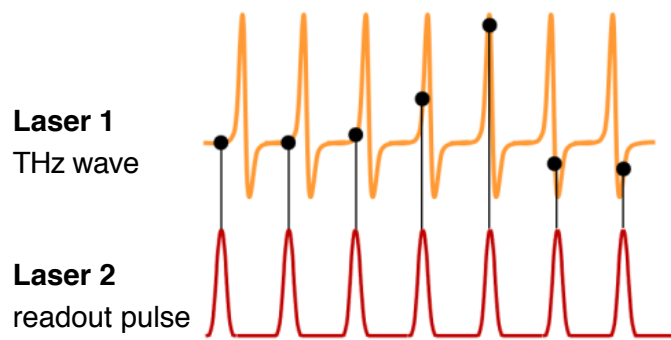


Figure 1.5: THz light pulses, and femtosecond laser pulses at the detector

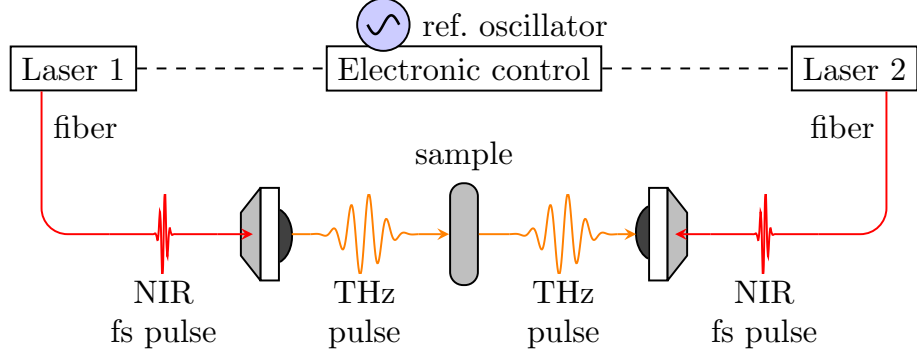


Figure 1.6: THz-TDS system in transmission geometry

1.2 THz-TDS measurement geometries

1.2.1 Transmission geometry

The most popular method for performing THz-TDS measurements is to use the transmission geometry as shown in Figure 1.6. In this setup, the sample under test is placed directly in the path of the THz beam. In order to extract the material properties, the following transfer function is constructed using the reference signal, \tilde{E}_r , which travels the same path in the absence of the substrate, and the THz signal, \tilde{E}_s obtained after it has interacted with the substrate [22]:

$$\frac{\tilde{E}_s}{\tilde{E}_r} = \frac{4\tilde{n}_s\tilde{n}_0}{(\tilde{n}_{\text{sam}} + \tilde{n}_0)^2} \exp\left[-j\frac{\omega}{c}L_s(\tilde{n}_s - \tilde{n}_0)\right] \text{FP}(\omega), \quad (1.1)$$

where

$$\text{FP}(\omega) = \left[1 - \left(\frac{\tilde{n}_s - \tilde{n}_a}{\tilde{n}_s + \tilde{n}_0}\right)^2 \exp\left(-2j\frac{\omega}{c}\tilde{n}_s L_s\right)\right]^{-1}. \quad (1.2)$$

L_s and \tilde{n}_s are the thickness and complex refractive index of the substrate respectively, and \tilde{n}_0 is the complex refractive index for air. $\text{FP}(\omega)$ represents the Fabry-Pérot interference effect that arises in the substrate due to multiple internal reflections [23]. If the sample is a layer on top of the substrate, then the transfer function takes the general form shown below [7]:

$$\frac{\tilde{E}_s}{\tilde{r}} = \tilde{t}_{01}\tilde{P}_1\tilde{t}_{12}\tilde{P}_2\tilde{t}_{23}\text{FP}_{123}, \quad (1.3)$$

where complex transmission coefficients going from layer j to layer k are given by

$$\tilde{t}_{jk} = \frac{2\tilde{n}_j}{\tilde{n}_j + \tilde{n}_k}. \quad (1.4)$$

The propagation through layer j is defined as an exponentially decaying function of its thickness d_j and complex refractive index \tilde{n}_j so that,

$$\tilde{P}_j = \exp\left(-j\frac{\omega}{c}d_j\tilde{n}_j\right). \quad (1.5)$$

The Fabry–Pérot etalon caused by the partial reflection of M internally reflected pulses is

$$\text{FP}(\omega) = \sum_{m=0}^M (\tilde{r}_{kl}\tilde{P}_k\tilde{r}_{jk}\tilde{P}_k)^m, \quad (1.6)$$

where the complex reflection coefficients are given by

$$\tilde{r}_{jk} = \frac{\tilde{n}_j - \tilde{n}_k}{\tilde{n}_j + \tilde{n}_k}. \quad (1.7)$$

Several studies [24–27] have described various numerical optimization routines to extract substrate and/or sample properties with high accuracy using the above equations. Since normal incidence is typically used in transmission geometry, polarization of the incident light is unimportant, simplifying the data analysis. However, the limitation of this geometry is that the samples need to be fairly transparent in the THz regime. Consequently, highly absorbing or highly conductive samples cannot be measured with this setup.

1.2.2 Reflection geometry

The reflection geometry allows for the material under test to be highly absorbing or highly reflective. In this geometry, there are three ways of probing the sample:

Attenuated total reflection A sample sits atop a prism, and the THz beam interacts with the sample at the prism–sample interface via total internal reflection. This is known as attenuated total reflection (ATR) since the evanescent field of the THz pulse penetrates into the sample. For this analysis, the transfer function is formed by taking the ratio of the reflected signal from the prism

interface when it is in contact with the sample to the reflected signal obtained when the interface is in contact with air [11]. While the ATR technique is best-suited for the characterization of highly absorbing dielectrics, such as water [28], it requires the sample to be in direct contact with the prism, which can impose some practical limitations.

Upside reflection In this configuration, the THz beam directly hits the sample placed on top of the substrate or the stage. This method is good for characterizing optically dense samples, such as highly-doped semiconductors [29]. In this method, a reference measurement is obtained by reflecting the THz beam from a metal mirror, whose reflection coefficient is taken to be $\tilde{r}_{\text{metal}} = -1$, and a transfer function is created as follows [11]:

$$\tilde{r}_{\text{sam}} = \frac{\tilde{n}_{\text{sam}} - 1}{\tilde{n}_{\text{sam}} + 1}. \quad (1.8)$$

This configuration has also been used to measure metal–graphene hybrid films. Here the reference measurement was taken to be the bare side of the substrate on which the sample was deposited. The following transfer function was used to extract the complex conductivity of the metal–graphene hybrid film [30]:

$$\tilde{R} = \frac{1 - Z_0 \frac{\tilde{\sigma}_f}{1 - \tilde{n}_s}}{1 - Z_0 \frac{\tilde{\sigma}_f}{1 + \tilde{n}_s}}. \quad (1.9)$$

Underside reflection In this configuration, the THz beam goes through the substrate and interacts with the sample at the substrate–sample interface. We adopt this method in the work presented in this dissertation, and explain it in detail in the subsequent chapters. We will show that this geometry is not limited by the opacity of the material. Our THz–TDS setup is shown in Figure 1.7

1.3 Motivation for this dissertation

The non-contact and nondestructive nature of THz–TDS is making it a popular choice for characterizing the electrical properties of materials ranging from two-dimensional crystals [31, 32] to biological samples [33, 34]. Although the transmission geometry is more commonly used, the reflection geometry is needed for the study of highly absorbing or highly reflective materials. In such applications, samples are typically placed atop substrates such as quartz or high-resistivity silicon, and their

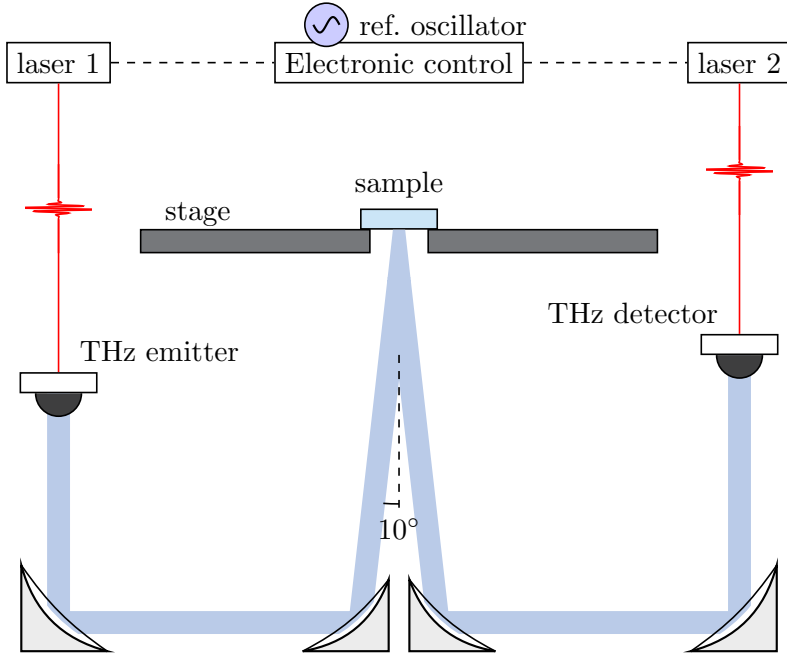


Figure 1.7: THz-TDS in reflection geometry

characteristics are determined by studying the light–matter interaction at the substrate–sample interface [35]. One can then ascertain the complex optical properties of the sample material through equations that depend on the substrate thickness and its complex refractive index. Consequently, accurate knowledge of both these values is necessary to correctly isolate the sample properties from those of the underlying substrate.

Since THz-TDS measures the electric field in the time domain, an imprecise value of the substrate thickness can cause errors to cascade into sample property calculations related to the detected phase [11]. In this dissertation, we demonstrate an experimental technique whereby the substrate thickness can be determined with high accuracy without making any assumptions about the substrate properties, and without using complicated numerical optimization routines. As a consequence of *independently* determining the thickness, we are then able to calculate the optical properties of the substrate with high confidence. This new technique can be easily applied to a wide range of substrates, and still yield precise results regardless of how transparent or opaque the substrate is. This technique is particularly advantageous when the effects of the supporting substrate must be carefully accounted for, such as applications involving the study of coatings, biological samples, thin-films, and two-dimensional materials.

1.3 Motivation for this dissertation

One of the biggest stumbling blocks of moving THz science and technology out of research laboratories and into industrial applications is the oversimplified analysis scheme wherein material-specific inputs are needed, which might often be unknown [36]. To mitigate the need to know specific properties, such as whether the sample under test is a dielectric or conductor, we introduce a transmission line model to extract the complex impedance of the sample based on reflection of the THz pulse obtained after interaction. Here we show that the calculations needed to extract sample properties from this complex impedance are considerably simpler than the Fresnel coefficient based equations currently used, yet provide an equivalent description of the system. Moreover, we will show how the phase information contained in THz-TDS measurements enables us to characterize the material more thoroughly than is possible using other spectroscopic or non-spectroscopic methods. Finally, we demonstrate the importance of proper characterization of a two-dimensional material using the above techniques in the context of plasmonic applications.

CHAPTER 2

Substrate Thickness Determination

2.1 Motivation

Numerical algorithms have traditionally been used to optimize the values of substrate thickness L_{sub} , refractive index n_{sub} , and extinction coefficient κ_{sub} [24–26]. Alternatively, L_{sub} can be assumed constant while n_{sub} is calculated [37], or n_{sub} can be kept fixed while computing L_{sub} [38]. More recent methods, proposed to minimize errors in parameter extraction resulting from substrate thickness variations, take one of the following approaches: assume that the substrate dielectric properties are known and calculate a calibration factor to account for beam displacement [39], perform a baseline calibration using a reference sample and substrate [40], or use substrates of different thicknesses to account for errors [41]. These techniques rely on assumptions of n_{sub} and/or L_{sub} , or require multiple iterations to arrive at values that numerically minimize a chosen error function.

In this chapter, we demonstrate the first experimental method in which we *independently* determine the substrate thickness without making any assumptions. We do this by illuminating the step-edge of a substrate—which sits atop a metal stage—to obtain three reflections. One reflection comes from the stage, while the other two come from the top and bottom surfaces of the substrate itself. The time delay between the first two reflections yields the substrate thickness completely independent of the refractive index. Unlike the method used in [42], which can only work for semi-transparent substrates, our method is also suitable for heavily doped substrates that are highly reflective, moderately doped substrates that are absorptive, and optically transparent insulators.

2.2 THz beam spot size measurement

According to [43], having a collimated beam for measurement is preferred because it avoids errors introduced by the Guoy shift [44]. However, the optical bench of our setup is designed with focusing mirrors, therefore we take the approach described below. For this measurement, we use the photoconductive antenna-based THz emitter having a spectral range of 0.1 to 4 THz. Parabolic mirrors guide the *p*-polarized beam such that it is made incident onto a horizontal sample stage at an angle of $\theta_i = 10^\circ$ from normal and focused at the surface.

To determine the spot size of the focused THz beam, we used the imaging capability of our THz-TDS system to measure the beam profile. We took four measurements described below with a stainless steel razor blade covering one half of the 10 mm hole as we scanned the stage along the positive and negative directions for both the *x*- and *y*- axes. This method, known as the knife-edge method, is a standard technique for determining the spot size of an electromagnetic beam [45]. Assuming that the THz beam has a radially symmetric Gaussian profile, its intensity can be described as:

$$I(x, y) = I_{\max} \exp \left(-2 \frac{(x - x_0)^2 + (y - y_0)^2}{r^2} \right), \quad (2.1)$$

where I_{\max} is the maximum intensity of the beam, (x_0, y_0) are the coordinates corresponding to the center of the beam, and r is the beam radius defined as the *x*-coordinate corresponding to I_{\max}/e^2 . Figure 2.1 shows the normalized intensity profile of the beam for both positive and negative scan directions along the *x*-axis. Similar results were obtained while scanning the stage along the *y*-axis. The normalized intensity profile measured using the blade in a given direction for the *x*-axis is described as [45],

$$I_N(x) = \frac{I(x)}{I_x} = \frac{1}{2} \left[1 \pm \operatorname{erf} \left(\sqrt{2} \frac{(x - x_0)}{r} \right) \right], \quad (2.2)$$

where erf is the error function defined as,

$$\operatorname{erf}(z) = \frac{2}{\sqrt{\pi}} \int_0^z e^{-t^2} dt \quad (2.3)$$

2.2 THz beam spot size measurement

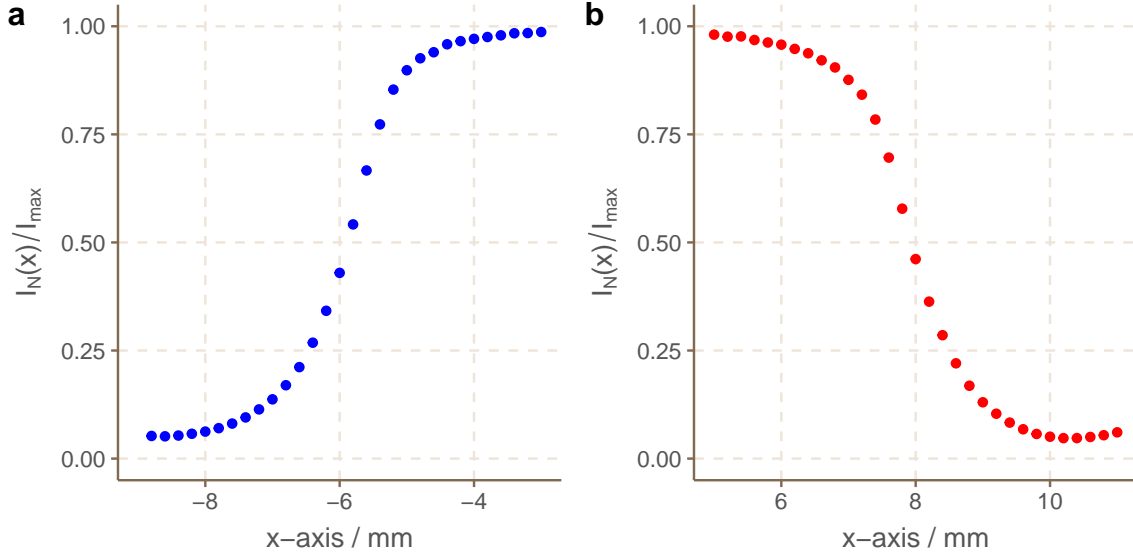


Figure 2.1: Normalized intensity of the beam profile along the x -axis

and its derivative is given by,

$$\frac{d}{dz} \text{erf}(z) = \frac{2}{\sqrt{\pi}} e^{-t^2}. \quad (2.4)$$

Taking the derivative of the normalized intensity function yields,

$$\frac{dI_N(x)}{dx} = \frac{1}{r} \frac{2}{\sqrt{\pi}} \exp \left[-2 \frac{(x - x_0)^2}{r^2} \right]. \quad (2.5)$$

This result is plotted in Figure 2.2 for the beam profile along the x -direction. A similar result is obtained for the beam profile along the y -direction. From this derivative plot, there are two ways to find the beam diameter, $2r$ [46]:

- 1) By fitting a Gaussian function corresponding to the above form, and extracting x_0 and r .
- 2) By taking the difference between the x -coordinates corresponding to the $\frac{1}{e^2}$ points of the derivative plot.

The extracted beam spot size, which will be $2r$, obtained by both methods is found to be very similar, as summarized in Table 2.1.

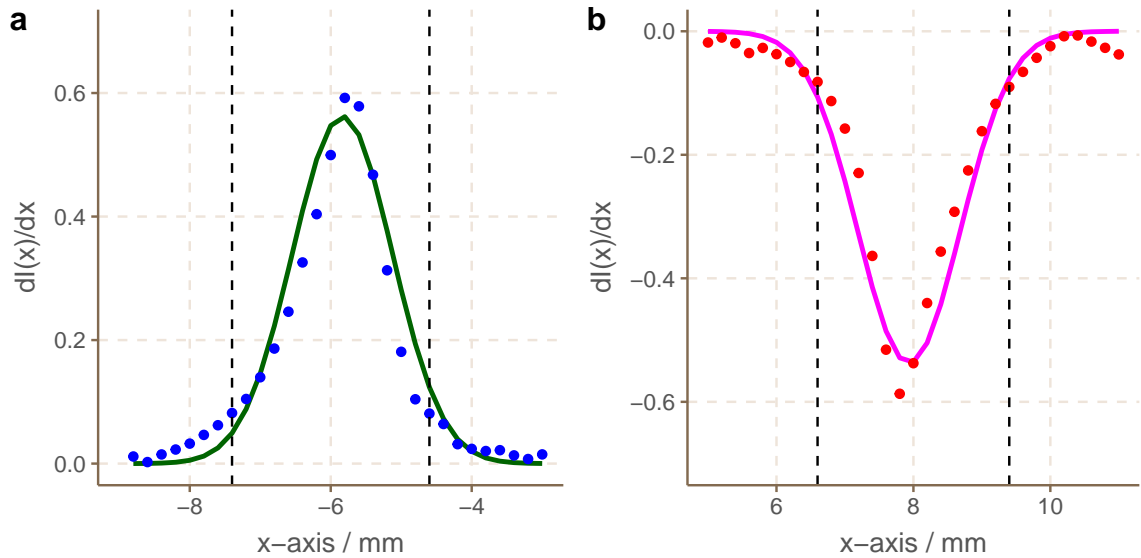


Figure 2.2: Derivative of the normalized intensity of the beam profile along the x -axis. The solid line denotes the Gaussian fit.

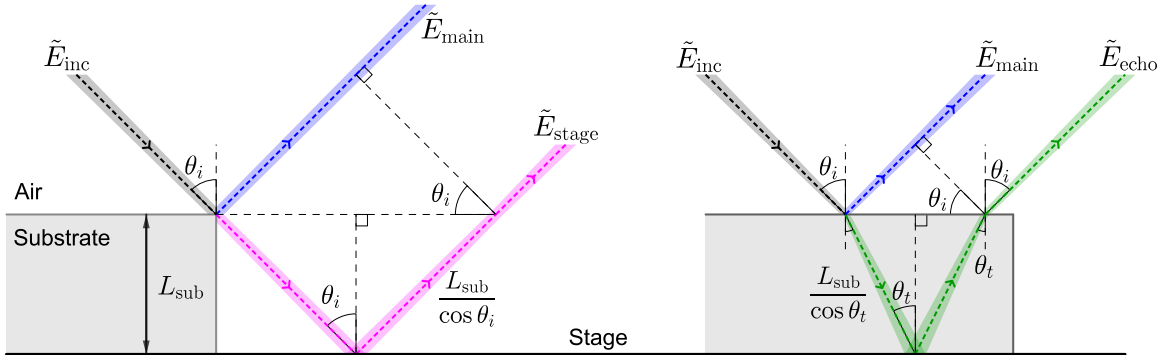
Table 2.1: THz beam spot size for the 4 THz emitter

Scan direction	Gaussian fit	$\frac{1}{e^2}$ coordinates
	$2r$ / mm	$2r$ / mm
$+x$ axis	2.90	2.80
$-x$ axis	2.80	2.80
$+y$ axis	2.80	2.60
$-y$ axis	2.90	2.80
Average	2.85	2.75

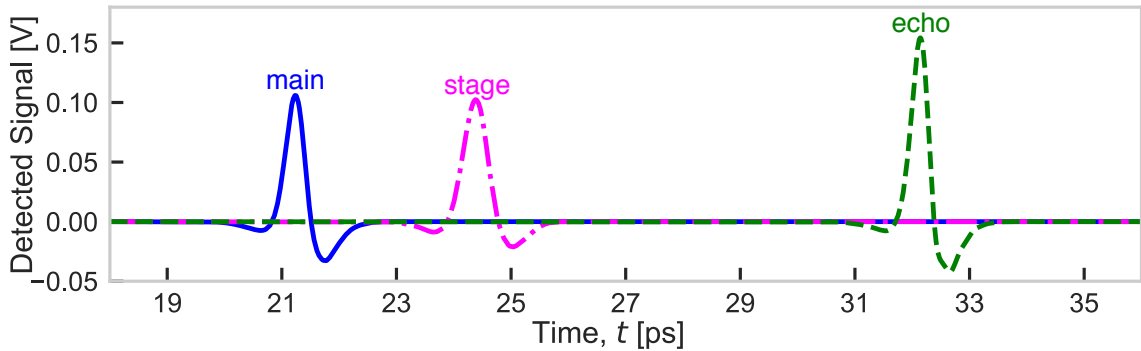
2.3 Fractional Reflection Measurement Method

In our THz-TDS system, the 50 fs light pulses coming from the 1550 nm infrared laser at a 50 MHz repetition rate excite a photoconductive antenna. This generates a THz beam consisting of pulses having a spectral range of 0.1 to 4 THz. Parabolic mirrors guide the p -polarized beam such that it is made incident onto a horizontal sample stage at an angle of $\theta_i = 10^\circ$. We adjust the vertical

2.3 Fractional Reflection Measurement Method



(a) Ray diagram showing the THz beam path outside the substrate (left) and inside the substrate (right)



(b) THz time-domain measurement showing the main, stage, and echo reflections

Figure 2.3: Fractional reflection at substrate step-edge

position of the stage so that the beam is focused to a spot size of approximately 3 mm on the sample or substrate surface.

The left side of Fig. 2.3a shows the part of the beam that travels outside the substrate, whereas the right side of Fig. 2.3a shows the part of the beam that propagates through the interior of the substrate. As seen in Figure 2.3b, the first detected pulse (main) is the reflection from the top surface of the substrate, whereas the second pulse (stage) is the reflection from the metal stage. The third pulse (echo) is due to the portion of the incident THz beam that propagates inside the substrate, eventually being reflected from the substrate-stage interface. Figure 2.4 shows these pulse positions for different substrates.

Since neither the main nor stage pulse travels through the substrate, the time delay between their arrival at the detector is completely independent of the substrate refractive index. From the time

2.3 Fractional Reflection Measurement Method

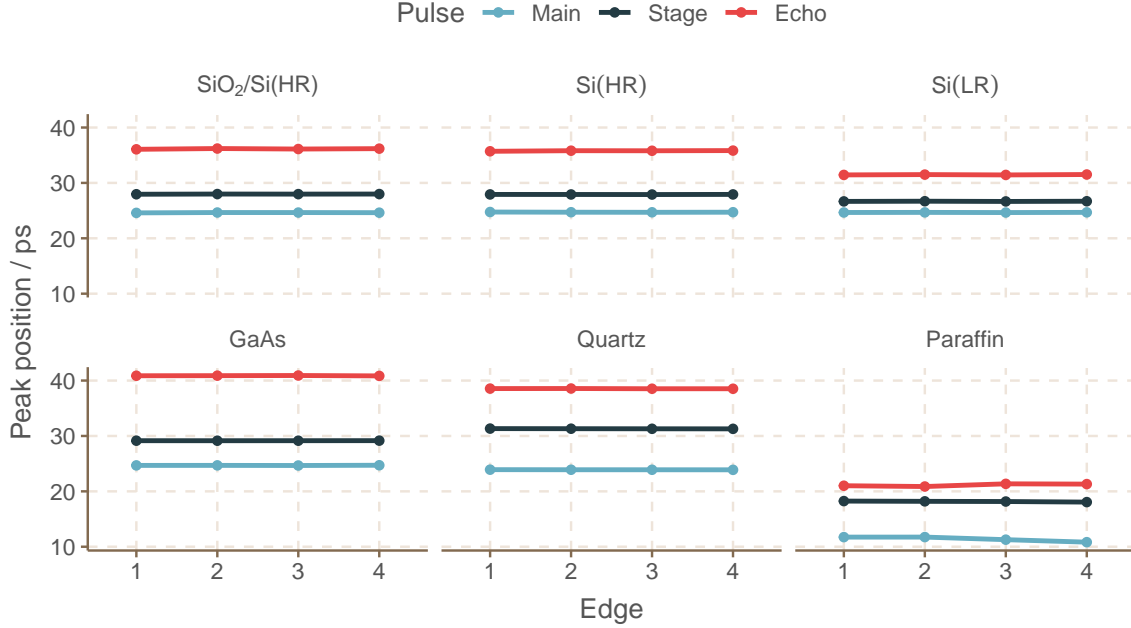


Figure 2.4: Main, stage, and echo pulse positions for each edge

difference in the positions of the main and stage pulses, we can calculate the substrate thickness as:

$$\Delta t_{\text{stage-main}} = D_{\text{stage}} \frac{n_{\text{air}}}{c} - D_{\text{main}} \frac{n_{\text{air}}}{c}, \quad (2.6)$$

where D is the distance traveled by the THz pulse. Assuming $n_{\text{air}} = 1$,

$$c \Delta t_{\text{stage-main}} = \frac{2L_{\text{sub}}}{\cos \theta_i} - \frac{2L_{\text{sub}}}{\cos \theta_i} \sin^2 \theta_i, \quad (2.7)$$

$$= \frac{2L_{\text{sub}}}{\cos \theta_i} (1 - \sin^2 \theta_i), \quad (2.8)$$

$$= \frac{2L_{\text{sub}}}{\cos \theta_i} \cos^2 \theta_i, \quad (2.9)$$

$$= 2L_{\text{sub}} \cos \theta_i. \quad (2.10)$$

Therefore,

$$L_{\text{sub}} = \frac{c \Delta t_{\text{stage-main}}}{\cos \theta_i}. \quad (2.11)$$

In the above calculations, we have considered the optical path difference between the stage and

2.3 Fractional Reflection Measurement Method

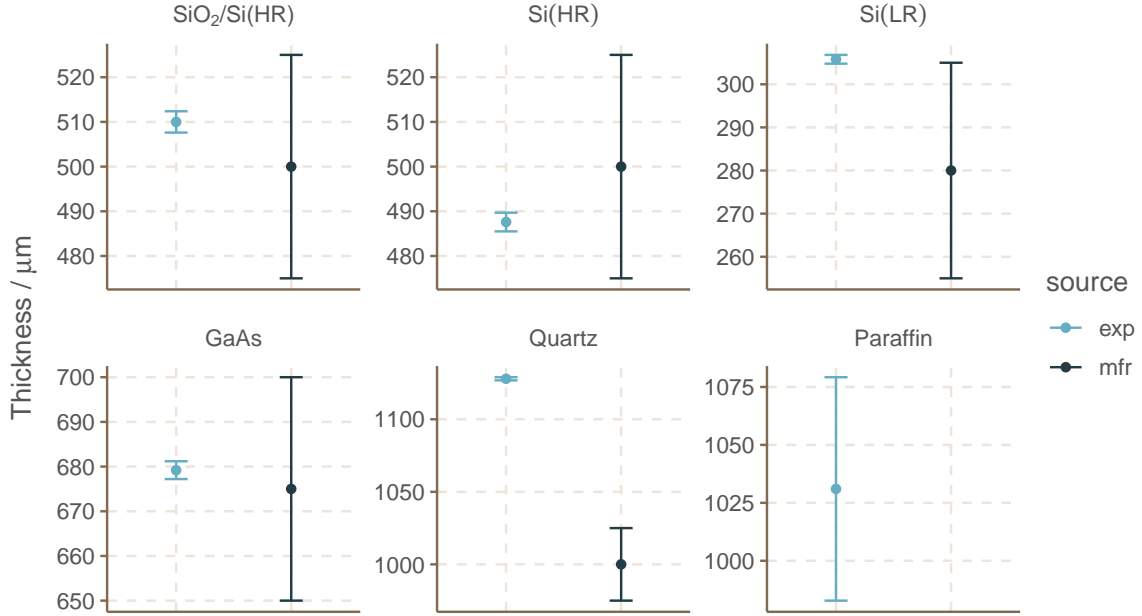


Figure 2.5: Calculated thickness for different substrates

main pulses in equation (2.7) to be from the point where the THz beam reflects from the top of the substrate to the point where both beams have the same wavefront [39].

Using this method, we calculate the thickness for the different substrates. Figure 2.5 shows the variation in thickness measured along each edge, and Table 2.2 shows the average value and standard deviation for each substrate. The large standard deviation observed for paraffin is because the sample thickness was not uniform.

Table 2.2: Substrate thickness

Substrate	Manufacturer L_{sub} (μm)		Measured L_{sub} (μm)	
	Given	Std. Dev.	Mean	Std. Dev.
SiO ₂ /Si(HR)	500	25	510.0	2.383
Si(HR)	500	25	487.6	2.094
Si(LR)	280	25	305.8	1.019
GaAs	675	25	679.2	1.992
Quartz	1000	25	1127.9	1.088
Paraffin	NA	NA	1031.0	48.204

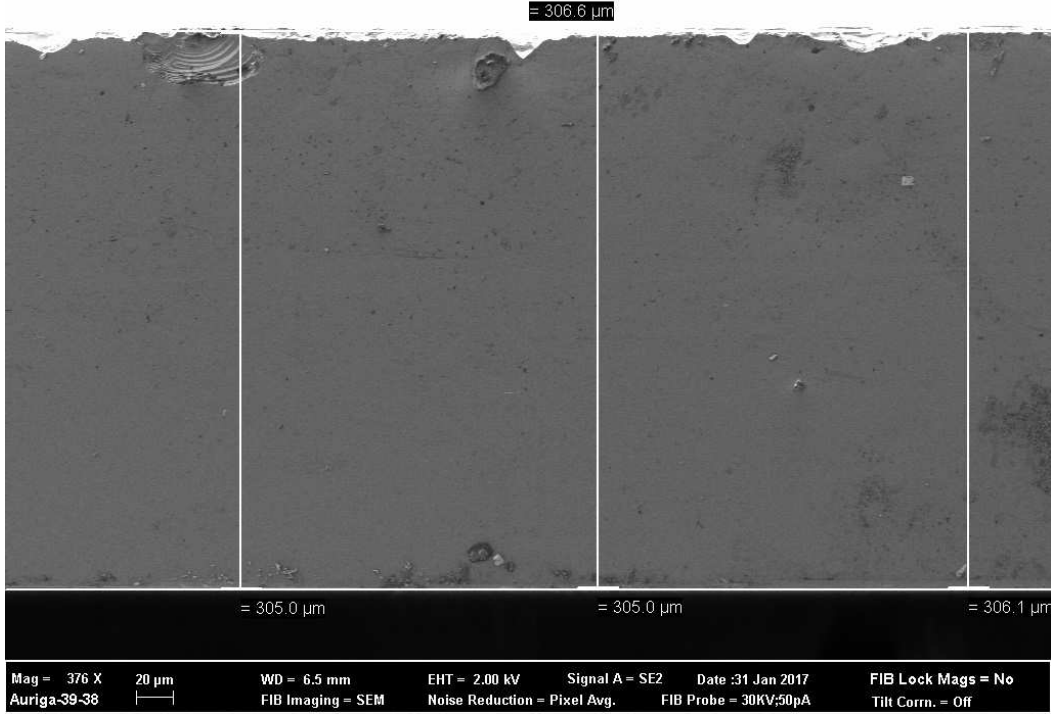


Figure 2.6: SEM image of the cross-section of Si(LR) substrate, $L_{\text{avg}} = 305.1 \mu\text{m}$

We used scanning electron microscopy (SEM) to independently verify the substrate thickness by imaging and measuring the cross-section. Figure 2.6 shows, as an example, the SEM images for the Si(LR) substrate. The average values of the measured thickness under SEM closely matches the average values shown in Table 2.2.

2.4 Conclusion

The results shown in Figure 2.5 and summarized in Table 2.2 demonstrate that the fractional-reflection measurement, taken at the step-edge of a substrate, allows us to decouple thickness and refractive index measurements using THz-TDS. Our approach does not require any numerical optimization routines. It is also applicable to a wide range of substrates and will yield accurate results despite unknown or uncertain doping levels.

2.4 Conclusion

Using these independently determined values, the optical properties of the substrate itself can be calculated with high confidence. This is critical when the effects of the supporting substrate must be carefully accounted for, such as when studying soft matter, like water, or two-dimensional materials, like graphene.

CHAPTER 3

Substrate Parameter Extraction

3.1 Motivation

Several studies [38, 47, 48] have shown that inaccuracies in the substrate properties, particularly, the uncertainty regarding its thickness, can cause the errors to propagate while extracting the sample properties. In Chapter 2, we showed that we can extract the substrate thickness with high confidence in its value because our fractional measurement at the step-edge is completely independent of the substrate's refractive index. Using this known thickness, we can now characterize the substrates which are typically used in THz-TDS measurements.

To find the substrate refractive index, we use a self-referenced method, like the one described in [39], wherein the substrate is illuminated with the THz beam as depicted in Figure 3.1. The following analysis will be based on the two reflected beams measured after the incident THz pulse has interacted with the substrate. The first measured reflection, \tilde{E}_{main} , is that of the incident THz beam \tilde{E}_{in} at the air–substrate interface. The second measured reflection, \tilde{E}_{echo} , is that of the portion of the THz beam that propagates inside the substrate, eventually being reflected at the other substrate–air interface.

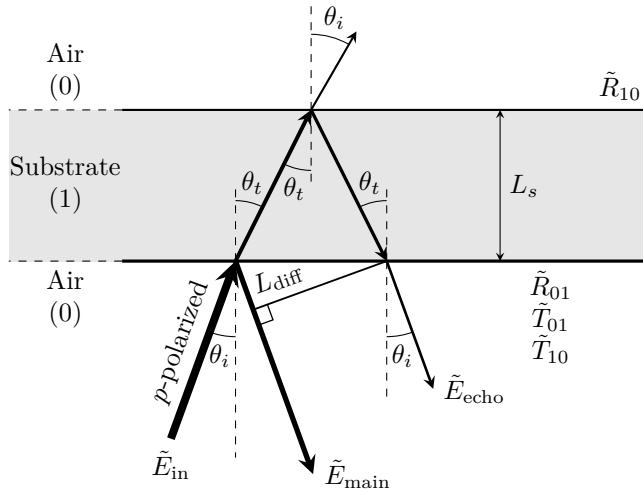


Figure 3.1: Ray diagram showing reflections and key parameters of substrate illuminated by a THz beam from below.

3.2 Time domain analysis

In this section, we will use the raw time-domain data to estimate the substrate parameters, and decouple the two reflected pulses before transforming the data to the frequency domain.

3.2.1 Estimating substrate parameters

The time delay at the detector between the main and echo pulses depends on the substrate thickness and refractive index. Since we have independently determined the substrate thickness, we can determine the contribution from the refractive index only, which can be calculated as follows:

$$\Delta t_{\text{echo-main}} = D_{\text{echo}} \frac{n_s}{c} - D_{\text{main}} \frac{n_a}{c}. \quad (3.1)$$

Here, D is the distance traveled by each pulse from the substrate surface to the point where the both have the same wavefront.

$$c \Delta t_{\text{echo-main}} = n_s \frac{2L_s}{\cos \theta_t} - \frac{2L_s}{\cos \theta_t} \sin \theta_t \sin \theta_i. \quad (3.2)$$

3.2 Time domain analysis

According to Snell's Law,

$$n_a \sin \theta_i = n_s \sin \theta_t \quad (3.3)$$

$$\frac{\sin^2 \theta_i}{n_s^2} = \sin^2 \theta_t = 1 - \cos^2 \theta_t, \quad (3.4)$$

$$\cos^2 \theta_t = 1 - \frac{\sin^2 \theta_i}{n_s^2}, \quad (3.5)$$

$$\cos \theta_t = \frac{\sqrt{n_s^2 - \sin^2 \theta_i}}{n_s}. \quad (3.6)$$

Therefore,

$$c\Delta t_{\text{echo-main}} = n_s \frac{2L_s}{\cos \theta_t} - n_s \frac{2L_s}{\cos \theta_t} \sin^2 \theta_t, \quad (3.7)$$

$$= n_s \frac{2L_s}{\cos \theta_t} (1 - \sin^2 \theta_t), \quad (3.8)$$

$$= n_s \frac{2L_s}{\cos \theta_t} \cos^2 \theta_t, \quad (3.9)$$

$$= 2L_s n_s \cos \theta_t, \quad (3.10)$$

$$c\Delta t_{\text{echo-main}} = 2L_s \sqrt{n_s^2 - \sin^2 \theta_i} \quad (3.11)$$

$$\left(\frac{c\Delta t_{\text{echo-main}}}{2L_s} \right)^2 = n_s^2 - \sin^2 \theta_i. \quad (3.12)$$

We can determine the refractive index using the following equation:

$$n_s = \sqrt{\left(\frac{c\Delta t_{\text{echo-main}}}{2L_s} \right)^2 + \sin^2 \theta_i}. \quad (3.13)$$

The angle of refraction can be calculated from the time delay as:

$$\Delta t_{\text{echo-main}} = 2L_s n_s \cos \theta_t, \quad (3.14)$$

$$\cos \theta_t = \frac{\Delta t_{\text{echo-main}}}{2L_s n_s}, \quad (3.15)$$

$$\theta_t = \cos^{-1} \left(\frac{\Delta t_{\text{echo-main}}}{2L_s n_s} \right). \quad (3.16)$$

This yields the effective substrate thickness

$$L_{\text{eff}} = L_s \cos \theta_t. \quad (3.17)$$

The results of these calculations for three separate substrates are summarized in Table 3.1. Since the angle of refraction inside the substrate is very small, the effective substrate thickness is very similar to the actual value measured using the method described in Chapter 2.

Table 3.1: Substrate parameters from time-domain data

Parameter	SiO ₂ /Si(HR)	Si(HR)	Si(LR)
$L_s(\mu\text{m})$	510.00	472.20	305.80
n_s	3.33	3.38	3.29
$\theta_t(\text{deg})$	2.99	2.95	3.02
$L_{\text{eff}}(\mu\text{m})$	509.31	471.57	305.37

3.2.2 Aligning the data in time

The next step in the data analysis procedure is to shift the time domain data such that the main pulse of all measurements are aligned in time. This is done either with respect to the pulse position of the reference pulse (usually taken to be the reflection obtained from a metal mirror) or the first reflection of the substrate measurement.

While this step is not as important for the substrate characterization because it is a self-referencing method, it is crucial when characterizing a sample placed on top of the substrate. By aligning the main pulse for the substrate and sample measurements, we are ensuring that any phase difference observed between the substrate and sample echo pulses is not due to some misalignment or positioning error of the substrate. In frequency domain, this will translate to the following:

$$\arg[\tilde{H}_{\text{sam}}] - \arg[\tilde{H}_{\text{sub}}] = [\phi_{\text{sam}}^{\text{echo}} - \phi_{\text{sam}}^{\text{main}}] - [\phi_{\text{sub}}^{\text{echo}} - \phi_{\text{sub}}^{\text{main}}]. \quad (3.18)$$

Only if $\phi_{\text{sam}}^{\text{main}} = \phi_{\text{sub}}^{\text{main}}$, then

$$\arg[\tilde{H}_{\text{sam}}] - \arg[\tilde{H}_{\text{sub}}] = \phi_{\text{sam}}^{\text{echo}} - \phi_{\text{sub}}^{\text{echo}}. \quad (3.19)$$

3.2.3 Windowing the time domain data

A Hann window function, centered at the peak position of each pulse, is applied to the time domain data to separate the main and echo pulses. The shape of the Hann window is found to significantly reduce spectral leakage, and minimize noise from the THz-TDS system and water vapor [49].

The Hann window function is defined as a special case of the Tukey window function [50] described as follows:

$$W(t) = \begin{cases} \frac{1}{2} \left(1 + \cos \left(\frac{2\pi}{r} \left[t - \frac{r}{2} \right] \right) \right), & 0 \leq t < \frac{r}{2} \\ 1, & \frac{r}{2} \leq t < 1 - \frac{r}{2} \\ \frac{1}{2} \left(1 + \cos \left(\frac{2\pi}{r} \left[t - 1 + \frac{r}{2} \right] \right) \right), & 1 - \frac{r}{2} \leq t \leq 1 \end{cases} \quad (3.20)$$

For $r = 1$, the above function returns a Hann window function defined as:

$$W(t) = \frac{1}{2} \left(1 - \cos \left(\frac{2\pi t}{M-1} \right) \right), \quad (3.21)$$

where $M = \Delta t$ is the window length. Adding the separated main and echo pulse data, and their respective window functions, results in the plot shown in Figure 3.2.

3.3 Frequency domain analysis

Since a narrow pulse in time domain becomes a broad spectrum in frequency domain, we transform the time domain data into frequency domain. The Fourier transform of a temporal waveform gives its spectral distribution in frequency domain.

3.3.1 Fourier transform

In general, a periodic function $F(t)$ in the time domain is defined as

$$F(t) = A \cos(\omega t + \phi), \quad (3.22)$$

where A is the amplitude, $\omega = 2\pi f$ is the frequency, and ϕ is the phase angle of the signal. Since THz light is an electromagnetic wave, which is time-varying, we can express the electric field in time

3.3 Frequency domain analysis

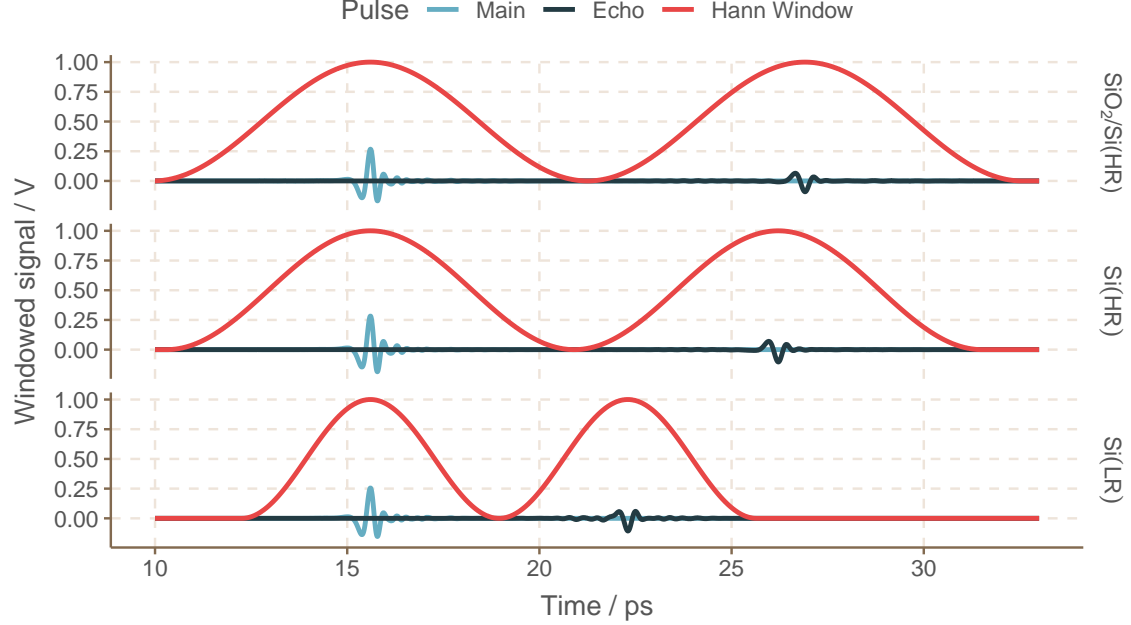


Figure 3.2: Windowed time domain data for different substrates

domain as

$$E(t) = E_0 \cos(\omega t - \tilde{\beta} L_{\text{sub}}), \quad (3.23)$$

where $\tilde{\beta} = \frac{\omega}{c} \tilde{n}_{\text{sub}}$ is the wave vector. In complex form, this time-varying electric field can be written as,

$$E(t) = \text{Re} [\tilde{\mathbf{E}} e^{j\omega t}], \quad (3.24)$$

where, $\tilde{\mathbf{E}}$ is the time-independent *phasor* of the instantaneous function $E(t)$. The Fourier transform extracts this phasor function when it converts the time domain signal into frequency domain. Therefore, the electric field in frequency domain is

$$\tilde{\mathbf{E}}(\omega) = E_0 \exp\left(-j \frac{\omega}{c} \tilde{n}_{\text{sub}} L_{\text{sub}}\right). \quad (3.25)$$

In the Python programming language, which we used for the data analysis (see Appendix C), the Fourier transform is defined as:

$$\tilde{\mathbf{E}}(f) = \sum_{t=0}^{N-1} E(t) \exp\left(-j \frac{\omega t}{N}\right), \quad (3.26)$$

3.3 Frequency domain analysis

where $N = 2^{16} = 65536$ is the total number of points in the time domain data. Since the time domain data is real, the `np.fft.rfft` function is used, and the transformed data is then scaled by the length of the time domain array.

Since the electric field is measured, the amplitude and phase information can be extracted from the Fourier transform as shown in the equations below.

The general form of the Fourier transformed data is

$$\tilde{\mathbf{E}}(\omega) = E_0 \exp\left(-j\frac{\omega}{c}\tilde{n}L_{\text{eff}}\right), \quad (3.27)$$

where, $\tilde{n} = n - j\kappa$ is the complex refractive index of the medium, and L_{eff} = effective distance traveled inside the medium. The electric field phasor can be expressed in terms of its magnitude and argument as follows:

$$|\tilde{\mathbf{E}}| \exp(-j\phi) = E_0 \exp\left(-\frac{\omega}{c}\kappa L_{\text{eff}}\right) \exp\left(-j\frac{\omega}{c}nL_{\text{eff}}\right). \quad (3.28)$$

The magnitude of the electric field is

$$|\tilde{\mathbf{E}}| = E_0 \exp\left(-\frac{\omega}{c}\kappa L_{\text{eff}}\right), \quad (3.29)$$

and the phase (in radians) is

$$\phi = \frac{\omega}{c}nL_{\text{eff}}. \quad (3.30)$$

The Log of the power P (in dB) is given by

$$\log(P) = 10 \log_{10}(|\tilde{\mathbf{E}}|^2). \quad (3.31)$$

The frequency domain transformations of the measured time domain signal for different substrates are shown in Figures 3.3 and 3.4.

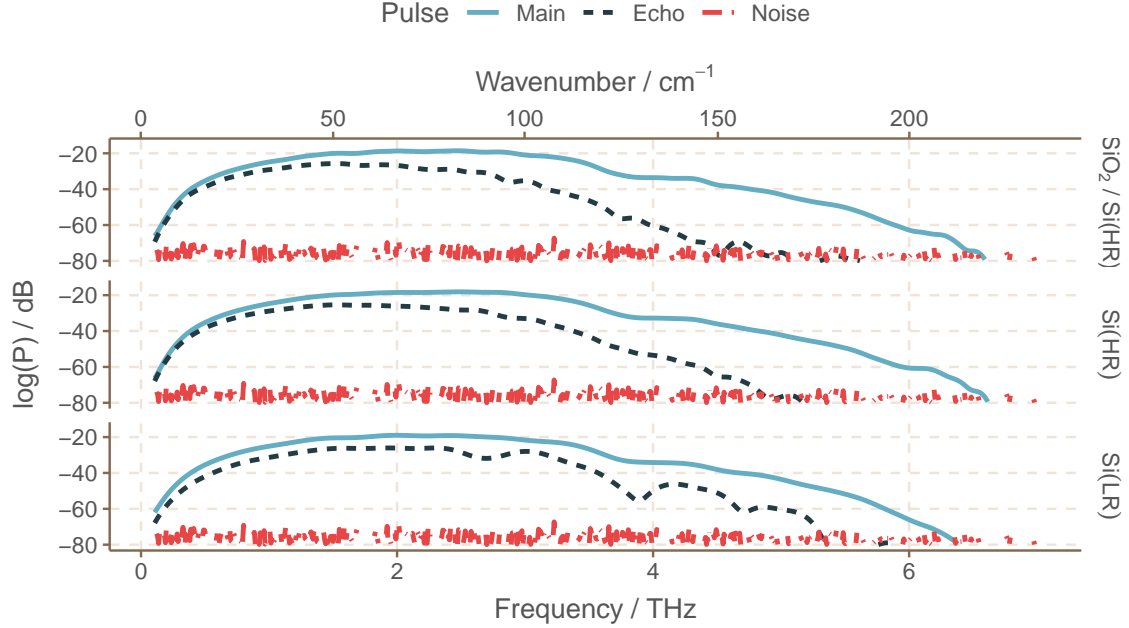


Figure 3.3: Power spectrum of the different substrates

3.4 Frequency calibration

Due to the Fabry–Pérot effect, wherein multiple reflections are obtained from a substrate for the same incident THz pulse, the substrate acts like an etalon. According to [51], using the uniformly spaced peaks of this interference effect in the frequency domain is an accurate and reliable way to verify the frequency scale of a time-domain system.

The interference arising from reflection at the air–substrate and substrate–air interfaces are extracted from the reflectance spectrum, which is calculated as described below:

$$R = \frac{|\tilde{\mathbf{E}}_2|^2}{|\tilde{\mathbf{E}}_1|^2}, \quad (3.32)$$

where

$|\tilde{\mathbf{E}}_2|$ is the magnitude of the THz electric field reflected from the substrate, and

$|\tilde{\mathbf{E}}_1|$ is the magnitude of the THz electric field reflected from an Al mirror used as reference. This is shown in Figure 3.5.

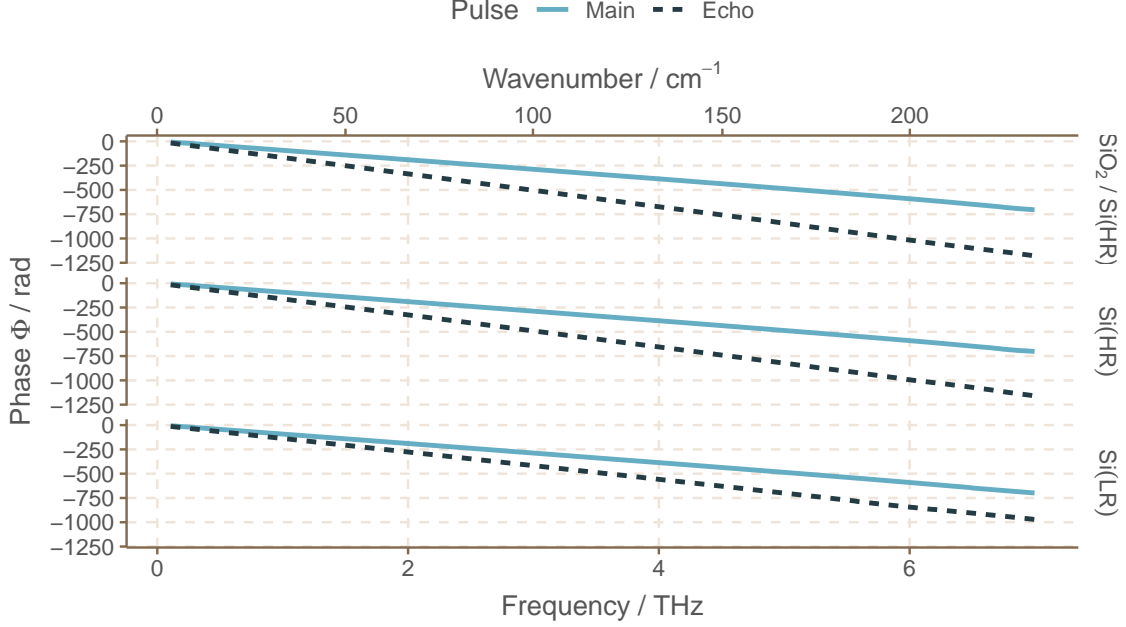


Figure 3.4: Phase spectrum of the different substrates

The frequencies at which peaks occur are given by [51]

$$f_p = \frac{c}{2n_{\text{sub}}L_{\text{eff}}} M, \quad (3.33)$$

and troughs occur at

$$f_t = \frac{c}{2n_{\text{sub}}L_{\text{eff}}} \left(M + \frac{1}{2} \right), \quad (3.34)$$

where, in our case, $L_{\text{eff}} = L_{\text{sub}} \cos \theta_t$, and M is the peak/trough order. The difference between the extracted frequency positions and the expected values are plotted with respect to the calculated frequency position. This yields the residual plot seen in Figure 3.6.

A residual point is the deviation of each data point from the predicted value. In Figure 3.6, the maximum residual observed between the extracted and calculated peak/trough positions is less than 7.6 GHz, which is the frequency resolution of our THz-TDS system. Given that the difference is so small, it implies that the peak/trough positions can be determined with very high accuracy, and whatever small deviations exist is largely due to the effect of digitizing the signal [51].

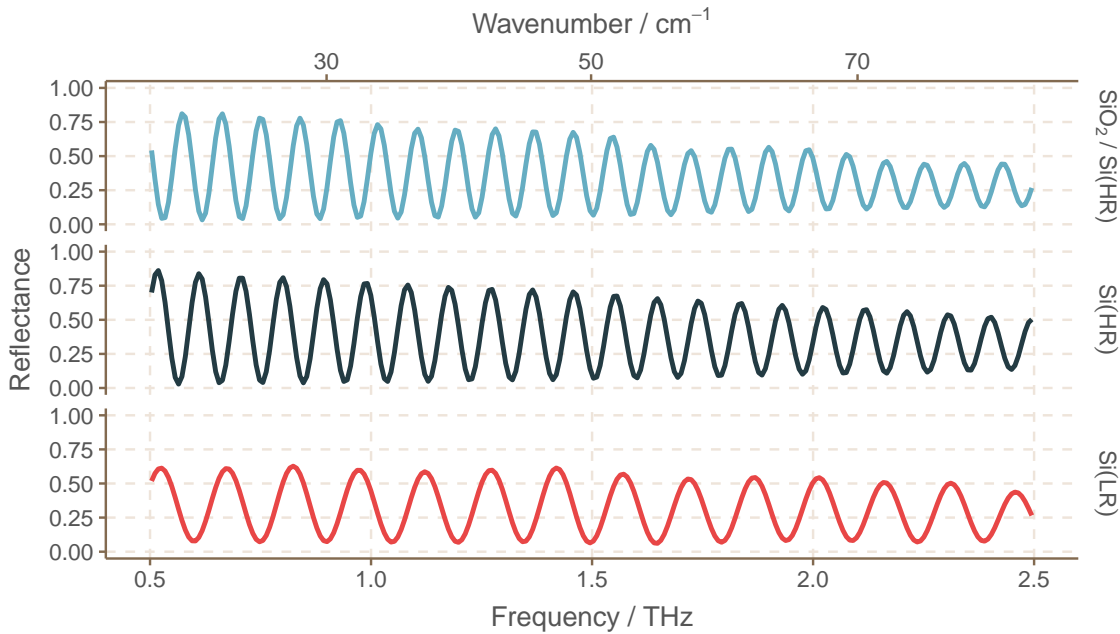


Figure 3.5: Reflectance spectrum for different substrates

3.5 Transfer function

When an electromagnetic wave propagates through a medium, it undergoes two changes:

- 1) Due to the refractive index of the medium, its speed decreases. This manifests as a time delay in time-domain, or analogously, as a phase difference in frequency domain.
- 2) Its amplitude attenuates, however slightly, due to some amount of loss inside the medium.

To compare how the THz electric field was modified after interaction with the substrate, we construct a transfer function \tilde{H} using the main pulse as the input and the echo pulse as the output as follows:

$$\tilde{H} = \frac{\tilde{\mathbf{E}}_{\text{echo}}}{\tilde{\mathbf{E}}_{\text{main}}} = \frac{|\tilde{\mathbf{E}}_{\text{echo}}|}{|\tilde{\mathbf{E}}_{\text{main}}|} \exp(-j[\Phi_{\text{echo}} - \Phi_{\text{main}}]). \quad (3.35)$$

In the following section we will see that the argument of this transfer function is related to the refractive index of the substrate, which causes the phase delay, whereas the magnitude is related to the extinction coefficient, which causes the amplitude attenuation.

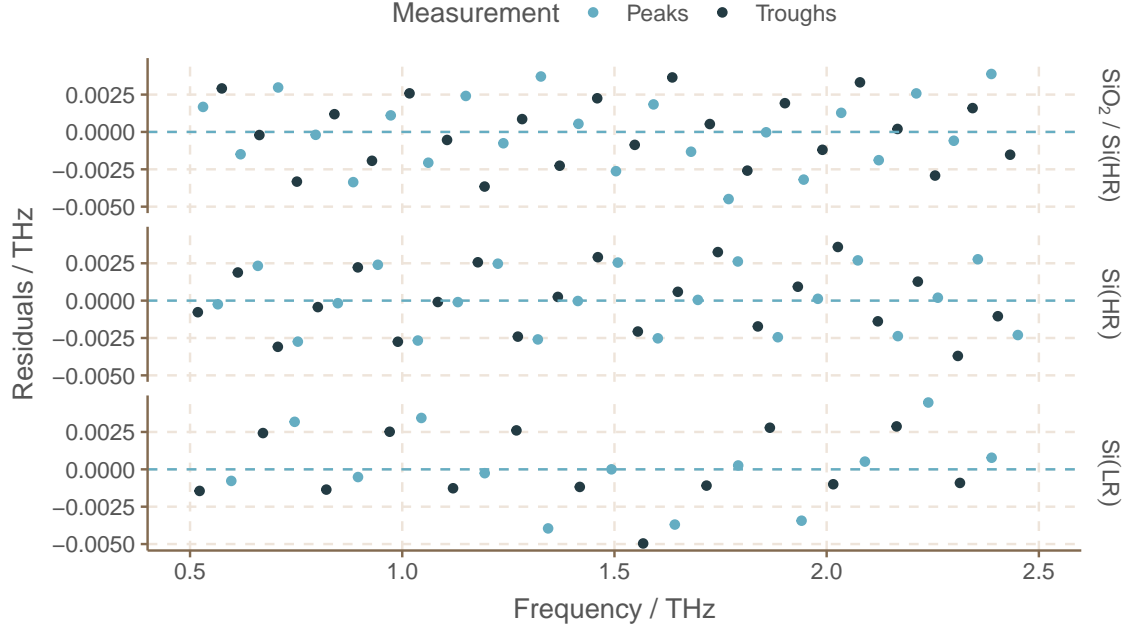


Figure 3.6: Residual plot of peak and trough positions for different substrates

3.6 Deriving the complex refractive index

The measurement setup is as shown in Figure 3.1. The main pulse is mathematically defined as:

$$\tilde{\mathbf{E}}_{\text{main}} = R_{01} \tilde{\mathbf{E}}_{\text{in}} \exp \left(-j\omega \frac{\tilde{n}_s}{c} \frac{2L_s}{\cos \theta_t} \sin \theta_t \sin \theta_i \right), \quad (3.36)$$

and the echo pulse is mathematically defined as:

$$\tilde{\mathbf{E}}_{\text{echo}} = T_{01} T_{10} \tilde{R}_{10} \tilde{\mathbf{E}}_{\text{in}} \exp \left(-j\omega \frac{\tilde{n}_s}{c} \frac{2L_s}{\cos \theta_t} \right). \quad (3.37)$$

Combining equations (3.35), (3.36), and (3.37) yields,

$$\tilde{H} = \frac{T_{01} T_{10}}{R_{01}} \tilde{R}_{10} \exp \left(-j \frac{\omega}{c} \frac{2L_s}{\cos \theta_t} [\tilde{n}_s - \sin \theta_t n_a \sin \theta_i] \right). \quad (3.38)$$

Using the equations (3.3) to (3.6) based on Snell's law, equation (3.38) can be reduced to

$$\tilde{H} = T_{01} T_{10} \frac{R_{10}}{R_{01}} \exp \left(-j \frac{\omega}{c} 2L_s \cos \theta_t [n_s - j\kappa_s] \right). \quad (3.39)$$

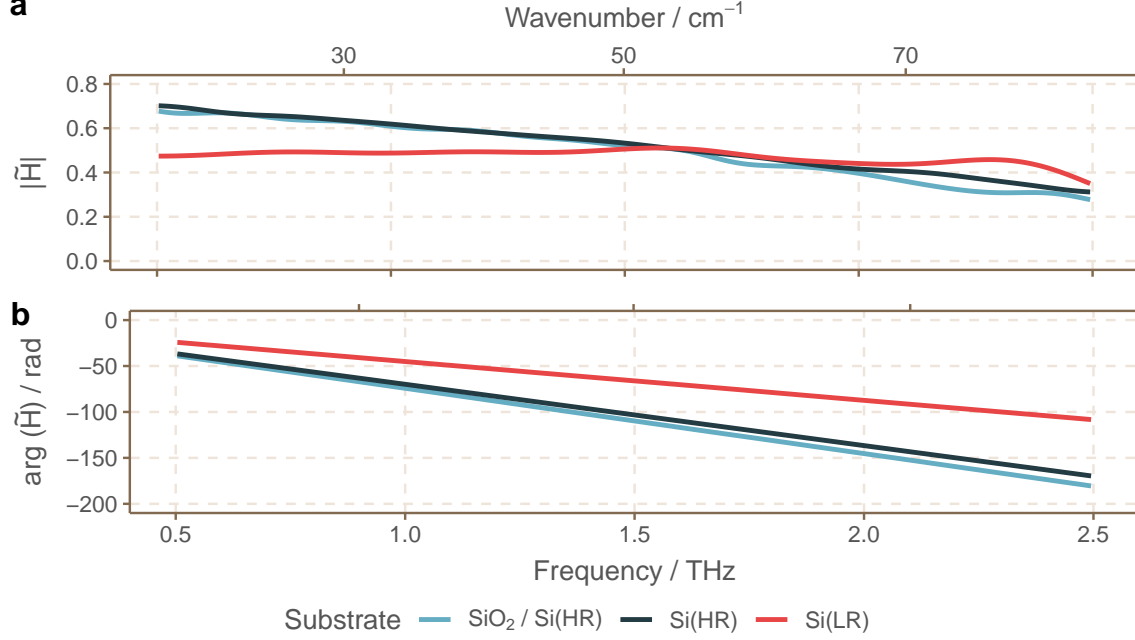


Figure 3.7: Transfer function for different substrates

For *p*-polarized light, based on the general form of Fresnel coefficients given in [52], the transmission coefficients going from air to substrate T_{01} , and substrate to air T_{10} are defined as.

$$T_{01} = \frac{2 \cos \theta_i}{n_s \cos \theta_i + \cos \theta_t}, \quad (3.40)$$

$$T_{10} = \frac{2 n_s \cos \theta_t}{n_s \cos \theta_i + \cos \theta_t}. \quad (3.41)$$

Therefore, the effective transmission coefficient for the substrate can be written as,

$$T_s = T_{01} T_{10} = \frac{4 n_s \cos \theta_i \cos \theta_t}{(n_s \cos \theta_i + \cos \theta_t)^2}. \quad (3.42)$$

Similarly, the Fresnel reflection coefficients are given by,

$$R_{01} = \frac{\cos \theta_t - n_s \cos \theta_i}{\cos \theta_t + n_s \cos \theta_i}, \quad (3.43)$$

$$R_{10} = \frac{n_s \cos \theta_i - \cos \theta_t}{n_s \cos \theta_i + \cos \theta_t}. \quad (3.44)$$

It follows that

$$\frac{R_{01}}{R_{10}} = -1 = \exp(j\pi). \quad (3.45)$$

The transfer function now becomes

$$|\tilde{H}| \exp(-j \arg[\tilde{H}]) = T_s \exp\left(-\frac{\omega}{c} \kappa_s 2L_s \cos \theta_t\right) \exp\left(-j \left[-\pi + \frac{\omega}{c} n_s 2L_s \cos \theta_t\right]\right). \quad (3.46)$$

Equating the argument on both sides of equation (3.46) will yield the substrate refractive index:

$$\arg[\tilde{H}] = -\pi + \frac{\omega}{c} n_s 2L_s \cos \theta_t, \quad (3.47)$$

$$\arg[\tilde{H}] + \pi = \frac{\omega}{c} 2L_s \sqrt{n_s^2 - \sin^2 \theta_i}, \quad (3.48)$$

$$n_s = \sqrt{\left(\frac{c}{2\omega L_s} (\arg[\tilde{H}] + \pi)\right)^2 + \sin^2 \theta_i}. \quad (3.49)$$

The substrate extinction coefficient is determined by equating the magnitudes of equation (3.46).

Therefore,

$$|\tilde{H}| = T_s \exp\left(-\frac{\omega}{c} 2L_s \cos \theta_t \kappa_s\right), \quad (3.50)$$

$$\kappa_s = \frac{-c}{2\omega L_s \cos \theta_t} \left(\ln[|\tilde{H}_{\text{sub}}|] - \ln[T_s] \right). \quad (3.51)$$

The absorption coefficient is related to the extinction coefficient as:

$$\alpha_s = \frac{2\omega}{c} \kappa_s. \quad (3.52)$$

This is plotted in Figure 3.8(a) as α/ω^2 to normalize for the increasing density of states with increasing frequency.

The complex dielectric function, shown in Figure 3.9 is defined as $\tilde{\epsilon}_s = \tilde{n}_s^2$. This expands to:

$$\epsilon_r - j\epsilon_i = n_s^2 + \kappa_s^2 - j2n_s\kappa_s. \quad (3.53)$$

The ratio of the imaginary part of the complex dielectric function to its real part, which is plotted in Figure 3.10, gives an indication of the material property. Typically, if $\frac{\epsilon_l}{\epsilon_r} \ll 1$, then the material is

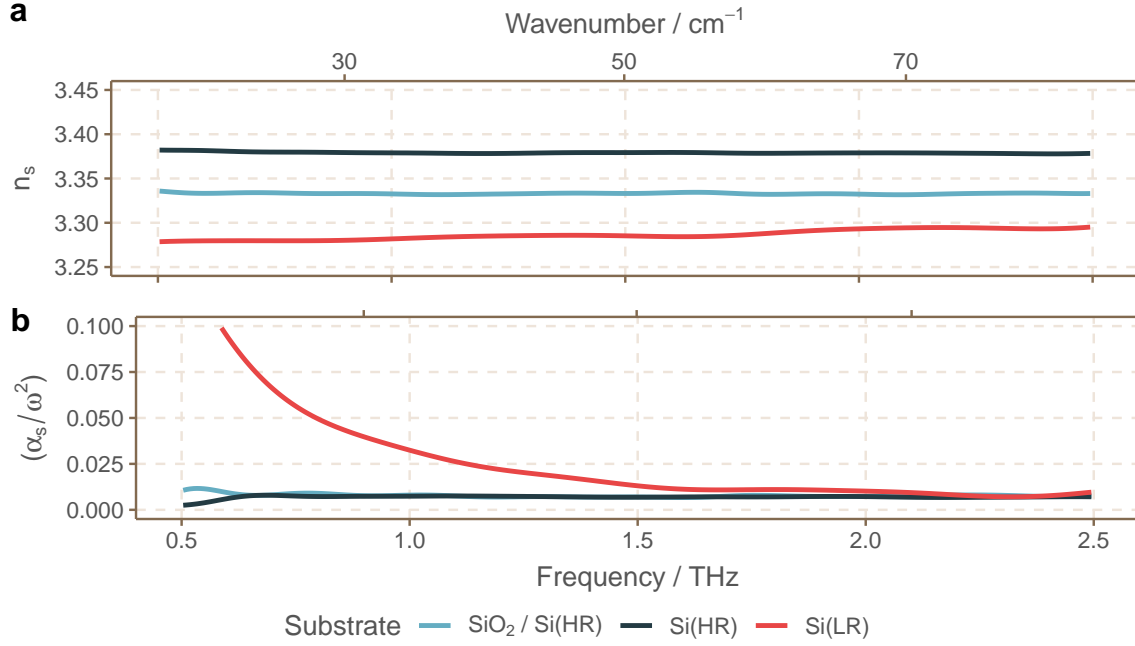


Figure 3.8: Complex refractive index for different substrates

considered to be a low-loss dielectric. Likewise, if $\frac{\epsilon_l}{\epsilon_r} \gg 1$, then the material is said to be a good conductor. For $0.01 \leq \frac{\epsilon_l}{\epsilon_r} \leq 100$, the material is a quasi-conductor. Based on the values seen in Figure 3.10, with the exception of Si(LR), the substrates measured here present as low-loss dielectrics. This is of importance because it implies that an undoped silicon wafer makes for a good substrate for sample characterization because very little of the incident radiation will be lost to it. The moderately doped Si(LR) wafer has a manufacturer specified resistivity of 1 to $10 \Omega \text{ cm}$. The effect of the small amount of charge carriers is apparent in the form of loss, which decays with increasing frequency.

3.7 Conclusion

The directly proportional relationship between resistivity and refractive index signifies a reduction in phase shift between the electric field and the current density induced in the substrate [53]. This correlation between complex refractive index and resistivity is in agreement with earlier findings [53,54], the accuracy with which we can calculate \tilde{n}_{sub} is limited. This is especially true in the case of moderately doped substrates because wafer specifications include a significant uncertainty in thickness (typically $\pm 25 \mu\text{m}$) as well as a broad range of resistivity values. The decreased refractive index of

3.7 Conclusion

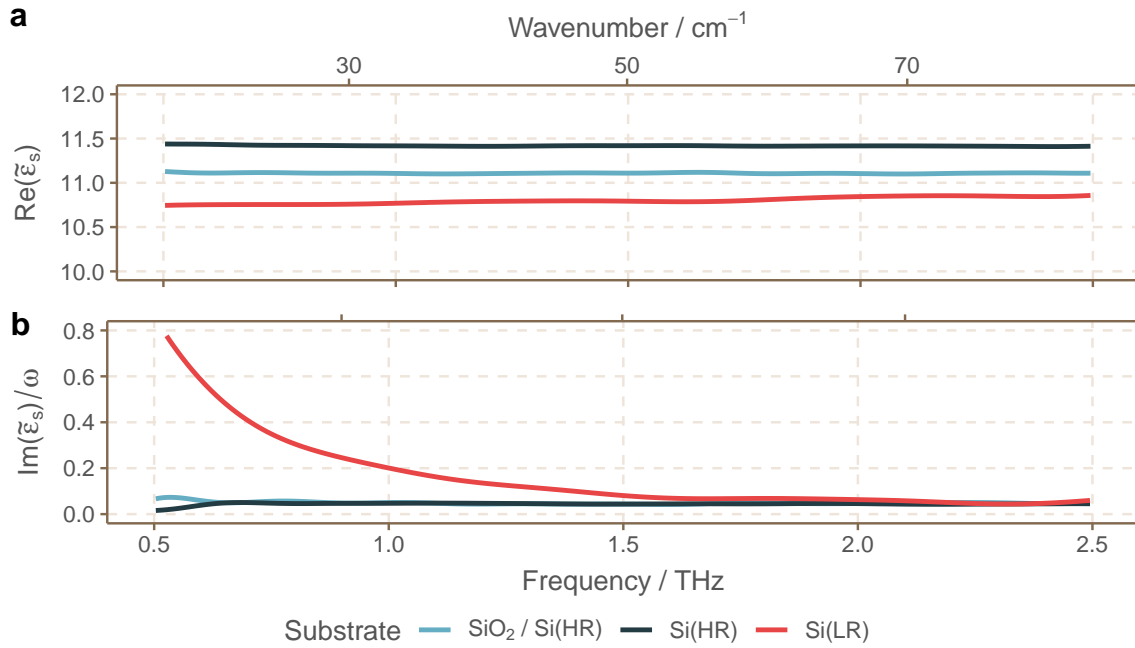


Figure 3.9: Complex dielectric function for different substrates

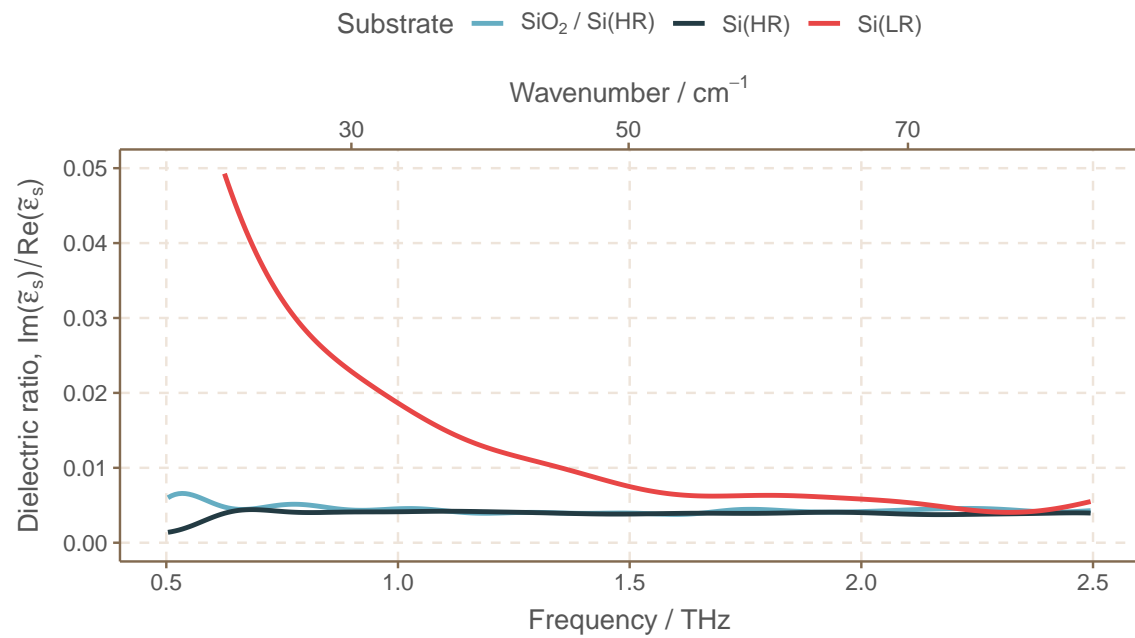


Figure 3.10: Dielectric function ratio for different substrates

3.7 Conclusion

the $\text{SiO}_2/\text{Si(HR)}$ substrate can be attributed to the effective value of the combination of the smaller refractive index of SiO_2 , reported in [55] as about 2, and larger value for Si(HR) . By measuring the thickness using the method reported in Chapter 2, we can accurately and independently determine the refractive index of a substrate, thereby allowing us to account for its related effects in subsequent sample characterization.

CHAPTER 4

Transmission Line Model

Typically in THz-TDS measurements, the material of interest is placed on top of a substrate (or window), whose properties are pre-determined. As described in Chapter 3, the process of sample data extraction involves forming a transfer function with a measurement from a blank substrate, which is used as a reference, and another measurement with the sample placed on the substrate. The transmission or reflection data at the substrate-sample interface is collected. The sample properties are then extracted by using the appropriate Fresnel coefficient equations for the given polarization of the THz beam.

In reflection geometry, the commonly used Fresnel reflection coefficient equations for *p*-polarized light at the interface of medium *a* and medium *b* are:

- 1) For dielectrics [39]:

$$\tilde{R}_{ab} = \frac{\tilde{n}_a \cos \theta_b - \tilde{n}_b \cos \theta_a}{\tilde{n}_a \cos \theta_b + \tilde{n}_b \cos \theta_a}, \quad (4.1)$$

- 2) For thin-film conductors [35]:

$$\tilde{R}_{ab} = \frac{\tilde{n}_a \cos \theta_b - \tilde{n}_b \cos \theta_a - \cos \theta_a \cos \theta_b \tilde{\sigma} Z_0}{\tilde{n}_a \cos \theta_b + \tilde{n}_b \cos \theta_a + \cos \theta_a \cos \theta_b \tilde{\sigma} Z_0}, \quad (4.2)$$

where $\tilde{\sigma}$ is the complex conductivity of the thin-film at the interface between medium *a* and medium *b*.

Extracting material properties through the use of these equations requires one to know beforehand the type of interface being probed, i.e., dielectric–dielectric, metal–dielectric, etc. In the case of

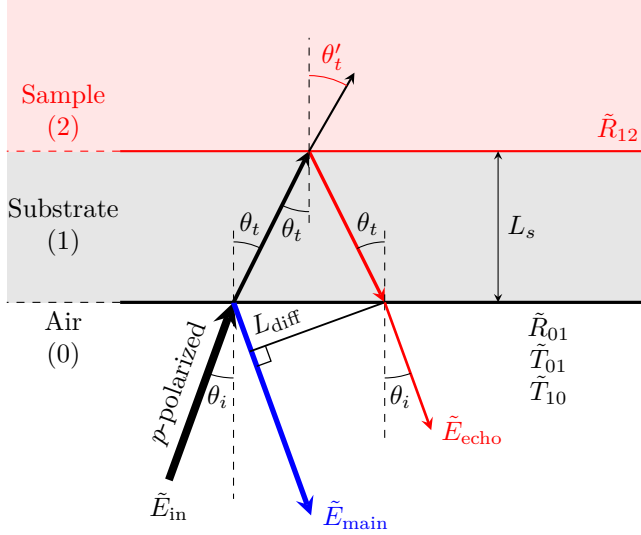


Figure 4.1: Experimental setup for a sample on top of a substrate

an unknown sample, or a known sample of unknown thickness, one cannot know *beforehand* what is happening at the interface. In this chapter, we will apply a transmission line model to describe the propagation of the THz wave as it travels through different media and reflects at the different interfaces. By using this model to extract the complex impedance, we can determine the type of interface and extract material properties of an unknown sample.

4.1 Complex reflection coefficients

To find the sample properties, we place the sample on top of a substrate, which is typically Si(HR) or SiO₂/Si(HR), and illuminate it with THz light as shown in Figure 4.1. The first interface is air–substrate, denoted by subscript 01, and the second interface is the substrate–sample, denoted by subscript 12.

The information about the sample properties is encoded in the reflection obtained from the substrate–sample interface. Since the acquired data is the reflection of the THz beam at each interface, correctly extracting the respective reflection coefficients is paramount.

Since the first interface is the air–substrate interface, the reflection coefficient there is obtained as follows:

$$\tilde{R}_{01} = \frac{\tilde{\mathbf{E}}_{\text{main}}}{\tilde{\mathbf{E}}_{\text{in}}} = \frac{\cos \theta_t - \tilde{n}_s \cos \theta_i}{\cos \theta_t + \tilde{n}_s \cos \theta_i}, \quad (4.3)$$

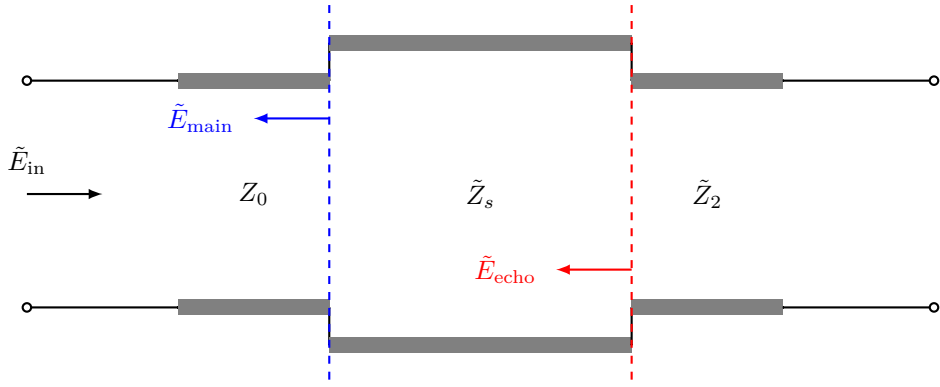


Figure 4.2: Transmission line model with loads representing the interface of each side of the substrate

where \tilde{E}_{in} is the reference THz pulse measured by placing an Al mirror in place of the substrate.

The reflection at the second interface is obtained after part of the incident THz pulse travels through the substrate and back. Therefore, it can be calculated from the transfer function as follows:

$$\tilde{H} = \frac{\tilde{T}_{01}\tilde{T}_{10}}{\tilde{R}_{01}} \tilde{R}_{12} \exp\left(-j\frac{\omega}{c}2\tilde{n}_s L_s \cos \theta_t\right), \quad (4.4)$$

$$\tilde{R}_{12} = \tilde{H} \frac{\tilde{R}_{01}}{\tilde{T}_s} \exp\left(j\frac{\omega}{c}2\tilde{n}_s L_s \cos \theta_t\right), \quad (4.5)$$

where \tilde{R}_{01} is obtained from equation (4.3), and $\tilde{T}_s = \tilde{T}_{01}\tilde{T}_{10}$.

4.2 Transmission line equivalent

Figure 4.1 can be visualized as the transmission line shown in Figure 4.2. Doing so allows us to calculate the complex impedance of the material on each side of the interface using the equations [56]:

$$\tilde{\Gamma}_{01} = \frac{\tilde{Z}_s - Z_0}{\tilde{Z}_s + Z_0}, \quad (4.6)$$

$$\tilde{\Gamma}_{12} = \frac{\tilde{Z}_2 - \tilde{Z}_s}{\tilde{Z}_2 + \tilde{Z}_s}. \quad (4.7)$$

4.3 Extracting material properties for bulk samples

For the general case of an electromagnetic wave traveling from bulk medium a to bulk medium b , the transmission line and Fresnel reflection coefficients can be equated as follows:

$$\tilde{\Gamma}_{ab} = \tilde{R}_{ab}, \quad (4.8)$$

$$\frac{\tilde{Z}_b - \tilde{Z}_a}{\tilde{Z}_b + \tilde{Z}_a} = \frac{\tilde{n}_a \cos \theta_b - \tilde{n}_b \cos \theta_a}{\tilde{n}_a \cos \theta_b + \tilde{n}_b \cos \theta_a}, \quad (4.9)$$

$$\frac{\tilde{Z}_b/\tilde{Z}_a - 1}{\tilde{Z}_b/\tilde{Z}_a + 1} = \frac{\tilde{n}_a \cos \theta_b}{\tilde{n}_b \cos \theta_a} - 1. \quad (4.10)$$

This implies,

$$\frac{\tilde{Z}_b}{\tilde{Z}_a} = \frac{\tilde{n}_a}{\cos \theta_a} \frac{\cos \theta_b}{\tilde{n}_b}. \quad (4.11)$$

If medium b is the material of interest, then let

$$\tilde{Z}_N = \frac{\tilde{Z}_b}{\tilde{Z}_a} \frac{\cos \theta_a}{\tilde{n}_a} = \frac{\cos \theta_b}{\tilde{n}_b}. \quad (4.12)$$

According to Snell's law at the two interfaces,

$$n_{\text{air}} \sin \theta_i = \tilde{n}_a \sin \theta_a = \tilde{n}_b \sin \theta_b, \quad (4.13)$$

$$\frac{\sin^2 \theta_i}{\tilde{n}_a^2} = \sin^2 \theta_a = (1 - \cos^2 \theta_a), \quad (4.14)$$

$$\frac{\sin^2 \theta_i}{\tilde{n}_b^2} = \sin^2 \theta_b = (1 - \cos^2 \theta_b). \quad (4.15)$$

Therefore,

$$\cos^2 \theta_a = \frac{\tilde{n}_a^2 - \sin^2 \theta_i}{\tilde{n}_a^2}, \quad (4.16)$$

$$\cos^2 \theta_b = \frac{\tilde{n}_b^2 - \sin^2 \theta_i}{\tilde{n}_b^2}. \quad (4.17)$$

Squaring equation (4.12) and substituting the above equation for $\cos^2 \theta_a$ yields

$$\tilde{Z}_N^2 = \frac{\tilde{n}_b^2 - \sin^2 \theta_i}{\tilde{n}_b^4}. \quad (4.18)$$

Since $\tilde{\epsilon} = \tilde{n}^2$,

$$Z_N^2 \tilde{\epsilon}_b^2 - \tilde{\epsilon}_b + \sin^2 \theta_i = 0. \quad (4.19)$$

The positive root of this quadratic equation is

$$\tilde{\epsilon} = \frac{1 + \sqrt{1 - 4\tilde{Z}_N^2 \sin^2 \theta_i}}{2}, \quad (4.20)$$

which we can use to extract the complex refractive index as $\tilde{n} = \sqrt{\tilde{\epsilon}}$.

4.3.1 Perfect dielectric

In the case of an interface with a perfect dielectric, such as air, on both sides of the substrate, \tilde{Z}_1 and \tilde{Z}_2 in equations (4.6) and (4.7) will be replaced by the free-space impedance $Z_0 = \sqrt{\frac{\mu_0}{\epsilon_0}} \approx 377 \Omega$. At the air–substrate interface,

$$\tilde{\Gamma}_{01} = \frac{\tilde{Z}_s - Z_0}{\tilde{Z}_s + Z_0}, \quad (4.21)$$

$$\tilde{Z}_s = \frac{1 + \tilde{\Gamma}_{01}}{1 - \tilde{\Gamma}_{01}} Z_0. \quad (4.22)$$

Similarly, at the substrate–air interface,

$$\tilde{\Gamma}_{10} = \frac{Z_0 - \tilde{Z}_s}{Z_0 + \tilde{Z}_s}, \quad (4.23)$$

$$Z_0 = \frac{1 + \tilde{\Gamma}_{10}}{1 - \tilde{\Gamma}_{10}} \tilde{Z}_s. \quad (4.24)$$

Equation (4.11) takes the following form for the THz wave going from air to substrate at the first interface:

$$\frac{\tilde{Z}_s}{Z_0} = \frac{1}{\cos \theta_i} \frac{\cos \theta_t}{\tilde{n}_s}. \quad (4.25)$$

Solving equations (4.12) to (4.20) yields the complex dielectric function and complex refractive index

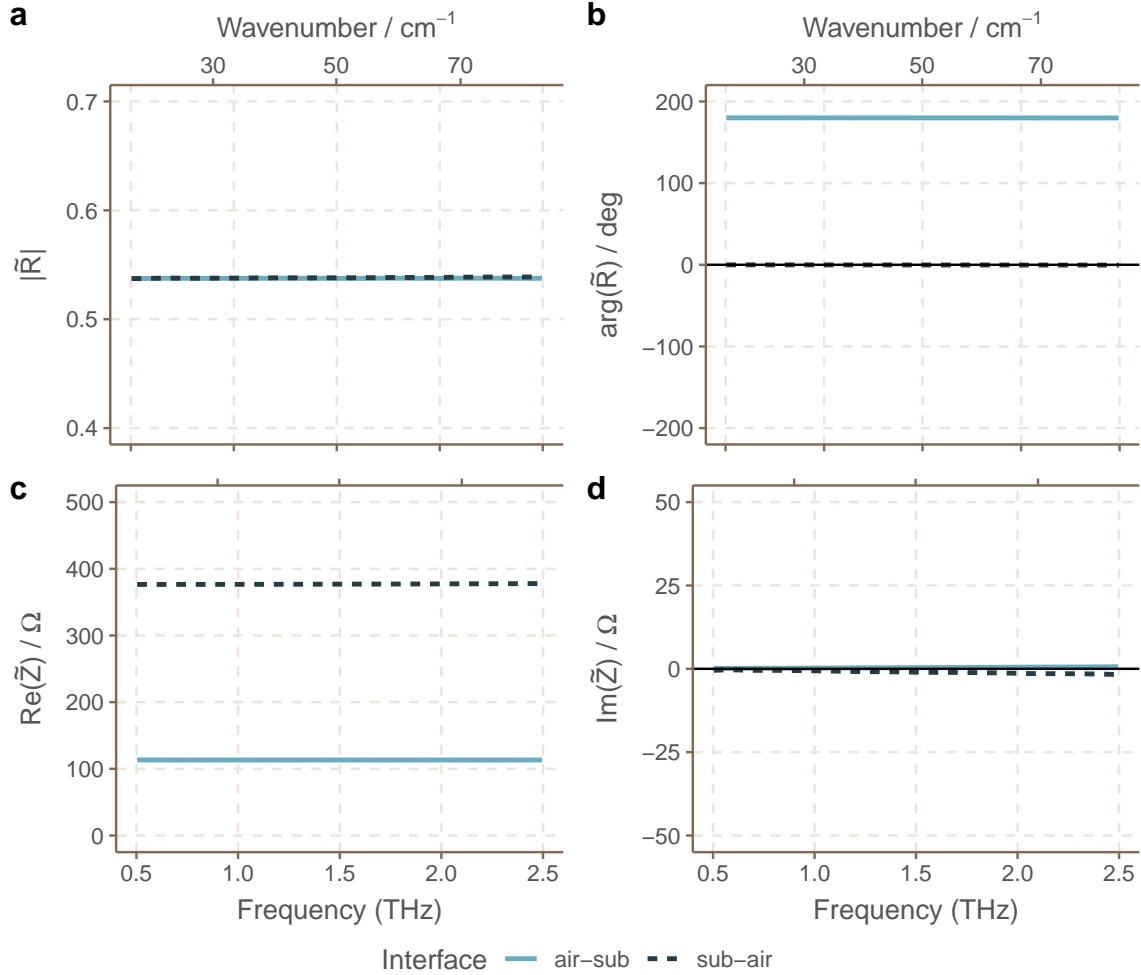


Figure 4.3: Complex reflection coefficients and complex impedance values for the air–substrate–air interfaces.

of the substrate, which is Si(HR) in this case. Figures 4.4 and 4.5 show the extracted values. There is found to be a close match to the values calculated using the equations described in the previous chapter.

While going from substrate to air at the second interface, equation (4.11) will take the form,

$$\frac{\tilde{Z}_0}{Z_s} = \frac{\tilde{n}_s}{\cos \theta_t} \frac{\cos \theta_i}{\tilde{n}_a}. \quad (4.26)$$

Now, solving equations (4.12) to (4.20) will yield the complex dielectric function and complex refractive index of air, which are plotted in Figures 4.4 and 4.5, respectively.

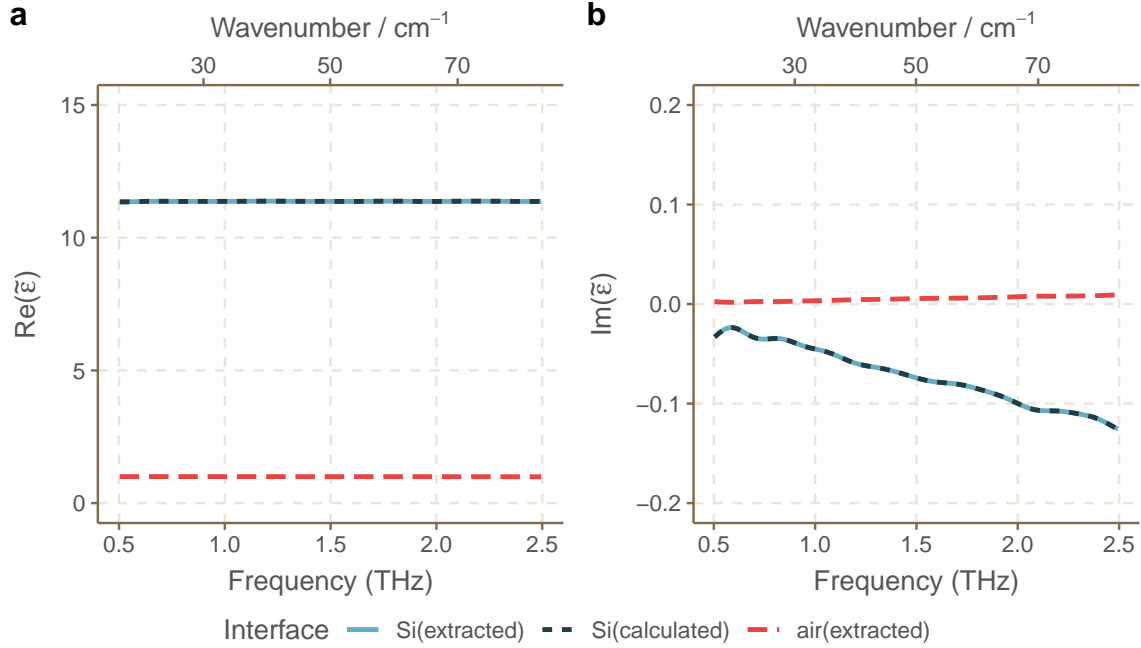


Figure 4.4: Complex dielectric function for substrate and air

4.3.2 Lossy dielectric

In case of a lossy dielectric, such as water, placed on top of a Si(HR) substrate, equations (4.6) and (4.7) change as follows: At the air–substrate interface, equation (4.21) applies, and at the substrate–water interface we have:

$$\tilde{\Gamma}_{12} = \frac{\tilde{Z}_2 - \tilde{Z}_s}{\tilde{Z}_2 + \tilde{Z}_s}, \quad (4.27)$$

$$\tilde{Z}_2 = \frac{1 + \tilde{\Gamma}_{12}}{1 - \tilde{\Gamma}_{12}} \tilde{Z}_s. \quad (4.28)$$

At the substrate–water interface, equation (4.11) will take the form,

$$\frac{\tilde{Z}_2}{Z_s} = \frac{\tilde{n}_s}{\cos \theta_t} \frac{\cos \theta_w}{\tilde{n}_w}, \quad (4.29)$$

where $\cos \theta_w$ is the refraction angle inside water. Solving equations (4.12) to (4.20) will yield the complex dielectric function and complex refractive index of water, which are plotted in Figures 4.4 and 4.5. These results are compared against the values obtained when they are calculated from the

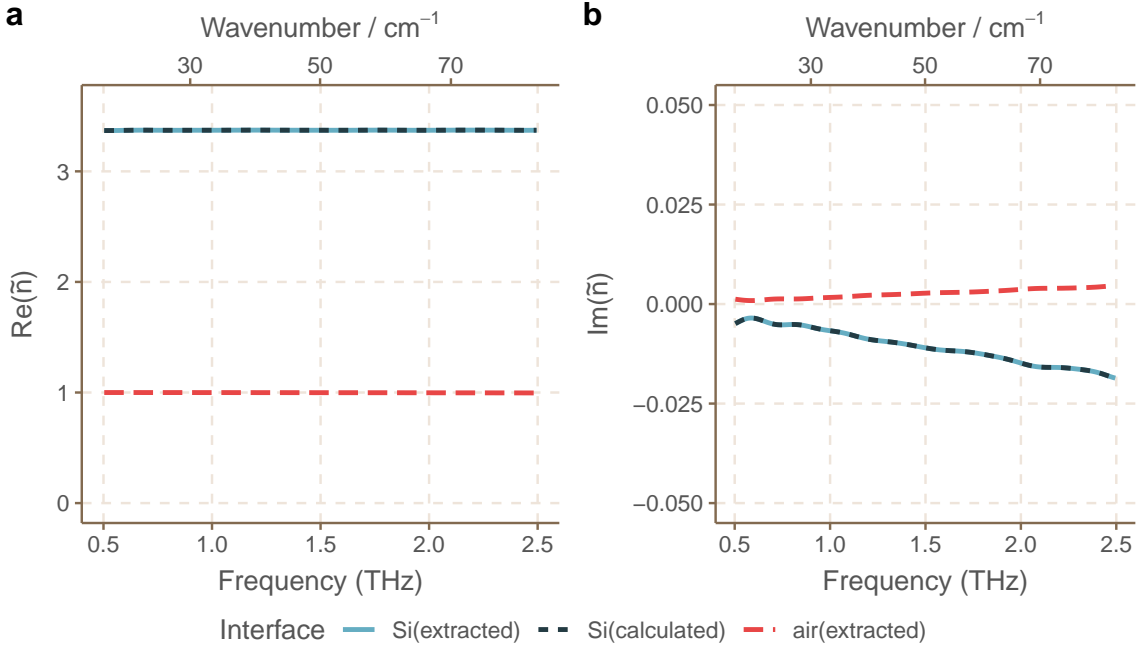


Figure 4.5: Complex refractive index for substrate and air

Fresnel reflection coefficient given below as described in [39]:

$$\tilde{R}_{12} = \frac{\tilde{n}_s^2 \sqrt{\tilde{n}_w^2 - \sin^2 \theta_i} - \tilde{n}_w^2 \sqrt{\tilde{n}_s^2 - \sin^2 \theta_i}}{\tilde{n}_s^2 \sqrt{\tilde{n}_w^2 - \sin^2 \theta_i} + \tilde{n}_w^2 \sqrt{\tilde{n}_s^2 - \sin^2 \theta_i}}. \quad (4.30)$$

Since the values obtained are identical, it confirms that, as expected, the transmission line approach is completely analogous to using Fresnel coefficients and the propagating electromagnetic wave approach.

From the above cases, it is observed that the complex impedance for bulk dielectrics takes the form $\tilde{Z}_2 = R_2 + jX_2$. The positive imaginary part signifies an inductive reactance, which translates into the complex dielectric function having the form $\tilde{\epsilon} = \epsilon_r - j\epsilon_i$. This is in line with our phasor notation for the electric field.

4.3.3 Bulk conductors

When a bulk metal is placed on top of the substrate, it is equivalent to the case of a transmission line terminated by a short-circuit, as shown in Figure 4.9. In this case, the input impedance of the

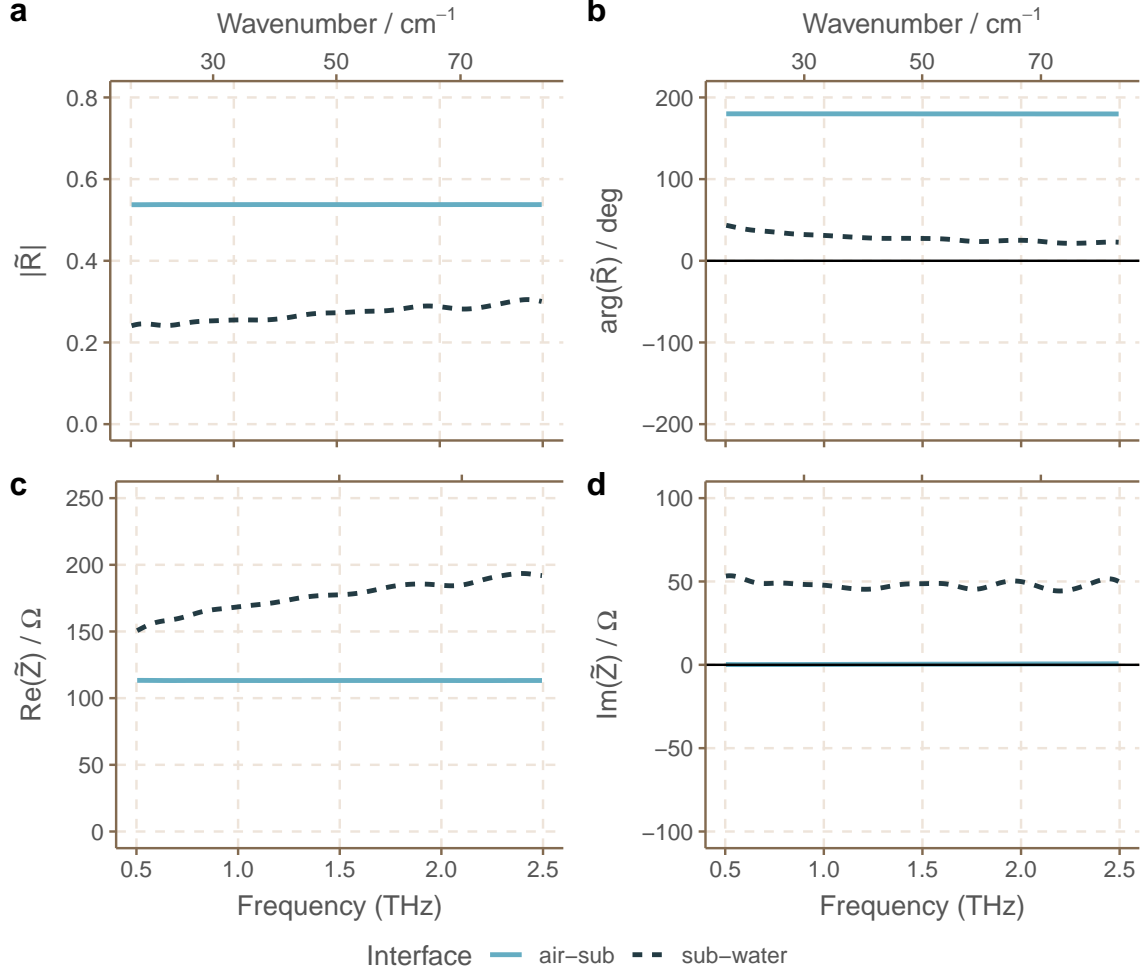


Figure 4.6: Complex reflection coefficients and complex impedance for the substrate–water interface.

line is defined as [56]:

$$\tilde{Z}_{\text{in}} = jZ_s \tan(\beta L_{\text{eff}}), \quad (4.31)$$

where,

$$\beta L_{\text{eff}} = \frac{2\pi f}{c} n_s L_s \cos \theta_t = \frac{2\pi}{\lambda} n_s L_s \cos \theta_t. \quad (4.32)$$

Since the input impedance is purely imaginary, it is called the input reactance. If $L_{\text{eff}} = L_s \cos \theta_t$ is the effective thickness of the substrate, i.e. the length of the transmission line, and $v_p = c/n_s$ is the phase velocity of electromagnetic wave inside the transmission line, then the input reactance

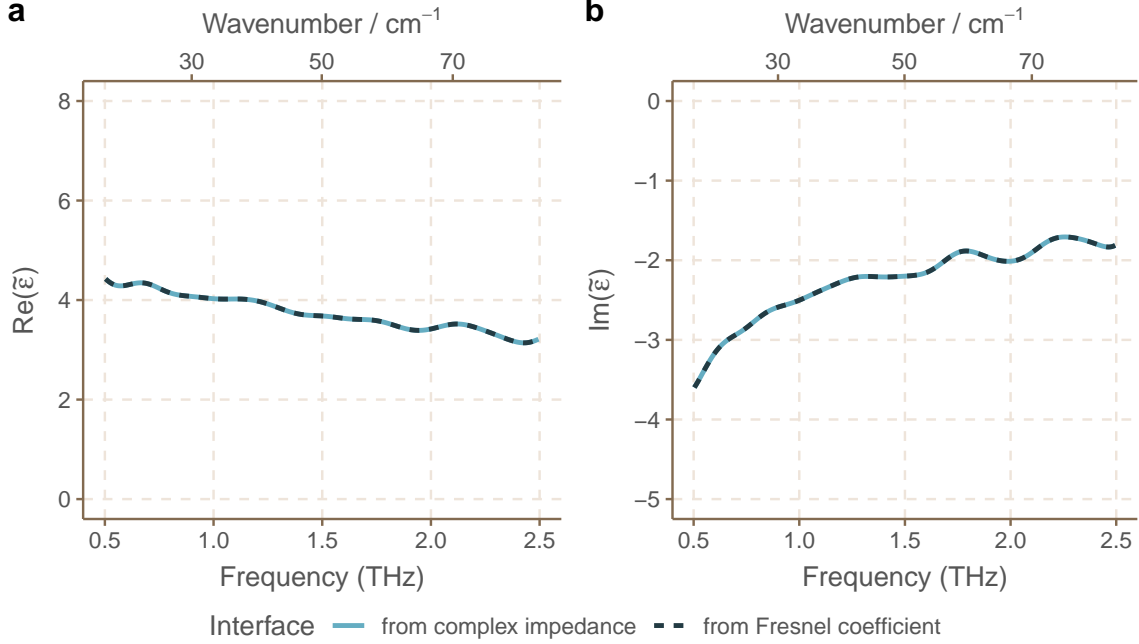


Figure 4.7: Complex dielectric function for water

varies with frequency, as shown in Figure 4.10. The phase velocity in a non-magnetic material can also be expressed as

$$v_p = \frac{\omega}{\beta} = \frac{1}{\sqrt{\epsilon}} = \frac{1}{\sqrt{L_{\text{eq}} C_{\text{eq}}}}. \quad (4.33)$$

The characteristic impedance of the transmission line can be expressed as

$$Z_s = \sqrt{\frac{L_{\text{eq}}}{C_{\text{eq}}}}, \quad (4.34)$$

where L_{eq} and C_{eq} are the equivalent inductance and capacitance of the transmission line seen by the input.

To understand the behavior of the transmission line at different frequencies, we consider the equations below [57]. For any arbitrary value of βL_{eff} ,

$$\tan(\beta L_{\text{eff}}) = \beta L_{\text{eff}} + \frac{1}{3}(\beta L_{\text{eff}})^3 + \frac{2}{15}(\beta L_{\text{eff}})^5 + \dots \quad (4.35)$$

At low frequencies, $\beta L_{\text{eff}} \ll 1$ or $L_{\text{eff}} \ll \frac{\lambda}{2\pi}$, i.e., for wavelengths much longer than the effective

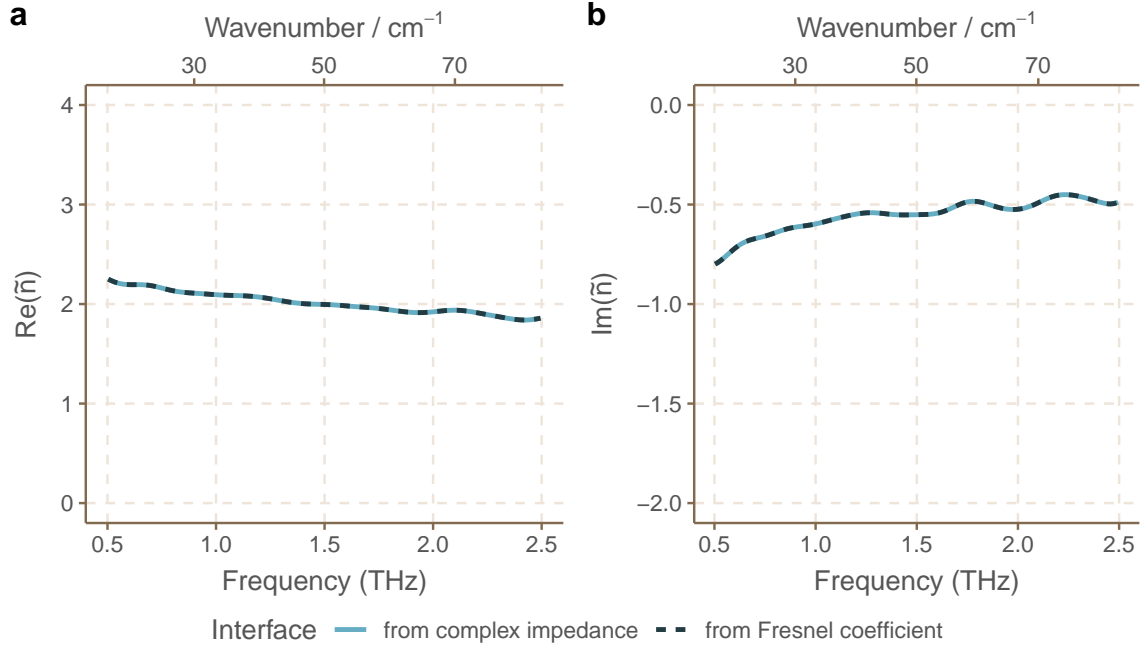


Figure 4.8: Complex refractive index for water

substrate thickness,

$$\tan \beta L_{\text{eff}} \approx \beta L_{\text{eff}}. \quad (4.36)$$

Therefore,

$$\tilde{Z}_{\text{in}} \approx j Z_s \beta L_{\text{eff}} = j \sqrt{\frac{L_{\text{eq}}}{C_{\text{eq}}}} \omega \sqrt{L_{\text{eq}} C_{\text{eq}}} L_{\text{eff}}, \quad (4.37)$$

$$\tilde{Z}_{\text{in}} = j \omega L_{\text{eq}} L_{\text{eff}}. \quad (4.38)$$

Thus, for wavelengths much longer than the effective substrate thickness, the transmission line behaves like an equivalent inductance to the incident THz electric field.

For frequencies slightly higher than the above case, or for wavelengths on the order of the effective

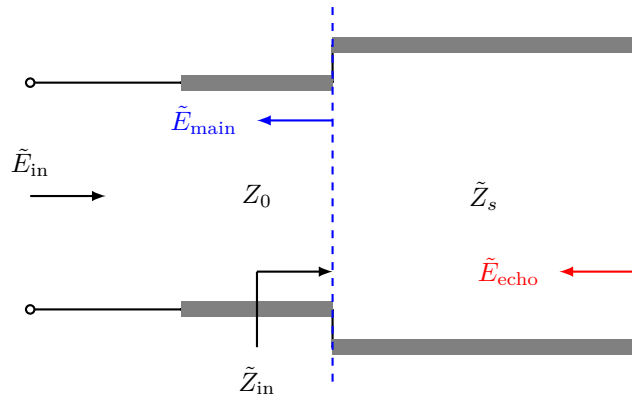


Figure 4.9: Transmission line model for bulk metal on top of the substrate.

substrate thickness,

$$\tan(\beta L_{\text{eff}}) \approx \beta L_{\text{eff}} + \frac{1}{3}(\beta L_{\text{eff}})^3, \quad (4.39)$$

$$= jZ_s \left(\beta L_{\text{eff}} + \frac{1}{3}\beta^3 L_{\text{eff}}^3 \right), \quad (4.40)$$

$$= j\sqrt{\frac{L_{\text{eq}}}{C_{\text{eq}}}} \left(\omega \sqrt{L_{\text{eq}} C_{\text{eq}}} L_{\text{eff}} + \frac{1}{3}\omega^3 L_{\text{eq}}^{2/3} C_{\text{eq}}^{2/3} L_{\text{eff}}^3 \right), \quad (4.41)$$

$$= j\omega L_{\text{eq}} L_{\text{eff}} \left(1 + \frac{1}{3}\omega^2 L_{\text{eq}} C_{\text{eq}} L_{\text{eff}}^2 \right). \quad (4.42)$$

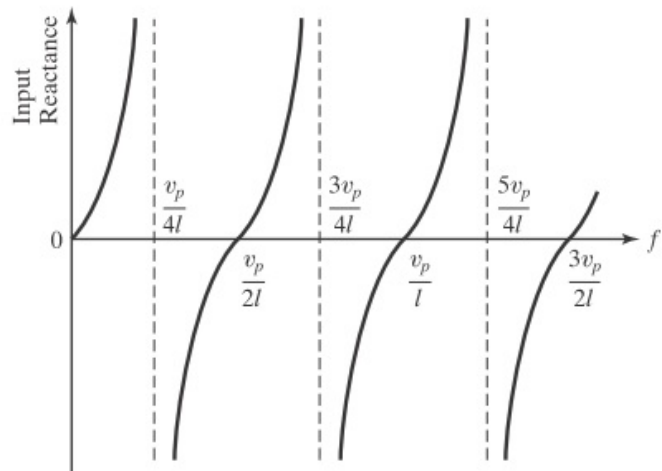


Figure 4.10: Input reactance variation with frequency [57]

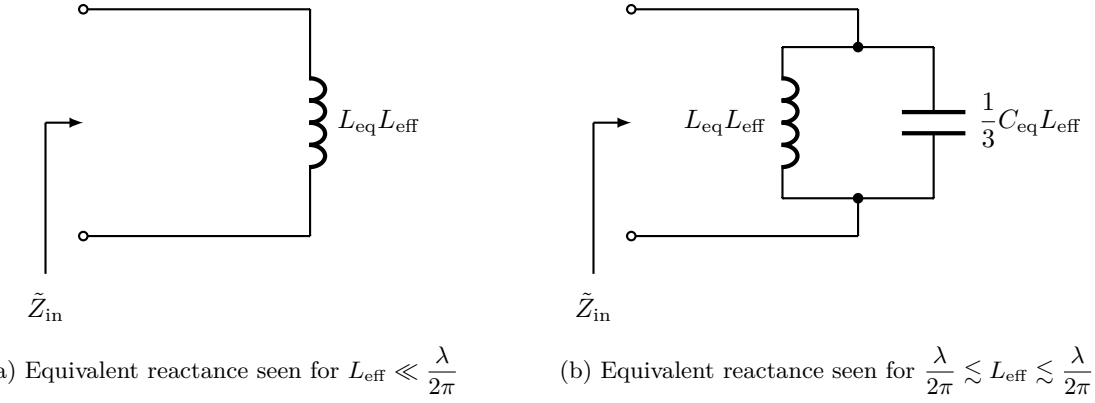


Figure 4.11: Equivalent reactance seen by the incident THz wave depending on its wavelength

In terms of input admittance,

$$\frac{1}{\tilde{Z}_s} = \tilde{Y}_s = \frac{1}{j\omega L_{\text{eq}} L_{\text{eff}}} \left(1 + \frac{1}{3} \omega^2 L_{\text{eq}} C_{\text{eq}} L_{\text{eff}}^2 \right)^{-1}, \quad (4.43)$$

$$\approx \frac{1}{j\omega L_{\text{eq}} L_{\text{eff}}} \left(1 - \frac{1}{3} \omega^2 L_{\text{eq}} C_{\text{eq}} L_{\text{eff}}^2 \right), \quad (4.44)$$

$$= \frac{1}{j\omega L_{\text{eq}} L_{\text{eff}}} + j \frac{1}{3} \omega C_{\text{eq}} L_{\text{eff}}. \quad (4.45)$$

Thus, in the frequency range where the wavelength is comparable to the effective substrate thickness, the transmission line terminated in a short-circuit appears as an equivalent inductance connected in parallel to an equivalent capacitance. In other words, Figure 4.9 gets reduced to the two cases depicted in Figure 4.11 depending on the wavelength relative to the effective substrate thickness.

If we extract the refractive index of the substrate by substituting the 180° phase shift with 0° phase shift, using equation (3.49) from Chapter 3, we get the result shown in Figure 4.12. The consequence of this result is that the substrate refractive index *no longer appears constant* across the frequency range, contrary to the case of having air at the second interface. Instead, it shows a variation because the incoming electric field sees a different reactance depending on its wavelength. Therefore, having a short-circuit termination introduces a pseudo-dispersion effect inside a low-loss dielectric material, even if the material itself is non-dispersive.

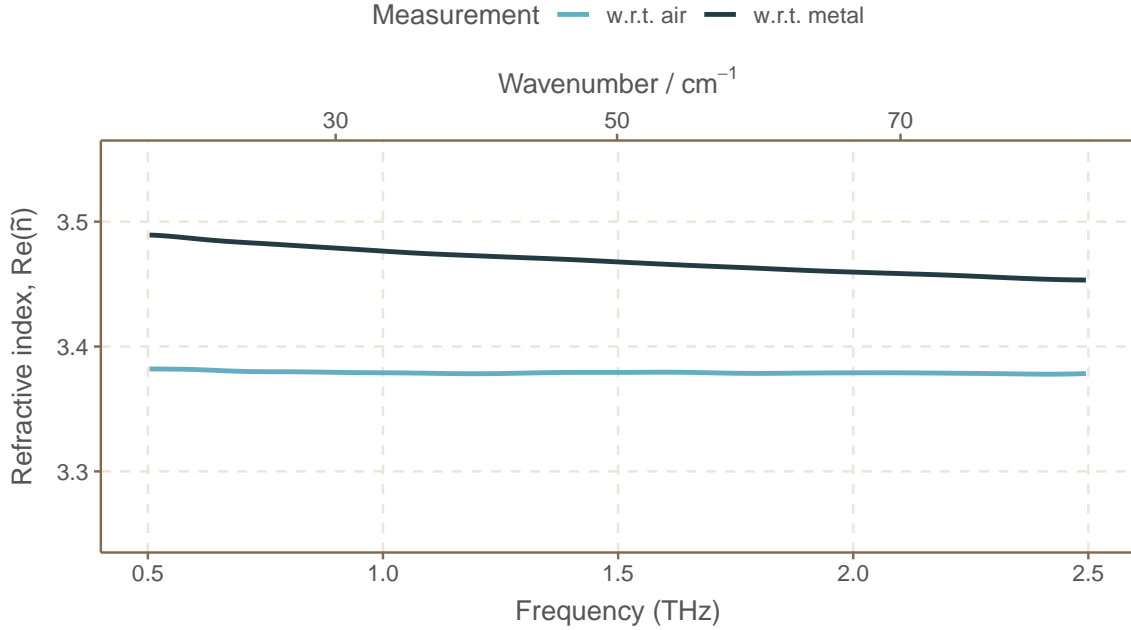


Figure 4.12: Comparison of refractive index of Si(HR) when extracted with respect to air at the back and with respect to Al mirror.

4.3.4 Thin metal films

For a thin metal film deposited on top of a substrate, the experimental set up is shown in Figure 4.13, and its transmission line equivalent model is shown in Figure 5.4. Thin metal films have been shown to exhibit dielectric-like properties [58]. To study this case, a 5 nm nickel film was deposited on the Si(HR) substrate through electron beam (e-beam) evaporation. At the air–substrate interface, equation (4.21) applies, and at the substrate–nickel interface we have:

$$\tilde{\Gamma}_{12} = \frac{\tilde{Z}_2 - \tilde{Z}_s}{\tilde{Z}_s + \tilde{Z}_2}, \quad (4.46)$$

$$\tilde{Z}_2 = \frac{1 + \tilde{\Gamma}_{12}}{1 - \tilde{\Gamma}_{12}} \tilde{Z}_s. \quad (4.47)$$

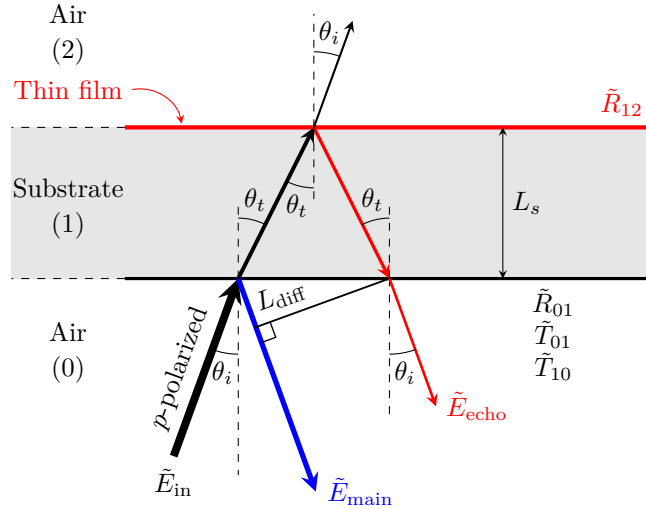


Figure 4.13: Experimental setup for a thin film on the substrate

\tilde{Z}_2 is the effective impedance of the parallel combination of the thin-film and air impedance. The thin-film impedance can be extracted as follows:

$$\tilde{Z}_2 = \tilde{Z}_{\text{Ni}} \parallel Z_0 = \frac{\tilde{Z}_{\text{Ni}} Z_0}{\tilde{Z}_{\text{Ni}} + Z_0}, \quad (4.48)$$

$$\tilde{Z}_2 \tilde{Z}_{\text{Ni}} + \tilde{Z}_2 Z_0 = \tilde{Z}_{\text{Ni}} Z_0, \quad (4.49)$$

$$\tilde{Z}_{\text{Ni}} (Z_0 - \tilde{Z}_2) = \tilde{Z}_2 Z_0. \quad (4.50)$$

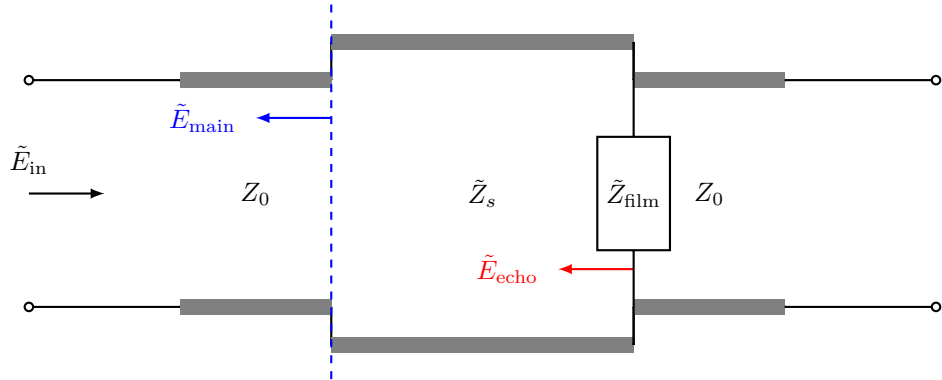


Figure 4.14: Transmission line model for a thin-film at the substrate-air interface.

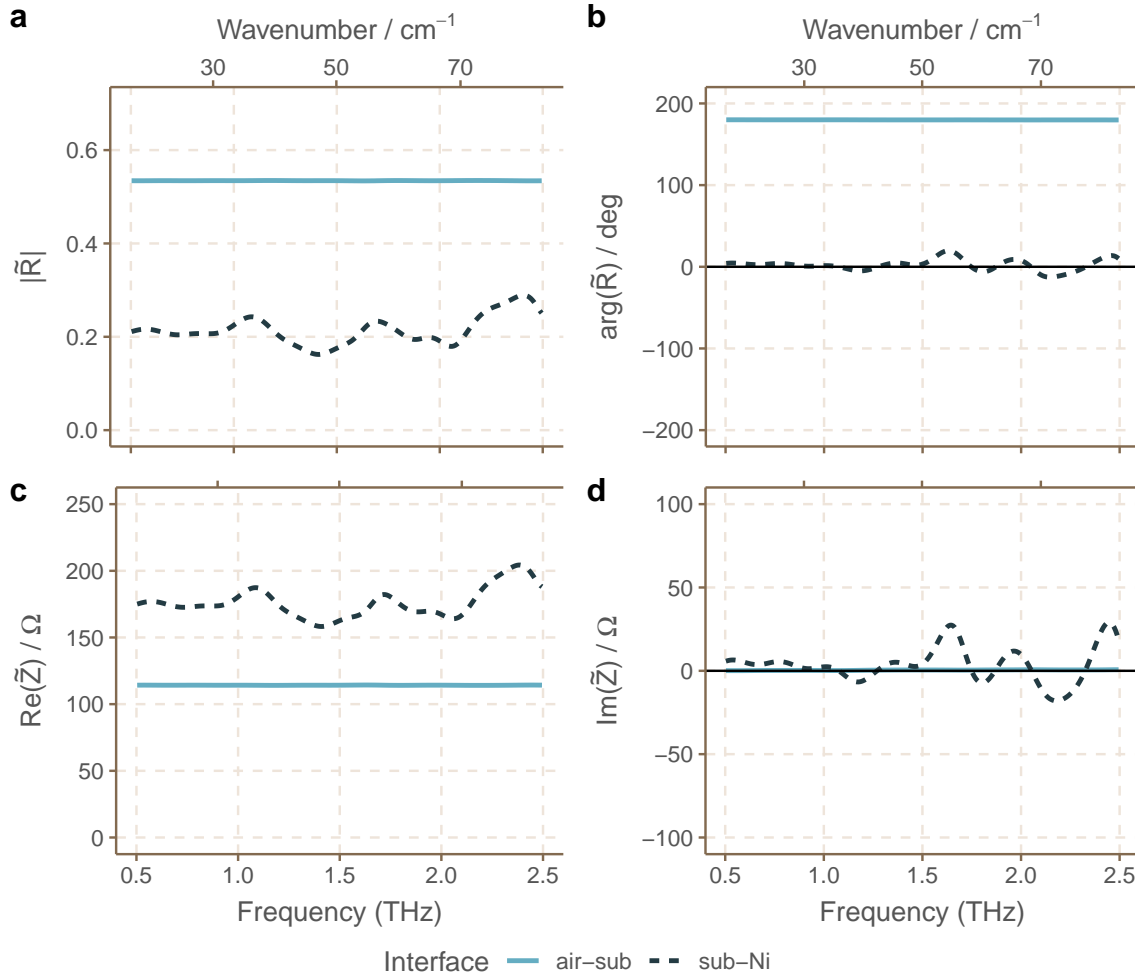


Figure 4.15: Complex reflection coefficients, and complex impedance for the substrate–nickel interface.

Therefore,

$$\tilde{Z}_{\text{Ni}} = \frac{Z_0 - \tilde{Z}_2}{\tilde{Z}_2 Z_0}. \quad (4.51)$$

From the complex impedance, the complex surface conductivity is easily obtained using:

$$\tilde{\sigma} = \frac{1}{\tilde{Z}_{\text{Ni}}} = \frac{Z_0 - \tilde{Z}_2}{Z_0 \tilde{Z}_2}. \quad (4.52)$$

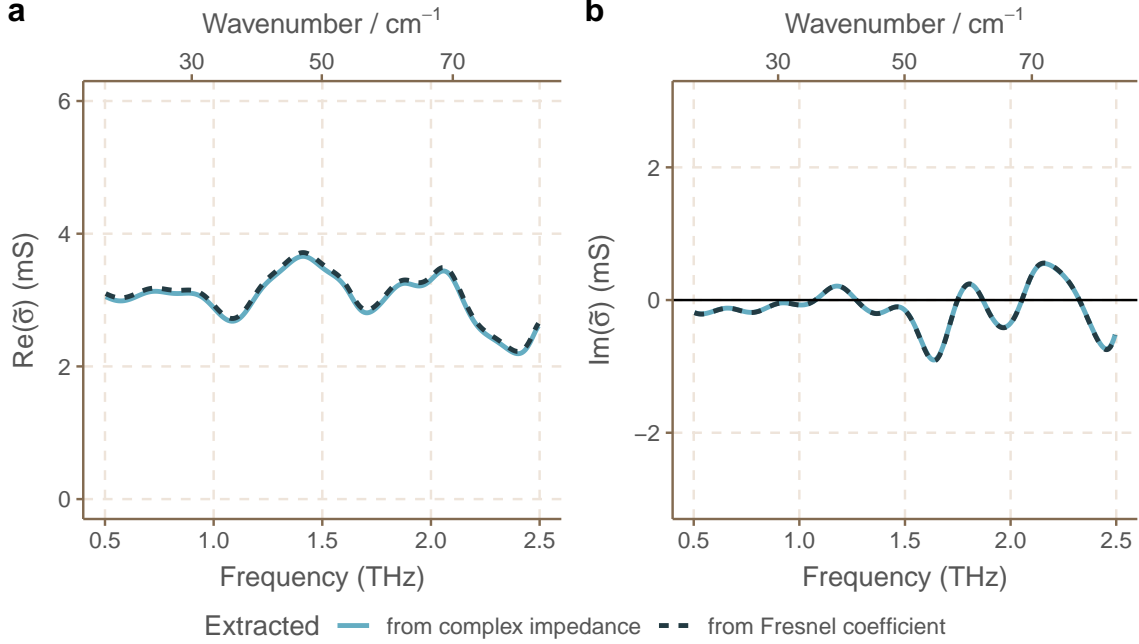


Figure 4.16: Complex conductivity of Ni.

If the complex conductivity is to be extracted from the Fresnel reflection coefficient, then it would take this form [59]:

$$\tilde{\sigma} = \frac{1}{Z_0} \left[\left(\frac{1 - \tilde{R}_{12}}{1 + \tilde{R}_{12}} \right) \frac{\tilde{n}_s}{\cos \theta_t} - \frac{1}{\cos \theta_i} \right]. \quad (4.53)$$

Complex conductivity values obtained through both methods are plotted in Figure 4.16 to show that they agree.

Based on Maxwell's equations, the complex dielectric function is related to the complex conductivity of a material as follows:

$$\tilde{\epsilon} = 1 - j \frac{\tilde{\sigma}}{\epsilon_0 \omega t_f}, \quad (4.54)$$

$$\epsilon_r + j \epsilon_l = 1 - \frac{\text{Im}[\tilde{\sigma}]}{\epsilon_0 \omega t_f} + j \frac{\text{Re}[\epsilon_0 \tilde{\sigma}]}{\omega t_f}, \quad (4.55)$$

where $t_f = 5 \text{ nm}$ is the film thickness. From the very large imaginary part and the negligible real part of the complex dielectric function, as seen in Figure 4.17, we can deduce that a 5 nm Ni film acts more like a lossy dielectric than a conductor. Since these results match a similar behavior reported for other thin metal films in [58], we believe we can extend our method to characterize two-dimensional materials, such as graphene.

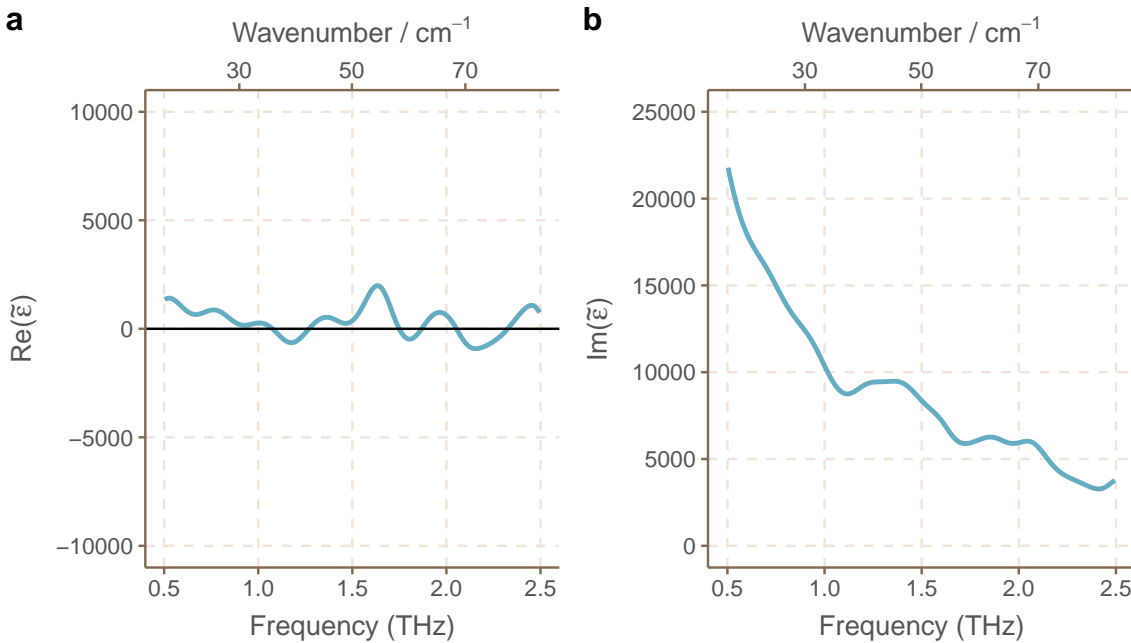


Figure 4.17: Complex dielectric function of Ni.

4.4 Conclusion

Using the transmission line model for a number of materials with very diverse properties, we can identify dielectric behaviour by simply extracting their complex impedances, $\tilde{Z} = R \pm jX$, and noting that the imaginary part is positive. We demonstrate this for the case of water and a 5 nm Ni film. The sample properties, such as the complex dielectric function, are much easier to calculate using the complex impedance instead of the Fresnel reflection coefficient. Moreover, this method requires no prior knowledge of the material properties, making this approach both faster and more broadly applicable.

We also present the special case of a substrate that is terminated by a bulk conductor, where a pseudo-dispersion effect is observed due to the substrate appearing as having a different reactance to the different wavelengths. Therefore, one must exercise caution when characterizing a sample separated by a dielectric over a bulk conductor.

CHAPTER 5

Graphene Characterization

5.1 Motivation

A key reason to use THz spectroscopy for material characterization is to be able to obtain the properties of hard-to-characterize materials, such as extremely thin materials that can have properties quite unlike—and often far superior to—their bulk counterparts. For this reason, increased attention is being paid to two-dimensional materials in the search for novel devices, including those that are functional at THz frequencies. Graphene is currently the most actively studied of these materials, as it shows potential for plasmonic, optoelectronic, and metamaterials applications in the THz frequency range [60]. The complete optical properties of graphene in this spectral range must be well understood to realize many of these applications.

Of its long list of impressive physical properties [61], graphene has the ability to support collective charge oscillations, known as *surface plasmons*, at a graphene–dielectric interface [62]. These surface plasmons can couple to THz-frequency electromagnetic (EM) waves, forming *surface plasmon polaritons*, or SPPs. The much smaller SPP wavelength strongly confines the free-space EM wave at the interface. Appropriate graphene dimensions would then define a resonant cavity that should act as an antenna in the THz range [63].

5.2 Graphene sample preparation: An overview

Graphene is often grown on a copper foil through chemical vapor deposition (CVD), and is then transferred onto a Si wafer having a 300 nm SiO₂ layer. Since a dielectric-conductor interface is necessary to excite and sustain surface plasmons, a negative dielectric function therefore becomes the defining property for a given graphene sample to be suitable for plasmonic applications. Optical characterization methods, such as microscopy and Raman spectroscopy, provide information about the morphology and doping level, but cannot provide a thorough picture of graphene's electrical properties.

We grow graphene from methane using low-pressure chemical vapor deposition on a 25 μm thick commercially available copper foil. The copper foil is first oxidized to suppress graphene nucleation, and then annealed at 1000 °C in the presence of a gas mixture consisting of 5% hydrogen, and 95% nitrogen. Graphene is then synthesized from methane gas having 99.97% purity. To prepare for transfer, the as-grown graphene on copper foil is spin-coated with a layer of poly(methylmethacrylate) (PMMA), and is soft-baked. It is then spin-coated with a second copolymer layer, which contains PMMA and poly(methacrylic acid) (MAA), and is soft-baked again. Oxygen plasma is used to etch away any residual graphene on the underside of the copper foil. The copper foil is dissolved in a solution of ammonium persulfate. The polymer-supported graphene is then rinsed in a two-stage DI water bath, scooped onto a clean SiO₂/Si wafer, and baked on a hot plate to improve interfacial contact. Finally, the polymer layers are removed by immersing the wafer in warm acetone for at least ten hours [64].

Figure 5.1 shows optical images for two representative graphene samples, and corresponding Raman spectra are shown in Figure 5.2. The Type A sample is representative of approximately 15%, while Type B represents the other 85% of the approximately 40 measured samples grown and transferred using the method described above. Although the images differ somewhat, they both show monolayer graphene coverage with some polymer residue and/or small multilayer regions. The Raman spectra are nearly identical, suggesting the two types of graphene samples are more or less equivalent.

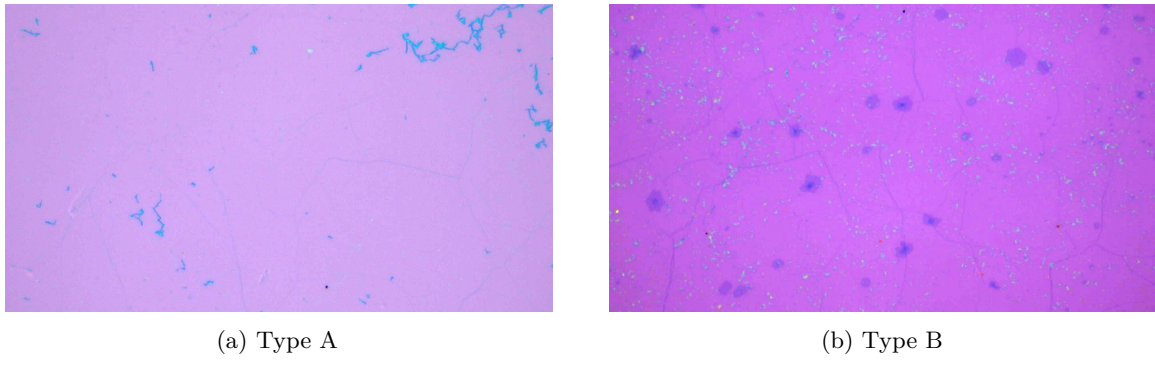


Figure 5.1: Optical micrograph of two representative graphene samples

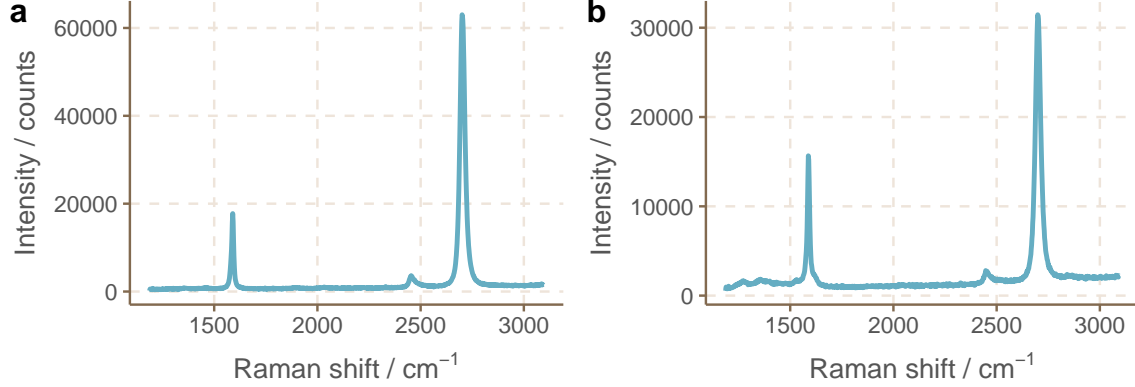


Figure 5.2: Raman spectra of two representative graphene samples

5.3 THz-TDS measurement of graphene

THz-TDS is a non-contact, non-destructive tool that allows us to extract electrical properties without actually doing a direct electrical measurement. We use the THz-TDS system in underside reflection geometry to analyze the light-matter interactions induced by picosecond pulses of THz light at the substrate-graphene-air interface as shown in Fig. 5.3. We describe the equations used to derive the electrical properties in the following sections.

5.4 Extracting complex properties of graphene

We use the transmission line model described in Chapter 4 on the THz-TDS measurements to extract the complex properties of graphene. At the air-substrate interface, equation (4.21) applies, and at

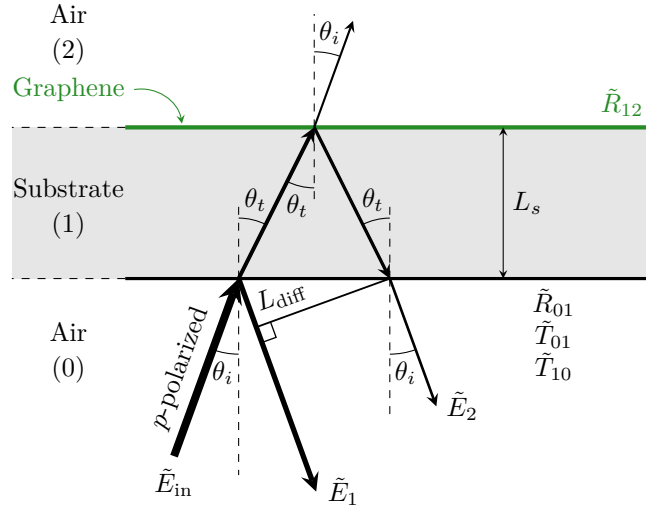


Figure 5.3: Ray diagram for THz light incident on the graphene-on-substrate system.

the substrate-graphene interface we have:

$$\tilde{\Gamma}_{12} = \frac{\tilde{Z}_s - \tilde{Z}_2}{\tilde{Z}_s + \tilde{Z}_2}, \quad (5.1)$$

$$\tilde{Z}_2 = \frac{1 + \tilde{\Gamma}_{12}}{1 - \tilde{\Gamma}_{12}} \tilde{Z}_s. \quad (5.2)$$

The graphene data shown in Figures 5.5 and 5.6 is the average taken for measurements over five random areas for each sample. The effective impedance, \tilde{Z}_2 , is the parallel combination of the graphene and air impedance. The complex impedance of graphene can be extracted from it, and is

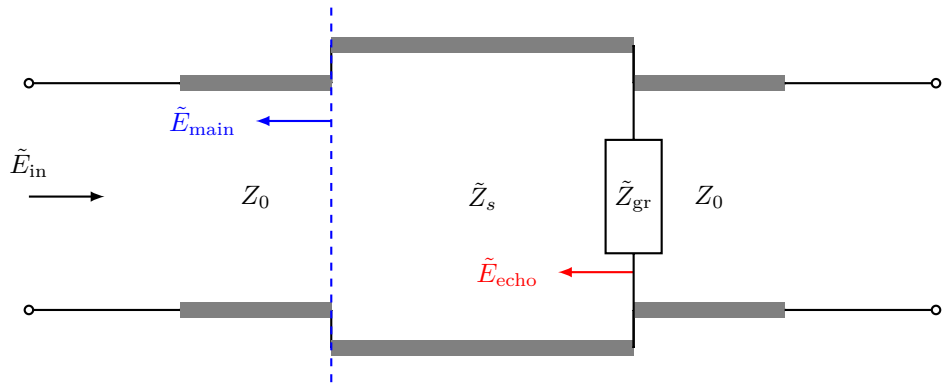


Figure 5.4: Transmission line model for graphene at the substrate-air interface.

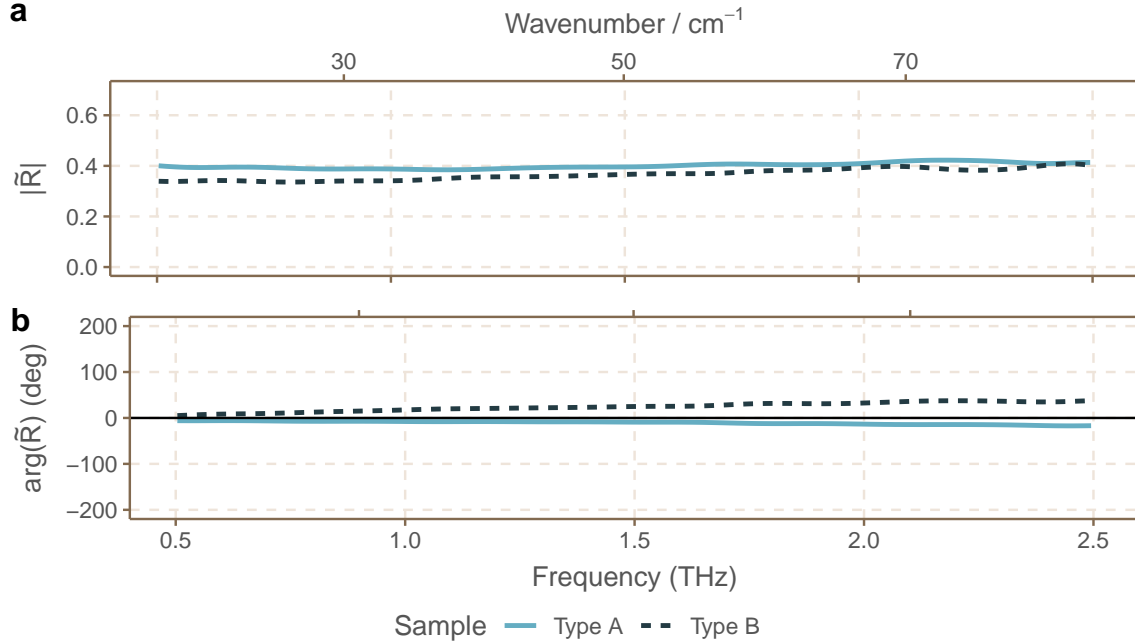


Figure 5.5: Complex reflection coefficients of the two representative graphene samples

given by

$$\tilde{Z}_{\text{gr}} = \frac{Z_0 - \tilde{Z}_2}{\tilde{Z}_2 Z_0}, \quad (5.3)$$

and the complex surface conductivity is given by,

$$\tilde{\sigma} = \frac{1}{\tilde{Z}_{\text{Gr}}} = \frac{Z_0 - \tilde{Z}_2}{Z_0 \tilde{Z}_2}. \quad (5.4)$$

5.5 Conductivity models

5.5.1 Kubo formalism

One of the uses of the Kubo formalism is to model the complete surface conductivity of graphene, taking into account both inter-band and intra-band transitions. Here we only consider the intra-band term because the energies corresponding to our THz frequency range are too low ($< k_B T \approx 26 \text{ meV}$) for any inter-band excitation in graphene. The Kubo formalism considering only intra-band contributions,

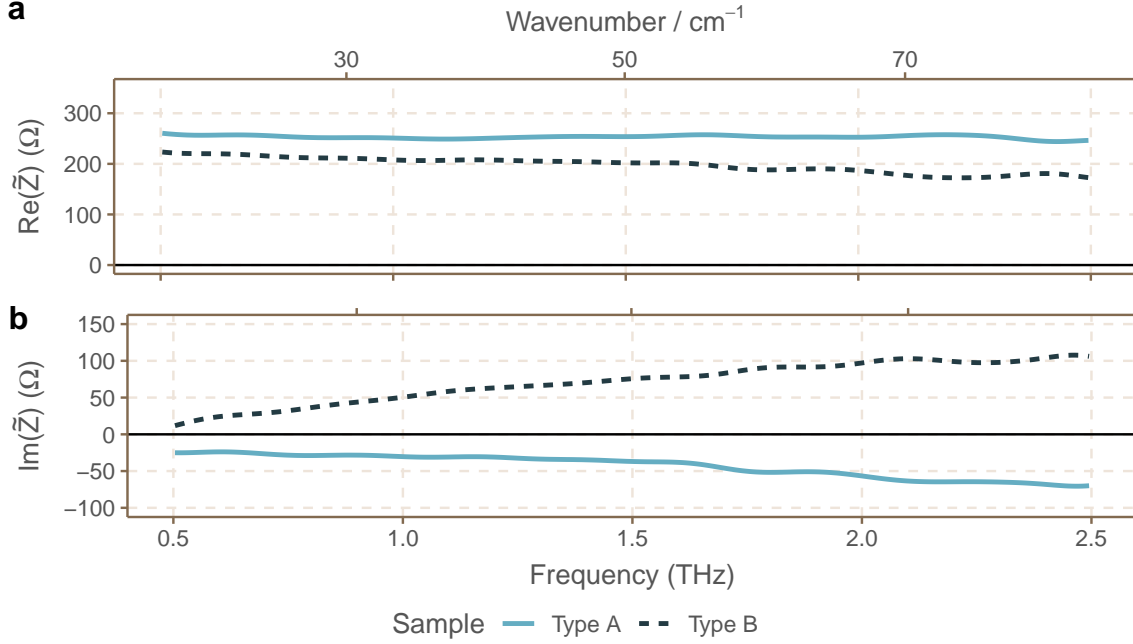


Figure 5.6: Complex impedance for the two representative graphene samples.

described in terms of Fermi energy E_F and scattering time τ , is given by [65, 66]:

$$\tilde{\sigma} = \frac{\tau}{1 - j\omega\tau} \left(\frac{2e^2}{\pi\hbar^2} k_B T \ln \left[2 \cosh \left(\frac{E_F}{2k_B T} \right) \right] \right). \quad (5.5)$$

This can be written as

$$\tilde{\sigma} = \frac{\tau}{1 - j\omega\tau} \left(\frac{2e^2}{\pi\hbar^2} k_B T \ln \left[2 \left(\frac{e^{E_F/2k_B T} + e^{-E_F/2k_B T}}{2} \right) \right] \right), \quad (5.6)$$

$$\tilde{\sigma} = \frac{\tau}{1 - j\omega\tau} \left(\frac{2e^2}{\pi\hbar^2} k_B T \ln \left[\left(\frac{e^{E_F/k_B T} + 1}{e^{E_F/2k_B T}} \right) \right] \right). \quad (5.7)$$

For graphene, $E_F \gg k_B T$. Therefore, $e^{E_F/k_B T} + 1 \approx e^{E_F/k_B T}$, and

$$\tilde{\sigma} = \frac{\tau}{1 - j\omega\tau} \left(\frac{2e^2}{\pi\hbar^2} k_B T \ln \left[\left(e^{E_F/2k_B T} \right) \right] \right), \quad (5.8)$$

$$\tilde{\sigma} = \frac{\tau}{1 - j\omega\tau} \left(\frac{2e^2}{\pi\hbar^2} k_B T \frac{E_F}{2k_B T} \right), \quad (5.9)$$

$$\tilde{\sigma} = \frac{\tau}{1 - j\omega\tau} \left(\frac{e^2}{\pi\hbar^2} E_F \right). \quad (5.10)$$

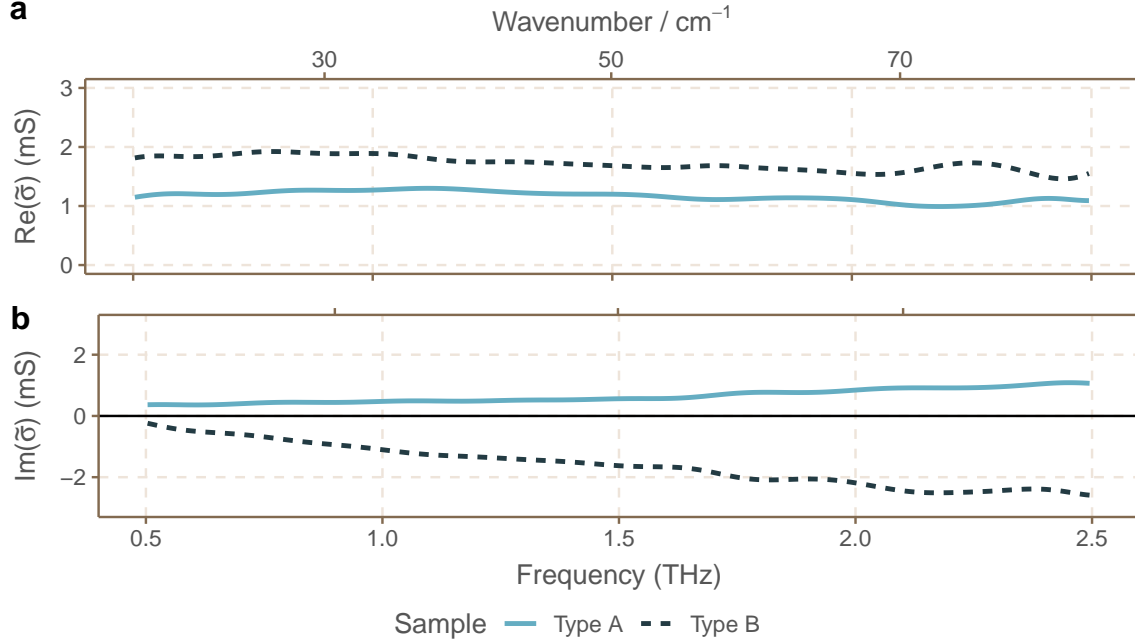


Figure 5.7: Complex conductivity for the two representative graphene samples.

According to [35],

$$E_F = \frac{\pi \hbar^2}{e^2} \frac{\sigma_{\text{dc}}}{\tau}, \quad (5.11)$$

where σ_{dc} is the DC conductivity of graphene. The complex conductivity becomes

$$\tilde{\sigma} = \frac{\tau}{1 - j\omega\tau} \frac{\sigma_{\text{dc}}}{\tau}, \quad (5.12)$$

thus, the Kubo formalism reduces to

$$\tilde{\sigma} = \frac{\sigma_{\text{dc}}}{1 - j\omega\tau}, \quad (5.13)$$

which is same as the Drude model for metals.

5.5.2 Drude model

In the Drude conductivity model, the dc conductivity term in equation (5.13) is given by,

$$\sigma_{\text{dc}} = \frac{Ne^2}{\tau m^*}, \quad (5.14)$$

where N is the surface charge carrier concentration and m^* is the effective mass of electrons. The Drude model assumes there to be no interactions among charge carriers, and that scattering is instantaneous and isotropic. This model works well to describe the surface conductivity of single crystal graphene [67]. However, graphene grown on commercial copper foils tends to be polycrystalline [67, 68]. Also, in the process of transferring graphene after growth onto the SiO_2 substrate, defects may occur in the form of folds, wrinkles, or tears. Scattering caused by such extended, line-shaped defects are far from being isotropic. Instead, they cause backscattering. This effect is especially poignant where the dimensions of the graphene crystal domains are similar to the mean free path of the carriers. In this case, significant backscattering occurs at the domain boundaries in addition to the point-like impurity scattering [67].

5.5.3 Drude–Smith model

In the simple Drude model, the scattering time, τ , gives the average time between all scattering events, and cannot differentiate between backscattering and isotropic scattering due to charge impurities. Therefore, to separate these two scattering mechanisms, we apply the Drude–Smith model [69] described by:

$$\tilde{\sigma} = \frac{\sigma_{\text{dc}}}{1 - j\omega\tau} \left[1 + \sum_{m=1}^{\infty} \frac{c_m}{(1 - j\omega\tau)^m} \right], \quad (5.15)$$

where c_m is the fraction of the original velocity retained by an electron after the m^{th} collision. If we consider only the first scattering event, i.e. $m = 1$, the Drude–Smith model can be written as:

$$\tilde{\sigma} = \frac{\sigma_{\text{dc}}}{1 - j\omega\tau} \left[1 + \frac{c_1}{1 - j\omega\tau} \right], \quad (5.16)$$

where $-1 \leq c_1 \leq 0$, and it describes the amount of backscattering after the first collision.

We apply both the Drude and Drude–Smith models to the extracted complex surface conductivity of Type A graphene. The fitting results are shown in Figure 5.8, and the model parameters obtained

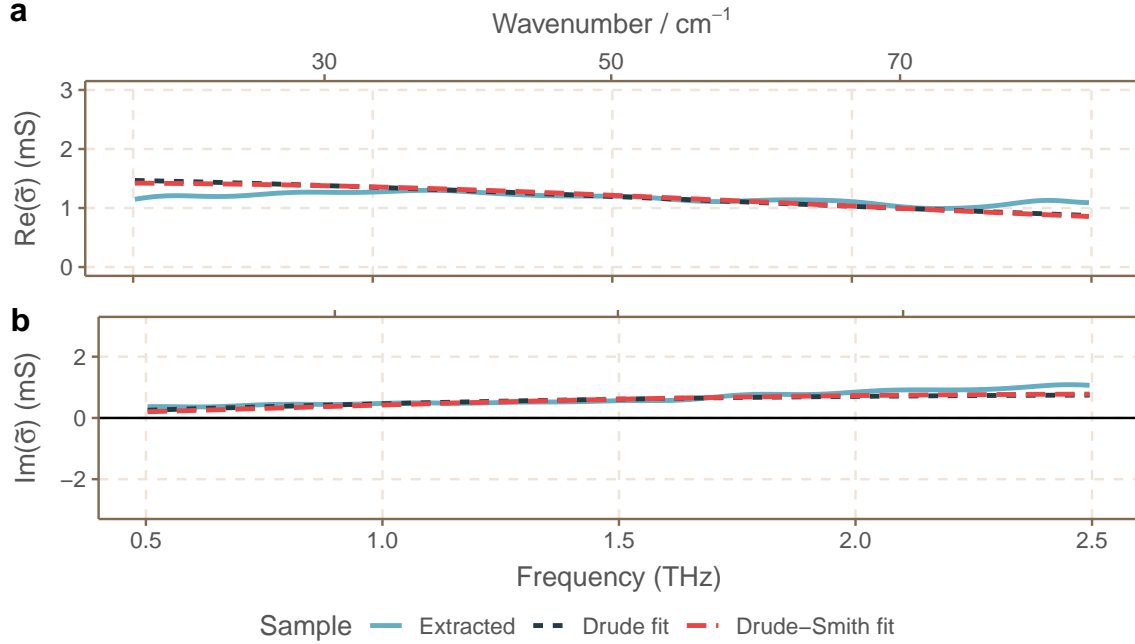


Figure 5.8: Drude and Drude-Smith model fitting to extracted complex surface conductivity of Type A graphene.

through the fitting are shown in Table 5.1. Based on the values obtained through the model fitting, we can estimate other properties of the graphene sample as described by the equations given below [32] and summarized in Table 5.1:

The Fermi energy can be expressed as:

$$E_F = \frac{1}{e} \frac{\pi \hbar^2}{e^2} \frac{\sigma_{dc}}{\tau}. \quad (5.17)$$

The surface charge carrier concentration is:

$$N = \frac{\pi \hbar^2}{e^4 v_F^2} \left(\frac{\sigma_{dc}}{\tau} \right)^2, \quad (5.18)$$

where $v_F \approx 1 \times 10^6 \text{ m s}^{-1}$ is the Fermi velocity of the electrons in graphene.

Lastly, the charge carrier mobility becomes:

$$\mu = \frac{\sigma_{dc}}{eN}. \quad (5.19)$$

Table 5.1: Extracted parameters for Type A graphene

Parameter	Drude model	Drude-Smith model
σ_{dc} (mS)	1.51	2.13
τ (fs)	54.48	83.06
c_1	0	-0.33
E_F (eV)	0.24	0.22
N (cm^{-2})	4.1×10^{12}	3.5×10^{12}
μ ($\text{cm}^2\text{V}^{-1}\text{s}^{-1}$)	2303	3800

5.5.4 Real part fitting

For a Type B graphene sample, we cannot fit the complex form of the Drude–Smith model because the imaginary part of the extracted complex surface conductivity is negative. However, by decomposing the Drude–Smith model into its real and imaginary parts [69], we can still estimate the dc conductivity and scattering time using

$$\text{Re}[\tilde{\sigma}] = \frac{\sigma_{dc}}{1 + \omega^2\tau^2} \left[1 + c_1 \frac{1 - \omega^2\tau^2}{1 + \omega^2\tau^2} \right]. \quad (5.20)$$

Figure 5.9 shows the results of fitting only the real part of the Drude–Smith model to both samples. Table 5.2 gives the model parameters obtained when only the real part of the Drude–Smith model is fit to the extracted complex surface conductivity of the representative graphene samples.

Table 5.2: Real part fitting parameters for both representative graphene samples

Parameter	Type A	Type B
σ_{dc} (mS)	2.02	1.89
τ (fs)	65.64	32.31
c_1	-0.4	-0.001
E_F (eV)	0.26	0.5
N (cm^{-2})	5.06×10^{12}	2.88×10^{15}
μ ($\text{cm}^2\text{V}^{-1}\text{s}^{-1}$)	2498	4

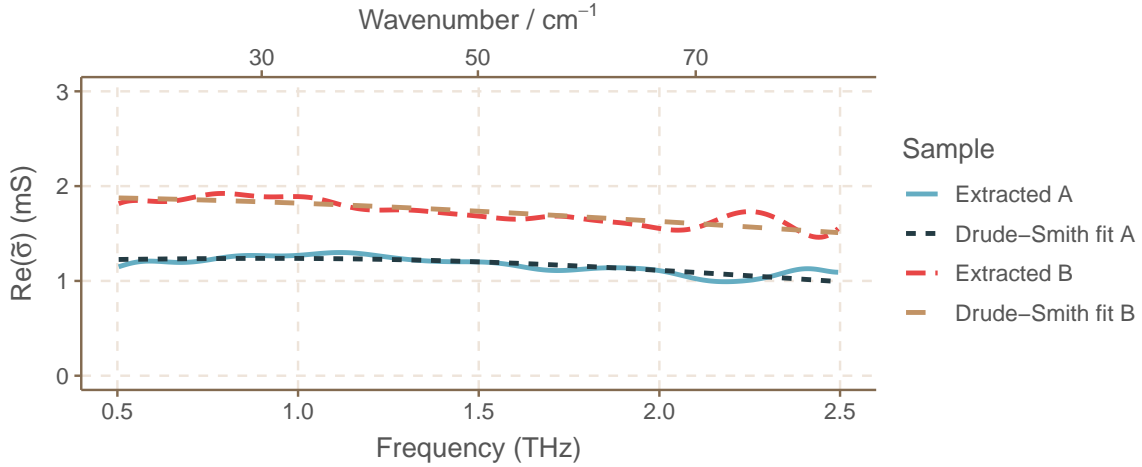


Figure 5.9: Drude–Smith model fitting to only the real part of the extracted complex surface conductivity for the representative graphene samples.

5.6 Complex dielectric function extraction

The extracted complex conductivity, particularly the real part, and the values extracted using the conductivity models are in agreement with the findings reported in [30–32, 68, 70–72]. Since results in existing literature are mainly obtained through measurement using transmission geometry, the phase uncertainty introduced due to substrate thickness variation makes the extracted imaginary part of the complex conductivity unreliable. While it is possible to still obtain the electrical parameters of graphene through conductivity model fitting of the real part only, as shown in the previous section, knowing the complex dielectric function is critically important for plasmonic applications.

From the complex surface conductivity, the complex dielectric function of graphene is extracted using:

$$\tilde{\epsilon} = 1 - j \frac{\tilde{\sigma}}{\epsilon_0 \omega t_f}, \quad (5.21)$$

$$\epsilon_r + j\epsilon_l = 1 - \frac{\text{Im}[\tilde{\sigma}]}{\epsilon_0 \omega t_f} + j \frac{\text{Re}[\epsilon_0 \tilde{\sigma}]}{\omega t_f}, \quad (5.22)$$

where $t_f = 1 \text{ nm}$ is assumed to be the graphene layer thickness. Figure 5.7a shows that Type B graphene sample has higher conductivity than Type A graphene sample. However, as seen in Figure 5.10, a Type A graphene has a negative relative permittivity, which is characteristic of a good conductor, whereas Type B graphene sample has a positive value, which is a characteristic of a

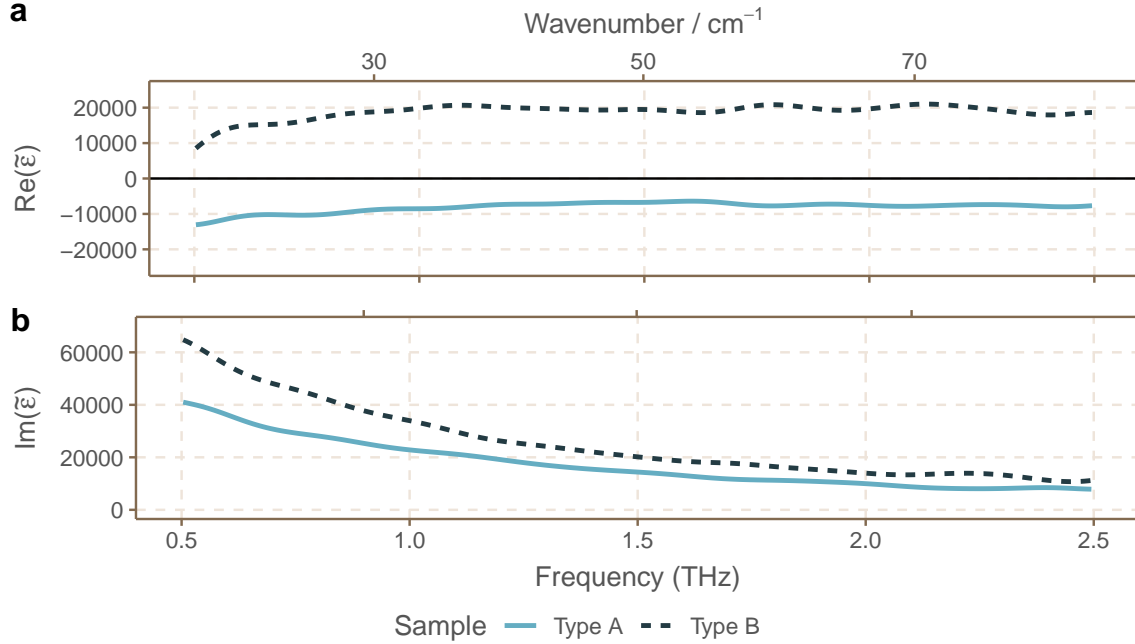


Figure 5.10: Complex dielectric function for two representative graphene samples

dielectric. The ability to ascertain this difference in graphene samples through THz-TDS has not been reported in the existing literature.

5.7 Importance to graphene-based plasmonics

In this chapter, we showed that relating the extracted complex surface conductivity to the complex dielectric function allows us to determine if a given graphene sample is capable of supporting surface plasmons. This property is critically important for plasmonics, and will determine the response of THz-frequency antenna structures, such as the bowtie antennas shown in Figure 5.11a. These antenna structures were designed to resonate at 1 THz. However, despite ascertaining through extraction of a negative dielectric function that this graphene sample shows conductor-like properties, no plasmonic resonance was observed when they were illuminated with THz radiation. This is observed in the form of a featureless reflectance spectrum shown in Figure 5.11b.

To understand why plasmons were not excited at the conductor–dielectric interface, we used the COMSOL Multiphysics platform to solve equations (5.5) and (5.21) and simulate the electric field inside a graphene patch antenna [59], which is only different in shape from the bowtie. Figure 5.12a uses a calculated value of the scattering time ($\tau = 0.5$ ps) [73], which shows the electric field of the

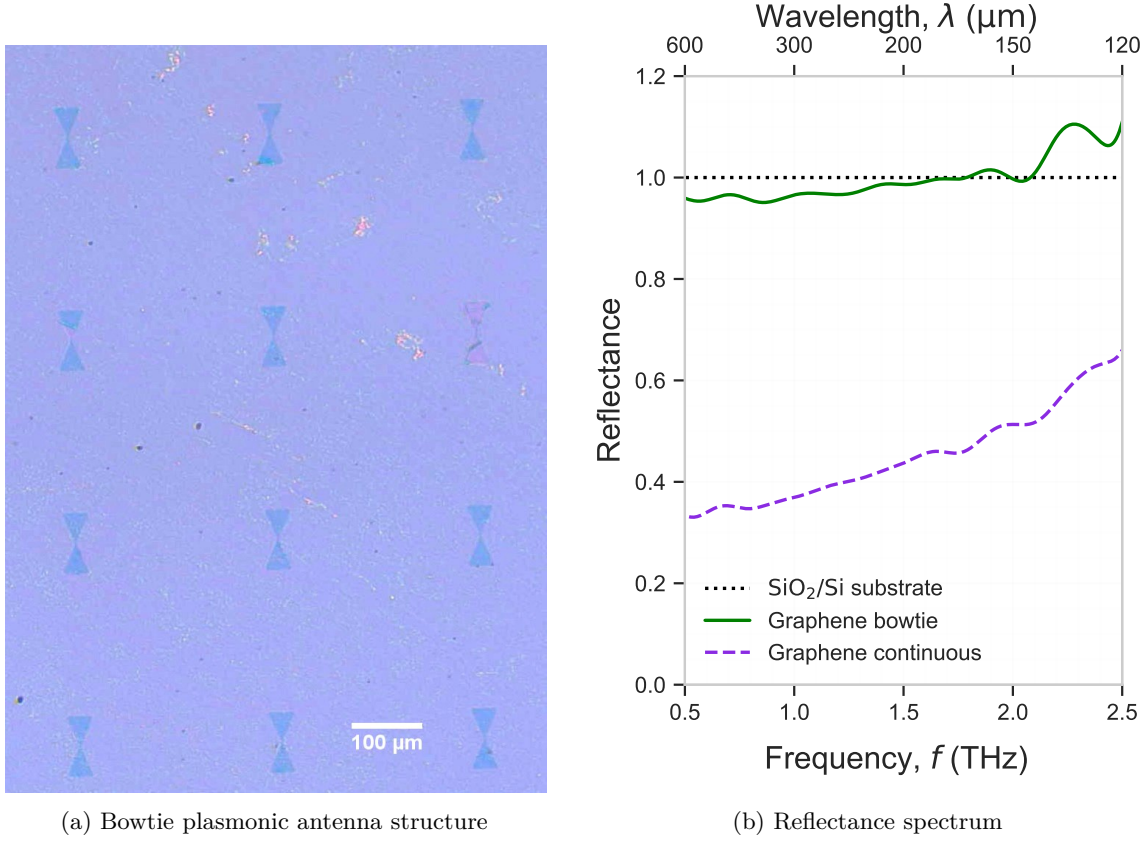


Figure 5.11: Graphene bowtie antenna array designed to resonate at 1 THz

surface plasmon being able to traverse the entire length of the patch. On the other hand, Fig. 5.12b shows that if the extracted value of τ is used, then the electric field of the surface plasmon decays very quickly.

5.8 Conclusion

Since THz-TDS measures the electric field, phase information is preserved when the THz light interacts with matter. This is shown as the argument of the reflection coefficient at the substrate-graphene-air interface. Using a transmission line model, we can quickly get the complex impedance of the graphene layer. The sign of the imaginary part of the complex impedance is opposite for the two representative graphene samples. This difference may be due to the quality of the graphene after the transfer process. If the imaginary part of the complex impedance is negative, then the real part of the complex dielectric function is also negative, which is expected of good conductors. On the

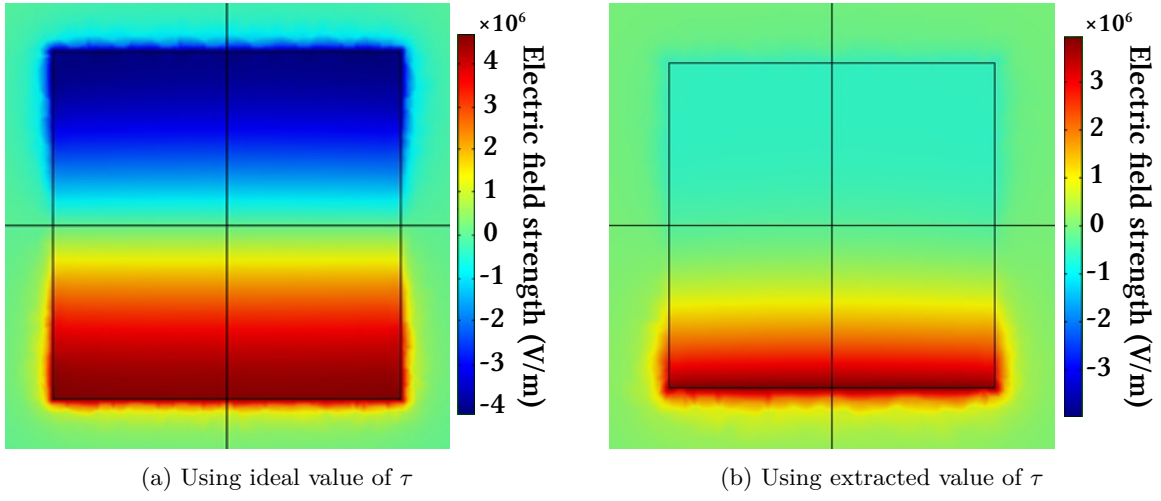


Figure 5.12: Electric field simulations for plasmon excitation in graphene patch antenna for different scattering times.

other hand, if the imaginary part of the complex impedance is positive, then the real part of the complex dielectric function is also positive, which is a property of a dielectric.

If graphene is to be used as the active layer in plasmonic applications, it is very important to know if the growth and transfer procedures produce a sample which shows conductor-like or dielectric-like properties. Other methods, such as optical characterization through Raman spectroscopy or electrical measurement using four-point probe, do not give this differentiation. The THz-TDS method presented here is not just better because of its non-contact, non-destructive nature, but other methods are insufficient when it comes to elucidating electrical and optical properties for plasmonic applications.

While the Drude and Drude-Smith conductivity models fit equally well, the backscattering parameter obtained through the Drude-Smith fitting gives a better indication of the scattering mechanisms in a given graphene sample. As seen in Table 5.1, the scattering time derived from the Drude model alone is much less than the value ascertained from the Drude-Smith model because the latter accounts for the line-defect scattering through its backscattering parameter. Therefore, the Drude-Smith model provides a somewhat clearer picture of the graphene quality. Finally, although the graphene samples that exhibit dielectric-like quality will be unsuitable for plasmonic applications, fitting only the real part of the Drude-Smith model allows us to still estimate the other electrical properties. The fact that the scattering time in comparison with the other sample is very short, and that the backscattering parameter is nearly zero, as shown in Table 5.2, is indicative of more charged impurities that increase isotropic scattering.

CHAPTER 6

Conclusion

In this work, we have demonstrated the versatility of the terahertz time-domain spectroscopy system in reflection geometry. When used in the upside reflection configuration, we can determine the substrate thickness very accurately through fractional illumination of the step-edge of the substrate. The results for this method were published in *Optics Express* [74]. Knowing the thickness very accurately, and *independent* of the refractive index, allows us to confidently characterize the substrate properties. This is critical when analyzing any sample placed on the substrate, as the effect of the substrate itself must be carefully accounted for.

We have also shown that, when used in the underside reflection geometry, the THz–TDS measurement allows us to characterize samples of diverse properties ranging from dielectric liquids, like water, to conducting two-dimensional crystals, like graphene. Through the use of the transmission line model described here, we can quickly and completely extract the complex impedance of a material to make a determination of its type, i.e., if it behaves like a conductor or a dielectric. By equating the transmission line reflection coefficient to the appropriate form of the Fresnel reflection coefficient, we have shown that we can extract the material’s complex conductivity or dielectric function using the complex impedance, which is easier to solve than the Fresnel counterpart. In the following sections we give some applications of our methods.

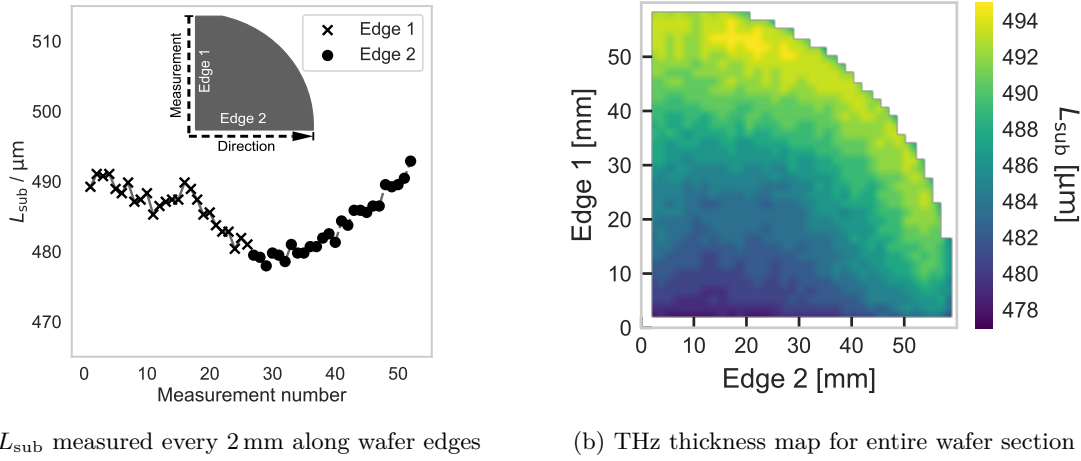


Figure 6.1: Time-domain spectroscopy and mapping measurement results

6.1 Thickness measurement application

We use the fractional reflection setup described in Chapter 2 to measure the thickness around the perimeter of a quadrant of a 100 mm-diameter undoped Si wafer. Figure 6.1a shows a series of measurements taken in increments of approximately 2 mm along the two straight edges of the wafer section (see inset). Based on these measurements, we find the thickness decreases as we move to the center of the wafer. Using these edge measurements to establish boundary conditions and an accurate value for n_{sub} , which we extract using the analysis method presented in Chapter 3, we then use the same measurement geometry to scan and obtain an accurate thickness map of the entire wafer section. The result is shown in Fig. 6.1b.

6.2 Complete determination of material type

We showed that describing the propagation of a THz beam through the substrate using a transmission line model helps to ascertain the properties of the material under test in a very straightforward manner. Figure 6.2 shows the complex impedance extracted for various materials using the equation:

$$\tilde{Z}_2 = \frac{1 + \Gamma_{12}}{1 - \Gamma_{12}} \tilde{Z}_s, \quad (6.1)$$

where $\Gamma_{12} = \tilde{R}_{12}$ is the reflection coefficient extracted from the transfer function formed using the echo pulse as the output and the main pulse as the input. The complex impedance of the substrate,

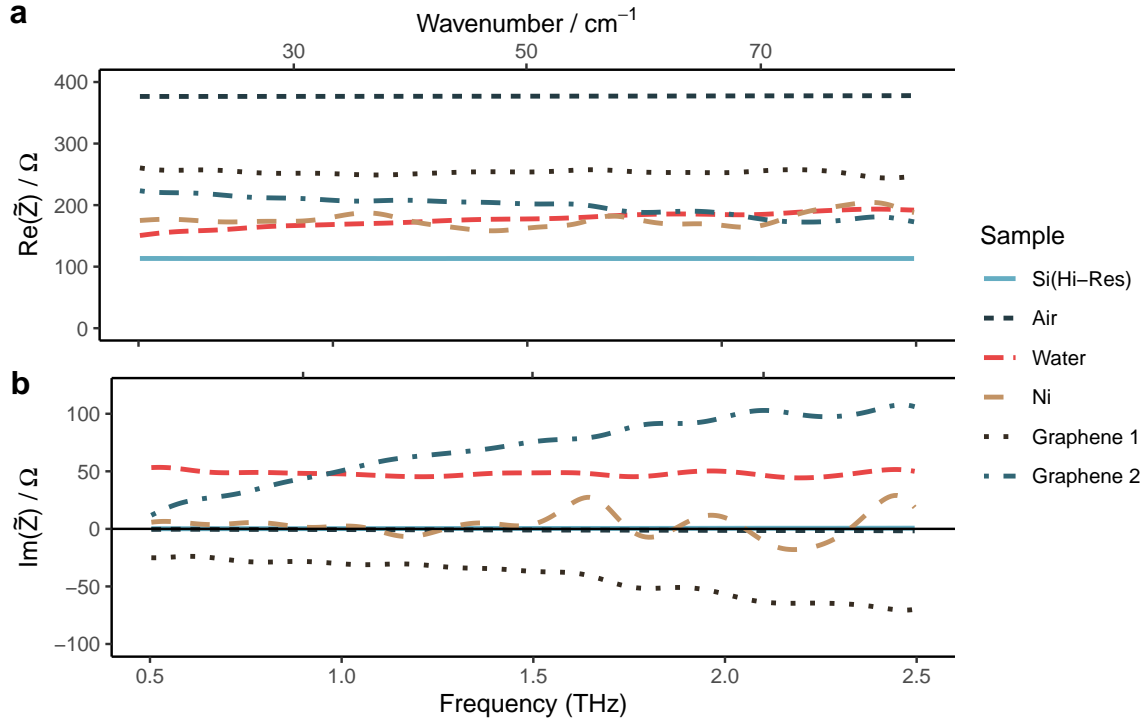


Figure 6.2: Complex impedances of different materials

\tilde{Z}_s , can be found by applying the above equation at the air–substrate interface, or by calculating as

$$\tilde{Z}_s = \frac{Z_0}{\tilde{n}_s \cos \theta_i}, \quad (6.2)$$

where $Z_0 \approx 377 \Omega$ is the free-space impedance, and \tilde{n}_s is the substrate complex refractive index calculated using the procedure described in Chapter 3.

A distinct advantage of THz–TDS over traditional electrical measurements is that, due to its non-contact nature, there is no risk of influencing or compromising the sample during measurement. Therefore, characterizing graphene through THz–TDS measurements helps us determine the complex dielectric properties, which are critically important for plasmonic applications. The clear difference seen in performing simulations using predicted, or theoretical, values versus real-world values accentuates the importance of obtaining graphene parameters under real-world conditions to guide antenna design and better evaluate expected performance. Moreover, the transmission line model approach has the ability to provide fast results, which is highly valued for industrial applications of THz metrology, as well as improved accuracy for THz plasmonics applications.

APPENDIX A

TAS7500TS THz-TDS Operating Procedure

Hardware settings

The transmission, underside reflection, and upside reflection geometries are shown in Figure A.1

Prior to initializing the system software, it is important to ascertain that the following hardware constraints are met:

- When used in the transmission or underside reflection configuration, the individual adapter plates need to be attached to the back of the emitter and detector optical modules before they are mounted on the backboard of the optical bench. These are shown in Figure A.2.
- When used in upside reflection configuration, the emitter and detector modules are mounted without the individual adapter plates on the Reflection Base Plate, shown in Figure A.3, which must be mounted first on the backboard of the optical bench.
- For the 4 THz standard emitter, the source and detector fiber optic and electrical cables are connected to the CH1 input of the Measurement Unit.
- For the 7 THz broadband emitter, the source and detector fiber optic and electrical cables are connected to the CH2 input of the Measurement Unit. This is a critical requirement because this emitter needs the laser power input to be 50 mW, which is only available on CH2.

Initializing the THz-TDS system

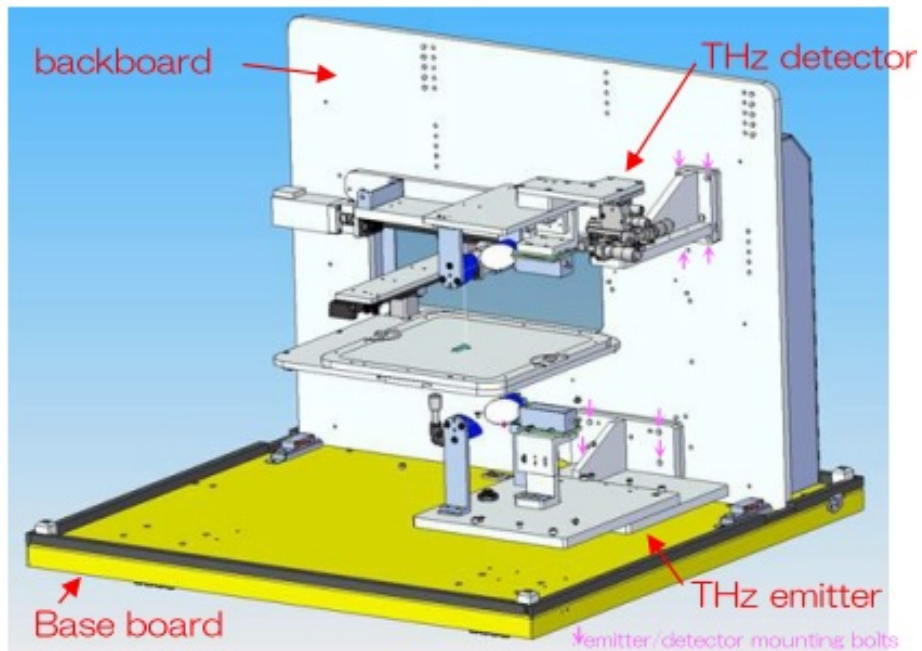
The TAS7500TS is a “turn-key” system. After switching it on, we need to wait at least one hour for the lasers to stabilize. The optical path length for the THz pulse is different for the two types of emitter setups. Therefore, each time one type of emitter is switched with another, we need to change the length of the delay fiber and perform a calibration check to set the trigger pulse. Having the optical bench in the transmission setup without the stage in place is highly recommended for this purpose.

This process involves performing the following steps in the given order:

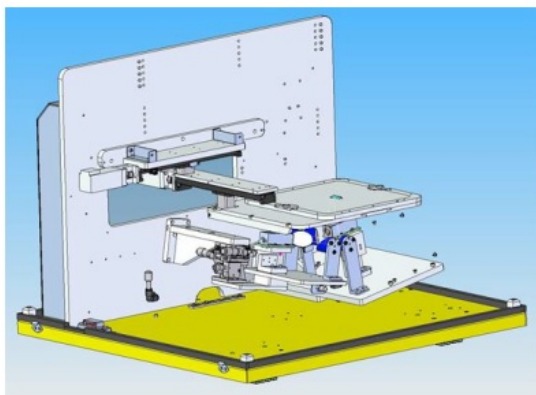
1. In the “THz Tuning & Monitoring” window, the Trigger Source is set to THz Wave, and the Cumulated Number is set to 1. Repeat Measurement is selected to monitor the THz wave.
2. The Trigger Level is adjusted until a waveform is displayed. Typically, a THz wave will be obtained between 10 mV and 65 mV. The notification box in the upper left corner will show “Triggered” in green.
3. The Trigger Position can be adjusted so that peak position of the THz wave is aligned with the vertical axis. This makes it easier to monitor its peak-to-peak value.
4. Adjust the micrometer screws on the detector module, until the maximum peak-to-peak value for the THz waveform is obtained. If the signal is too weak even after adjusting the screws, purge the optical bench for at least 30 minutes, and then try again.
5. Click on the Fiber Select option in the upper right corner. Click Replace under the Fiber Information section. Click Ok when asked for confirmation to replace the delay fiber length.
6. Wait for the system to stop the generation of optical pulses. This is known when the pump light on the front of the Measurement Unit is switched off.
7. *Ignore* the values displayed in the Selected Fiber section. Instead use the following values for each emitter type:
 - For the 4 THz standard emitter, the delay fiber length should be $0.25 + 0.125 = 0.375$ m.
 - For the 7 THz broadband emitter, the delay fiber length should be $0.5 + 0.125 = 0.625$ m.
8. Connect this delay fiber in the front panel of the Measurement Unit.
9. Click on the Completion button in the Fiber Information section, and wait for the system to start generating the optical pulses again. The pump light will switch on at this point.
10. Click on the Fitting Trigger button in the right hand corner to optimize the trigger delay device

for this particular delay length. When the system finishes the optimization process, it will display Pass in green under the Fitting Result section.

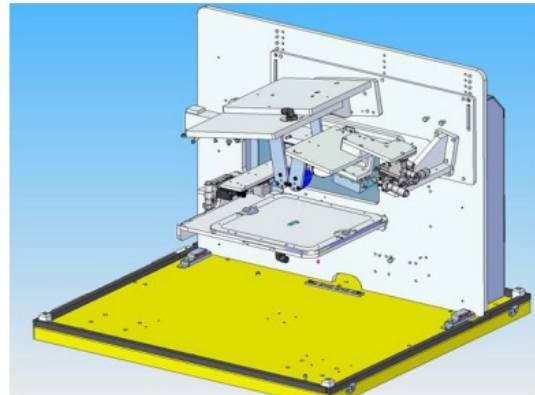
The result of a successful initialization process for each emitter type is shown in Figure A.4.



(a) Transmission setup



(b) Underside reflection setup



(c) Upside reflection setup

Figure A.1: Optical bench setup for all geometries

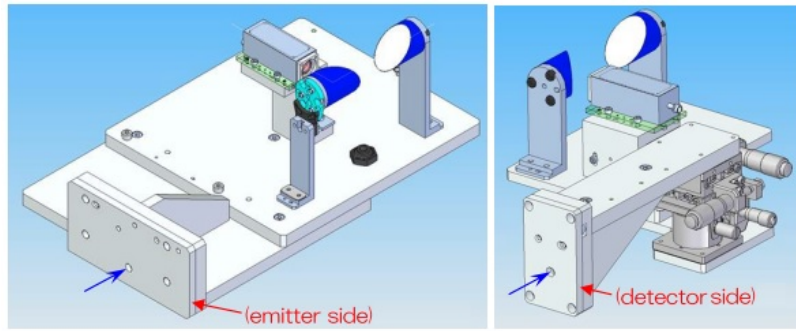


Figure A.2: Adapter plates attached to the emitter and detector modules

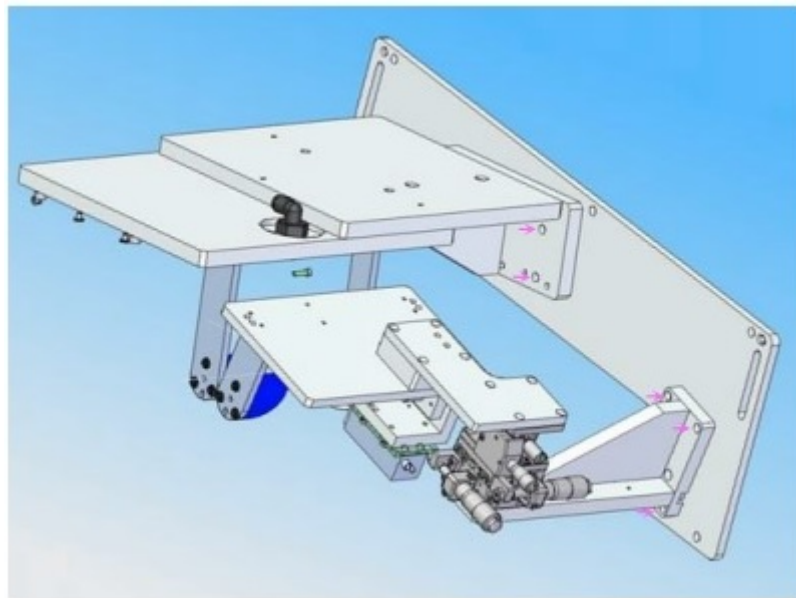
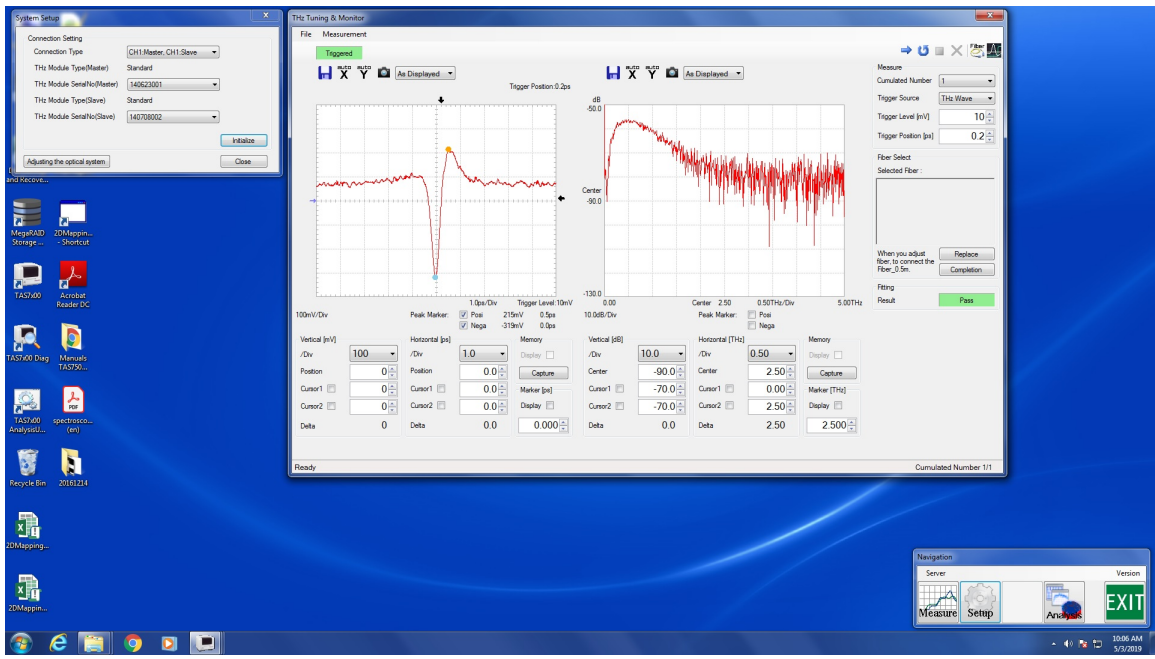
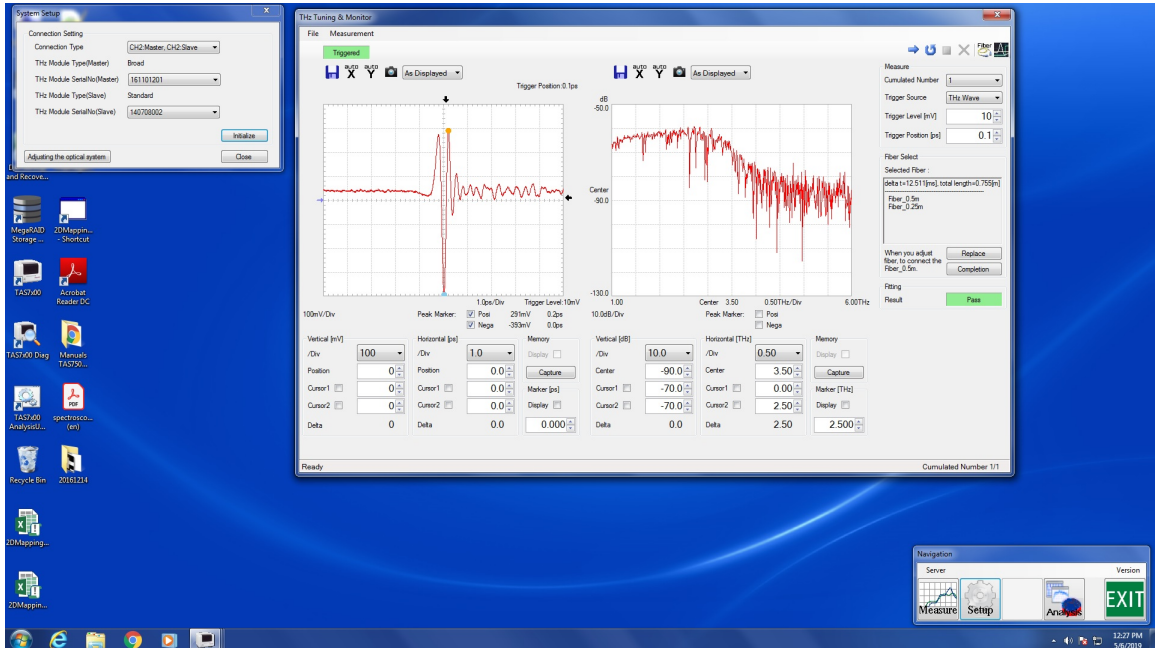


Figure A.3: Reflection base plate to be used in upside reflection geometry



(a) For the 4 THz standard emitter



(b) For the 7 THz broadband emitter

Figure A.4: Screenshot of successful initialization

APPENDIX B

Spot Size Measurement for the LiNbO₃ Emitter

For the LiNbO₃ waveguide-based emitter, the spectral range is 0.5 to 7 THz. We followed the same process as we did with the photoconductive antenna-based emitter. This method, known as the knife-edge method, is a commonly used technique to determine the spot size of an electromagnetic beam [45]. We took four measurements described below with a stainless steel blade covering one half of the 10 mm hole as we scanned the stage along the positive and negative directions for both the x - and y - axes.

Figure B.1 shows the normalized intensity profile of the beam for both directions along the x -axis. Similar results were obtained while scanning the stage in both directions along the y -axis. The derivative of the normalized intensity is plotted in Figure B.2 for the beam profile along the x -direction. A similar result is obtained for the beam profile along the y -direction. By fitting a Gaussian function corresponding to the above form, and extracting x_0 and r , we can calculate the beam radius , $2r$. The results are summarized in Table B.1.

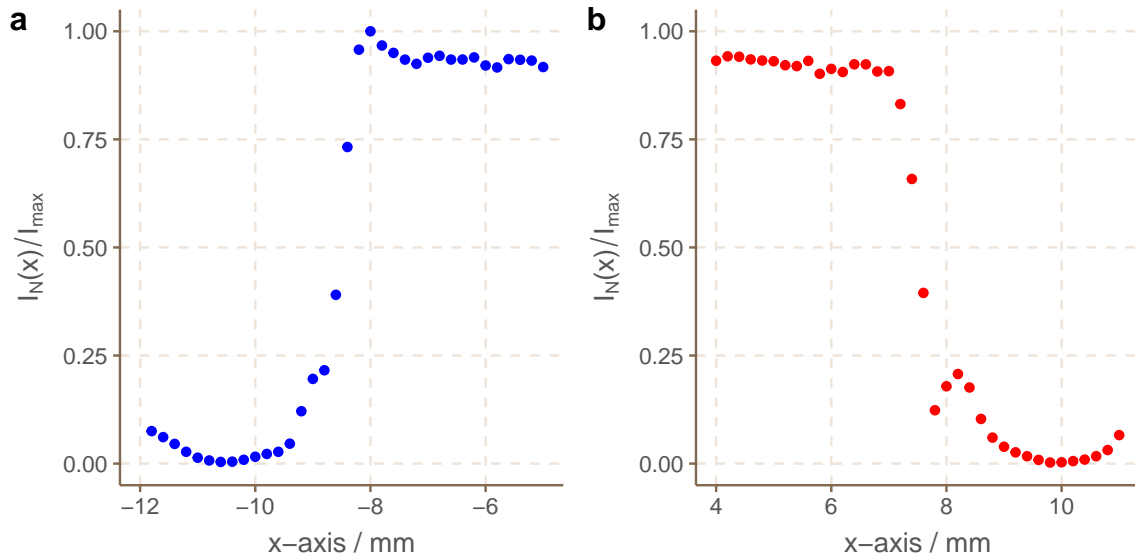


Figure B.1: Normalized intensity of the beam profile along the x -axis

Table B.1: THz beam spot size for the 4 THz emitter

Scan direction	Gaussian fit
	$2r(\text{mm})$
$+x$ axis	1.2
$-x$ axis	1.1
$+y$ axis	1.1
$-y$ axis	1.8
Average	1.3

For this emitter, the beam cannot be profiled smoothly because the beam radius is only three times larger than the 0.2 mm step size while scanning the stage.

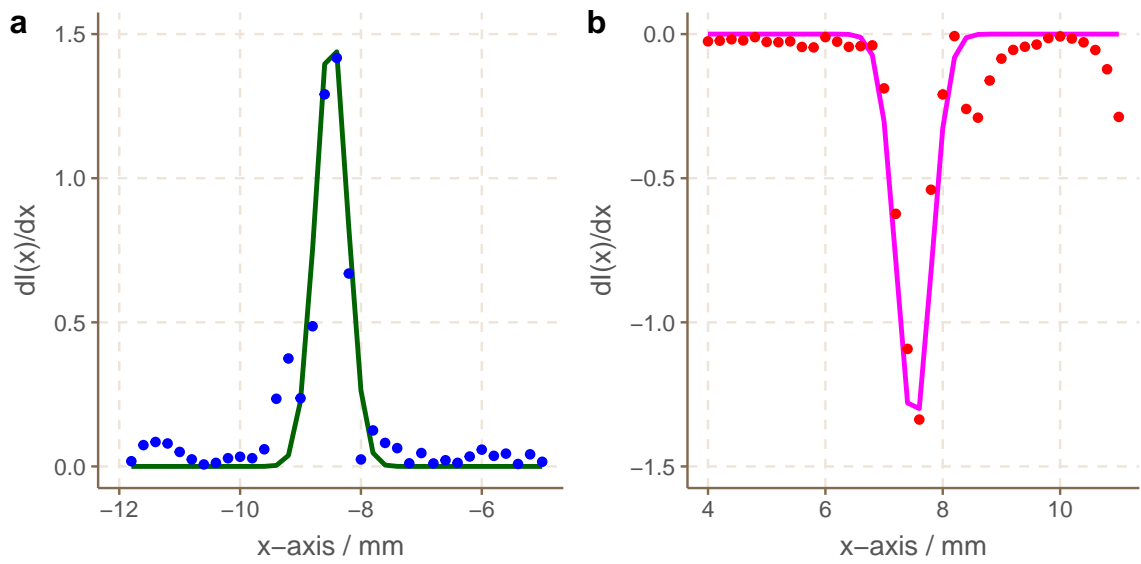


Figure B.2: The points are the derivative of the normalized intensity of the beam profile along the x -axis. The solid line denotes the Gaussian fit.

APPENDIX C

Python Code

The following code describes the functions defined for the analysis in this dissertation.

Define constants

```
from __future__ import division
import numpy as np
import pandas as pd
import matplotlib as mpl
import matplotlib.pyplot as plt
from scipy import signal
import seaborn as sb
import warnings
warnings.filterwarnings("ignore")

# Define constants
c = 3e11 # mm/s
epis_0 = 8.854e-15 # F/mm
Z0 = 1.0/(c*epis_0) # Ohm
h_bar = 1.054571800e-34 # Js/rad
#h_bar = 6.582118893e-16 # eV s
k_B = 1.3807e-23 # J/K
#k_B = 8.617342301e-5 # eV/K
v_F = 1e9 # mm/s Fermi velocity of electrons in graphene
```

```

T = 300 # K
e = 1.6e-19 # C
ts = 0.002
NFFT = 65536
timeX = np.arange(0,NFFT*ts,ts)
theta_deg = 10 # deg
theta_rad = np.deg2rad(theta_deg)
cos_theta = np.cos(theta_rad)
sin_theta = np.sin(theta_rad)
fs = 1/(NFFT*ts)
freqX_7THz = np.arange(0,7,fs)
omegaX_7THz = 2.0*np.pi*freqX_7THz*1e12
OmegaX = 2.0*np.pi*freqX_7THz

```

Import time domain data

```

# Import time domain data
def import_data(filename,show_plot=False):
    index_data, data_time, data_amp = np.loadtxt(filename,skiprows=111,delimiter=',',
                                                 unpack=True)

    if(show_plot==True):
        sb.set_style("whitegrid")
        fig, ax = plt.subplots(figsize=(7,7))
        ax.plot(data_time,data_amp,label='Imported Data')
        ax.get_xaxis().set_minor_locator(mpl.ticker.AutoMinorLocator())
        ax.get_yaxis().set_minor_locator(mpl.ticker.AutoMinorLocator())
        ax.grid(b=True,which='major',linewidth=1.0)
        ax.grid(b=True,which='minor',linewidth=0.5)
        ax.legend(loc='best',frameon=True,fontsize=18)
        plt.xlabel('time, $t$ [ps]',fontsize=20)
        plt.ylabel('Detected Signal, [V]',fontsize=20)
        fig.text(0.25, 0.9, '%s'%filename,fontsize = 18)
        plt.tick_params(labelsize=16)
        plt.show()

    return data_amp

```

Time domain analysis

Find main, stage, and echo peaks

```
# Detect peaks

def time_peak_detect(data,min_height,min_dist):
    data_dx = data[1:]-data[:-1]
    both, rise, fall = np.array([[],[],[]],dtype=int)
    rise = np.where((np.hstack((data_dx,0))<=0)&(np.hstack((0,data_dx))>0))[0]
    data_ind = rise
    data_ind = data_ind[data[data_ind]>=min_height]
    data_ind = data_ind[np.argsort(data[data_ind])][::-1]
    idel = np.zeros(data_ind.size,dtype=bool)
    for i in range(data_ind.size):
        if not idel[i]:
            idel = idel|(data_ind>data_ind[i]-min_dist)&(data_ind<=data_ind[i]+
                                                               min_dist)&(data[data_ind[i]]>
                                                               data[data_ind])
            idel[i] = 0
    data_ind = np.sort(data_ind[~idel])
    return data_ind

# Find all peaks

def all_time_peaks(data):
    data = data
    data_ind = time_peak_detect(data,min_height=0.014,min_dist=(1.5/ts))
    data_ind = data_ind.astype(int)
    data_val = data[data_ind]
    for i in range(data_ind.size-1):
        if(((data_ind[i+1]-data_ind[i])<(1.5/ts))):
            if(np.abs(data_val[i+1])<np.abs(data_val[i])):
                data_ind[i+1] = 0
            elif(np.abs(data_val[i+1])>=np.abs(data_val[i])):
                data_ind[i] = 0
            else:
                data_ind[i+1] = 0
                data_ind[i] = 0
    data_ind = data_ind[data_ind!=0]
    data_ind = data_ind[0:3]
```

```

data_ind = data_ind.astype(int)
data_peak_time = data_ind*ts
data_peak_value = data[data_ind]
return data_peak_time, data_peak_value

```

Find substrate thickness

```

# Define function to estimate thickness
def calc_params(peak_time):
    main_pk, stage_pk, echo_pk = peak_time
    dt_sm = stage_pk-main_pk
    L_est = (c*dt_sm*(1e-12))/(2.0*cos_theta)
    est_param = ([dt_sm,L_est*(1e3)])
    return est_param

```

Find positive and negative time domain peaks

```

# Detect peaks
def peak_detect(data,min_height,min_dist):
    data_dx = data[1:]-data[:-1]
    both, rise, fall = np.array([[],[],[]],dtype=int)
    rise = np.where((np.hstack((data_dx,0))<=0)&(np.hstack((0,data_dx))>0))[0]
    data_ind = rise
    data_ind = data_ind[data[data_ind]>=min_height]
    data_ind = data_ind[np.argsort(data[data_ind])][::-1]
    idel = np.zeros(data_ind.size,dtype=bool)
    for i in range(data_ind.size):
        if not idel[i]:
            idel = idel|(data_ind>data_ind[i]-min_dist)&(data_ind<=data_ind[i]+
                                                               min_dist)&(data[data_ind[i]]>
                                                               data[data_ind])
        idel[i] = 0
    data_ind = np.sort(data_ind[~idel])
    return data_ind

# Find all peaks
def all_time_peaks(data,pos_min_height,neg_min_height):

```

```

pos_data = data
neg_data = -data
pos_data_ind = peak_detect(pos_data, pos_min_height, min_dist=1000)
neg_data_ind = peak_detect(neg_data, neg_min_height, min_dist=1000)
pos_data_ind = pos_data_ind.astype(int)
data_ind = np.sort(np.concatenate((pos_data_ind, neg_data_ind)))
data_val = data[data_ind]
for i in range(data_ind.size-1):
    if(((data_ind[i+1]-data_ind[i])<(2/ts))):
        if(np.abs(data_val[i+1])<np.abs(data_val[i])):
            data_ind[i+1] = 0
        elif(np.abs(data_val[i+1])>=np.abs(data_val[i])):
            data_ind[i] = 0
        else:
            data_ind[i+1] = 0
            data_ind[i] = 0
data_ind = data_ind[data_ind!=0]
data_ind = data_ind[0:2]
data_ind = data_ind.astype(int)
data_peak_time = data_ind*ts
data_peak_value = data[data_ind]
return data_peak_time, data_peak_value

```

Estimate substrate parameters

```

# Define function to calculate time domain parameters for reflection measurements
def refl_time_params(data_pk_t,L_sub_const):
    main_pk_t, echo_pk_t = data_pk_t
    delta_t = echo_pk_t-main_pk_t
    n_est = np.sqrt((c*delta_t*(1e-12)/(2.0*L_sub_const))**2+sin_theta**2)
    cos_theta_t_est = c*delta_t*(1e-12)/(2.0*L_sub_const*n_est)
    theta_t_est = np.rad2deg(np.arccos(cos_theta_t_est))
    T_ASub_est = 2.0*cos_theta/(n_est*cos_theta+cos_theta_t_est)
    T_SubA_est = 2.0*n_est*cos_theta_t_est/(n_est*cos_theta+cos_theta_t_est)
    T_Sub_est = T_ASub_est*T_SubA_est
    R_ASub_est = (-n_est*cos_theta+cos_theta_t_est)/(n_est*cos_theta+cos_theta_t_est)
    R_SubA_est = (n_est*cos_theta-cos_theta_t_est)/(n_est*cos_theta+cos_theta_t_est)

```

```

est_params = ([n_est,theta_t_est,T_ASub_est,T_SubA_est,T_Sub_est,R_ASub_est,
              R_SubA_est])

return est_params

```

Shift time domain data

```

# Define function to shift time domain data

def shift_data(data1_peak_time,data2_peak_time,data2_amp,pos_min_height,
               neg_min_height):
    data1_main_peak_index = (data1_peak_time[0]/ts).astype(int)
    data2_main_peak_index = (data2_peak_time[0]/ts).astype(int)
    new_data2_amp = np.roll(data2_amp,data1_main_peak_index-data2_main_peak_index)
    new_data2_peak_time, new_data2_peak_value = all_time_peaks(new_data2_amp,
                                                               pos_min_height,neg_min_height)
    return new_data2_amp, new_data2_peak_time, new_data2_peak_value

```

Apply Hann window function

```

# Define window function

def Hann_win_func(data_peak_time,data_amp):
    if(len(data_peak_time)==1):
        ref_index = (data_peak_time/ts).astype(int)
        win_len = 5590
    else:
        main_peak_index, echo1_peak_index = (data_peak_time/ts).astype(int)
        win_len = (echo1_peak_index-main_peak_index)

def win_func(peak_index,exp_win_data=False):
    w = signal.tukey(win_len,1)
    w_before = np.zeros((peak_index+(0/ts)-len(w)/2).astype(int))
    w_after = np.zeros(NFFT-len(w_before)-len(w))
    window = np.concatenate((w_before,w,w_after))

    return window

if(len(data_peak_time)==1):
    ref_win = win_func(ref_index)
    ref_data = ref_win*data_amp
    return ref_win, ref_data
else:

```

```

    main_win = win_func(main_peak_index)
    echo_win = win_func(echo1_peak_index)
    main_data = main_win*data_amp
    echo_data = echo_win*data_amp
    data = main_data+echo_data
    data_win = main_win+echo_win
    return data_win, data

```

Frequency domain analysis

Apply Fourier transform

```

# Define function to apply Fourier transform to time domain data
def Fourier_transform(data):
    FourierY = np.fft.rfft(data,NFFT)/(len(timeX)-1)
    FourierY = FourierY [0:len(freqX_7THz)]
    return FourierY

```

Extract frequency domain data

```

# Define function to find frequency domain data
def Freq_data(FourierY):
    magY = np.abs(FourierY)
    phase = np.unwrap(np.angle(FourierY))
    inten = magY**2
    power = 10*np.log10(inten*NFFT)
    return magY, phase, power

```

Frequency calibration

Find reflectance

```

# Define function to find reflectance
def reflect(data1_FourierY,data2_FourierY,find_peaks=False):
    data1_inten = (np.abs(data1_FourierY))**2

```

```

data2_inten = (np.abs(data2_FourierY))**2
reflect = data2_inten/data1_inten
if(find_peaks==True):
    rl_pk_ind = peak_detect(reflect,min_height=0.08,min_dist=5)
    rl_th_ind = peak_detect(-reflect,min_height=-0.4,min_dist=5)
    return reflect, rl_pk_ind, rl_th_ind
else:
    return reflect

```

Calculate etalon frequencies

```

# Define function to filter peak and trough frequencies
def filter_freq(data,ind,low_lim,up_lim):
    del_ind = np.empty([])
    f = ind*fs
    for i in range(len(ind)):
        if((f[i]<low_lim)|(f[i]>up_lim)):
            del_ind = np.append(del_ind,i)
    new_ind = np.delete(ind,del_ind)
    f = new_ind*fs
    v = data[new_ind]
    return f, v

# Define function to find calculated peaks and troughs
def calc_pk_th(L_sub,n_sub,low_lim,up_lim):
    M = np.arange(1,len(freqX_7THz)+1)
    cos_theta_t = (np.sqrt(n_sub**2-sin_theta**2)/n_sub)
    pk_calc = (c/(2.0*n_sub*L_sub*cos_theta_t))*M/(1e12)
    th_calc = (c/(2.0*n_sub*L_sub*cos_theta_t))*(M+0.5)/(1e12)
    del_ind = np.empty([])
    for i in range(len(pk_calc)):
        if((pk_calc[i]<=low_lim)|(pk_calc[i]>=up_lim)):
            del_ind = np.append(del_ind,i)
    pk_calc = np.delete(pk_calc,del_ind)
    del_ind = np.empty([])
    for i in range(len(th_calc)):
        if((th_calc[i]<=low_lim)|(th_calc[i]>=up_lim)):
            del_ind = np.append(del_ind,i)

```

```

th_calc = np.delete(th_calc, del_ind)

return pk_calc, th_calc

```

Substrate characterization

Define transfer function

```

# Define transfer function

def trans_func(data1_FourierY,data2_FourierY):
    H = data2_FourierY / data1_FourierY
    return H

```

Find complex substrate properties

```

# Define function to find substrate refractive index

def sub_refract_index(H_EM,L_sub,ang):
    ang_rad = np.deg2rad(ang)
    H_EM_mag = np.abs(H_EM)
    H_EM_arg = np.unwrap(np.angle(H_EM))
    n_sub = np.sqrt(((c/(2.0*omegaX_7THz*L_sub))*(H_EM_arg+ang_rad))**2+sin_theta**2)
    cos_theta_t = (np.sqrt(n_sub**2-sin_theta**2))/n_sub
    L_eff = 2.0*L_sub*cos_theta_t
    T_ASub = (2.0*cos_theta)/(n_sub*cos_theta+cos_theta_t)
    T_SubA = (2.0*n_sub*cos_theta_t)/(n_sub*cos_theta+cos_theta_t)
    T_Sub = T_ASub*T_SubA
    kappa_sub = (-c/(omegaX_7THz*L_eff))*(np.log(H_EM_mag)-np.log(T_Sub))
    alpha_sub = (2.0*omegaX_7THz/c)*kappa_sub
    n_comp = n_sub-1j*kappa_sub      # True form is n-jk
    epis_comp = n_comp**2
    beta_L = (omegaX_7THz/c)*2.0*n_comp*L_sub*cos_theta_t
    return n_comp, beta_L, alpha_sub, epis_comp

```

Transmission line model analysis

Find complex reflection coefficient at substrate-sample interface

```
# Define function to find reflection coefficients
def refl_coeffs(H_EM,H_MR,n_comp,L_sub):
    cos_theta_t = (np.sqrt(n_comp**2-sin_theta**2))/n_comp
    T_ASub = (2.0*cos_theta)/(n_comp*cos_theta+cos_theta_t)
    T_SubA = (2.0*n_comp*cos_theta_t)/(n_comp*cos_theta+cos_theta_t)
    T_Sub = T_ASub*T_SubA
    R_ASub = (-n_comp*cos_theta+cos_theta_t)/(n_comp*cos_theta+cos_theta_t)
    R_s2 = H_EM*(R_ASub/T_Sub)*np.exp(1j*(omegaX_7THz/c)*2.0*n_comp*L_sub*cos_theta_t)
    return R_ASub, R_s2
```

Find complex impedance of the sample

```
# Define function to find complex impedance of the medium
def comp_Z(R,Z1):
    comp_Z2 = (((1.0+R)/(1.0-R))*Z1)
    return comp_Z2
```

Find complex properties of bulk sample

Find complex refractive index of sample from complex impedance

```
# Define function to extract refractive index from complex impedance
def comp_n_Z(Z_Y,Z_X,n_X):
    cos_theta_X = np.sqrt(n_X**2-sin_theta**2)/n_X
    Z_N = (Z_Y/Z_X)*(cos_theta_X/n_X)
    epis_Y = (1/(2.0*Z_N**2))*(1.0+np.sqrt(1.0-(2.0*Z_N*sin_theta)**2))
    n_Y = np.sqrt(epis_Y)
    return n_Y, epis_Y
```

Find complex refractive index of sample from Fresnel reflection coefficient

```
# Define function to find refractive index from reflection coefficient
def sam_prop(R_SiW,n_comp):
    R_SiW = R_SiW
    cos_theta_t = (np.sqrt(n_comp**2-sin_theta**2))/n_comp
    A_W = ((1.0-R_SiW)/(1.0+R_SiW))*(n_comp/cos_theta_t)
    sam_n_comp = np.sqrt((0.5*A_W*(A_W+np.sqrt(A_W**2-(4.0*sin_theta**2)))))

    epis_comp = (sam_n_comp)**2
    return sam_n_comp, epis_comp
```

Find complex properties of thin film

Find complex conductivity from complex impedance

```
# Define function to find complex conductivity from complex impedance
def sam_sigma_Z(Z):
    sigma = (Z0-Z)/(Z0*Z)
    return sigma*(1e3)
```

Find complex conductivity from Fresnel reflection coefficient

```
# Define function to find conductivity
def sam_conduct(n_comp,R_Sam):
    R_Sam = R_Sam
    cos_theta_t = (np.sqrt(n_comp**2-sin_theta**2))/n_comp
    Y_Sam = (((1.0-R_Sam)/(1.0+R_Sam))*(n_comp/cos_theta_t))-(1.0/cos_theta)
    sigma = Y_Sam/Z0
    return sigma*(1e3)
```

Find complex dielectric function from complex conductivity

```
# Define function to find dielectric function
def dielect_func(sigma,t_sam):
```

```

sigma = sigma*(1e-3)
sigma_real = np.real(sigma)
sigma_imag = np.imag(sigma)
epis_real = 1.0-(sigma_imag/(omegaX_7THz*epis_0*t_sam))
epis_imag = sigma_real/(omegaX_7THz*epis_0*t_sam)
return epis_real, epis_imag

```

Fitting conductivity models

Fit Drude model

```

# Define function to find simulated complex conductivity and Drude model parameters
def Drude_model(sigma,low_freq=0.5,high_freq=2.5):
    sigma = sigma*(1e-3)
    sigma_r = np.real(sigma)
    sigma_i = np.imag(sigma)

    # Define residual function to fit real and imaginary parts of Drude model
    def residual(params,OmegaX,sigma):
        sigma_dc, tau = params
        diff = sigma - (sigma_dc/(1-1j*(OmegaX*tau)))
        new_diff = np.zeros(sigma.size*2, dtype = np.float64)
        new_diff[0:new_diff.size:2] = diff.real
        new_diff[1:new_diff.size:2] = diff.imag
        return new_diff

    # Find fitted parameters using leastsq
    low_freq_ind = int(low_freq/fs)
    high_freq_ind = int(high_freq/fs)
    param_init = np.array([1.0,1.0])
    best_fit = least_squares(residual,param_init,args=(OmegaX[low_freq_ind:high_freq_ind],
                                                       sigma[low_freq_ind:high_freq_ind]),bounds=[[0.0,0.0],[np.inf,np.inf]))

    # Electrical parameters
    sigma_dc, tau = best_fit.x
    E_F = (np.pi*(h_bar**2)/(e**3))*(sigma_dc/tau)*(1e12)

```

```

N = (E_F/(e*((v_F*(1e-1))**2)))*(sigma_dc/tau)*(1e12)
mu = (sigma_dc/(e*N))

# Define complex Drude model
def complex_Drude(sigma_dc,tau):
    sigma_sim = sigma_dc/(1-1j*(OmegaX*tau))
    return sigma_sim*(1e3)

# Find simulated complex conductivity
sigma_sim = complex_Drude(sigma_dc,tau)

# Find goodness of fit
ss_err=((best_fit.fun)**2).sum()
ss_tot=((np.concatenate((sigma_r[low_freq_ind:high_freq_ind],sigma_i[low_freq_ind
                    :high_freq_ind])
-np.concatenate((sigma_r[low_freq_ind:high_freq_ind],sigma_i[low_freq_ind:
                    high_freq_ind])).mean())**2).sum()
r2 = 1-(ss_err/ss_tot)

Drude_params = ([sigma_dc*(1e3),tau*(1e3),r2])
Electrical_params = ([E_F,N,mu])
return sigma_sim, Drude_params, Electrical_params

```

Fit Drude-Smith model

```

# Define function to find simulated complex conductivity using Drude-Smith model
def Drude_Smith_model(sigma,low_freq=0.5,high_freq=2.5):
    sigma = sigma*(1e-3)
    sigma_r = np.real(sigma)
    sigma_i = np.imag(sigma)

    # Define residual function to fit real and imaginary parts of conductivity
    def residual(params,OmegaX,sigma):
        sigma_dc, tau, bs_c = params
        diff = sigma - ((sigma_dc/(1-1j*OmegaX*tau))*(1+(bs_c/(1-1j*OmegaX*tau))))
        new_diff = np.zeros(sigma.size*2, dtype = np.float64)
        new_diff[0:new_diff.size:2] = diff.real
        new_diff[1:new_diff.size:2] = diff.imag

```

```

    return new_diff

# Find fitted parameters using leastsq
low_freq_ind = int(low_freq/fs)
high_freq_ind = int(high_freq/fs)
param_init = np.array([1.0,1.0,0.0])
best_fit = least_squares(residual,param_init,args=(OmegaX[low_freq_ind:
                                                       high_freq_ind],
                                                    sigma[low_freq_ind:high_freq_ind]),bounds=[[0.0,0.0,-1.0],[np.inf,np.
inf,0.0]))

# Electrical parameters
sigma_dc, tau, bs_c = best_fit.x
E_F = (np.pi*(h_bar**2)/(e**3))*(sigma_dc/tau)*(1e12)
N = (E_F/(e*((v_F*(1e-1))**2)))*(sigma_dc/tau)*(1e12)
mu = (sigma_dc/(e*N))

# Define Drude-Smith model
def complex_Drude_Smith(sigma_dc,tau,c):
    sigma_sim = (sigma_dc/(1-1j*OmegaX*tau))*(1+(bs_c/(1-1j*OmegaX*tau)))
    return sigma_sim*(1e3)

# Find simulated complex conductivity
sigma_sim = complex_Drude_Smith(sigma_dc,tau,bs_c)

# Find goodness of fit
ss_err=((best_fit.fun)**2).sum()
ss_tot=((np.concatenate((sigma_r[low_freq_ind:high_freq_ind],sigma_i[low_freq_ind
                                                               :high_freq_ind]))
         -np.concatenate((sigma_r[low_freq_ind:high_freq_ind],sigma_i[low_freq_ind:
                                                               high_freq_ind])).mean())**2).sum()
r2 = 1-(ss_err/ss_tot)

Drude_Smith_params = ([sigma_dc*(1e3),tau*(1e3),bs_c,r2])
Electrical_params = ([E_F,N,mu])
return sigma_sim, Drude_Smith_params, Electrical_params

```

Fit only real part of Drude–Smith model

```
# Define function to find simulated complex conductivity using Drude-Smith model
def real_Drude_Smith_model(sigma,low_freq=0.5,high_freq=2.5):
    sigma = sigma*(1e-3)
    sigma_r = np.real(sigma)

    # Define residual function to fit real part of conductivity
    def residual(params,OmegaX,sigma_r):
        sigma_dc, tau, c = params
        diff = sigma_r - np.real((sigma_dc/(1-1j*OmegaX*tau))*(1+(c/(1-1j*OmegaX*tau))))
    return diff

    # Find fitted parameters using leastsq
    low_freq_ind = (np.round(low_freq/fs)).astype(int)
    high_freq_ind = (np.round(high_freq/fs)).astype(int)
    param_init = np.array([1.0,1.0,0.0])
    best_fit = least_squares(residual,param_init,args=(OmegaX[low_freq_ind:high_freq_ind],
                                                       sigma_r[low_freq_ind:high_freq_ind]),bounds=[[0.0,0.0,-1.0],[np.inf,np.inf,0.0]))

    # Electrical parameters
    sigma_dc, tau, c = best_fit.x
    E_F = (np.pi*(h_bar**2)/(e**3))*(sigma_dc/tau)*(1e12)
    N = (E_F/(e*((v_F*(1e-1))**2)))*(sigma_dc/tau)*(1e12)
    mu = (sigma_dc/(e*N))

    # Define Drude-Smith model
    def complex_Drude_Smith(sigma_dc,tau,c):
        sigma_sim = (sigma_dc/(1-1j*OmegaX*tau))*(1+(c/(1-1j*OmegaX*tau)))
    return sigma_sim*(1e3)

    # Find simulated complex conductivity
    sigma_sim = complex_Drude_Smith(sigma_dc,tau,c)

    # Find goodness of fit
    ss_err=((best_fit.fun)**2).sum()
```

```
ss_tot=((sigma_r[low_freq_ind:high_freq_ind]
         -sigma_r[low_freq_ind:high_freq_ind].mean())**2).sum()
r2 = 1-(ss_err/ss_tot)

Drude_Smith_params = ([sigma_dc*(1e3),tau*(1e3),c,r2])
Electrical_params = ([E_F,N,mu])
return sigma_sim, Drude_Smith_params, Electrical_params
```

Bibliography

- [1] T. Hochrein, “Markets, Availability, Notice, and Technical Performance of Terahertz Systems: Historic Development, Present, and Trends,” *Journal of Infrared, Millimeter, and Terahertz Waves*, vol. 36, no. 3, pp. 235–254, 2014.
- [2] C. Ronne, L. Thrane, P. O. Astrand, A. Wallqvist, K. V. Mikkelsen, and S. R. Keiding, “Investigation of the temperature dependence of dielectric relaxation in liquid water by THz reflection spectroscopy and molecular dynamics simulation,” *Journal of Chemical Physics*, vol. 107, no. 14, pp. 5319–5331, 1997.
- [3] H. Yada, M. Nagai, and K. Tanaka, “Origin of the fast relaxation component of water and heavy water revealed by terahertz time-domain attenuated total reflection spectroscopy,” *Chemical Physics Letters*, vol. 464, no. 4-6, pp. 166–170, 2008.
- [4] K. Shiraga, Y. Ogawa, T. Suzuki, N. Kondo, A. Irisawa, and M. Imamura, “Characterization of Dielectric Responses of Human Cancer Cells in the Terahertz Region,” *Journal of Infrared Millimeter and Terahertz Waves*, vol. 35, no. 5, pp. 493–502, 2014.
- [5] A. A. Angeluts, A. V. Balakin, M. G. Evdokimov, M. N. Esaulkov, M. M. Nazarov, I. A. Ozheredov, D. A. Sapozhnikov, P. M. Solyankin, O. P. Cherkasova, and A. P. Shkurinov, “Characteristic responses of biological and nanoscale systems in the terahertz frequency range,” *Quantum Electronics*, vol. 44, no. 7, pp. 614–632, 2014.
- [6] X. Yang, X. Zhao, K. Yang, Y. P. Liu, Y. Liu, W. L. Fu, and Y. Luo, “Biomedical Applications of Terahertz Spectroscopy and Imaging,” *Trends in Biotechnology*, vol. 34, no. 10, pp. 810–824, 2016.

-
- [7] J. Neu and C. A. Schmuttenmaer, "Tutorial: An introduction to terahertz time domain spectroscopy (THz-TDS)," *Journal of Applied Physics*, vol. 124, no. 23, 2018.
- [8] S. S. Dhillon, M. S. Vitiello, E. H. Linfield, A. G. Davies, M. C. Hoffmann, J. Booske, C. Paoloni, M. Gensch, P. Weightman, G. P. Williams, E. Castro-Camus, D. R. S. Cumming, F. Simoens, I. Escorcia-Carranza, J. Grant, S. Lucyszyn, M. Kuwata-Gonokami, K. Konishi, M. Koch, C. A. Schmuttenmaer, T. L. Cocker, R. Huber, A. G. Markelz, Z. D. Taylor, V. P. Wallace, J. A. Zeitler, J. Sibik, T. M. Korter, B. Ellison, S. Rea, P. Goldsmith, K. B. Cooper, R. Appleby, D. Pardo, P. G. Huggard, V. Krozer, H. Shams, M. Fice, C. Renaud, A. Seeds, A. Stohr, M. Naftaly, N. Ridler, R. Clarke, J. E. Cunningham, and M. B. Johnston, "The 2017 terahertz science and technology roadmap," *Journal of Physics D-Applied Physics*, vol. 50, no. 4, p. 49, 2017.
- [9] J. B. Baxter and G. W. Guglietta, "Terahertz Spectroscopy," *Analytical Chemistry*, vol. 83, no. 12, pp. 4342–4368, 2011.
- [10] M. van Exter, C. Fattinger, and D. Grischkowsky, "Terahertz time-domain spectroscopy of water vapor," *Opt. Lett.*, vol. 14, pp. 1128–1130, Oct 1989.
- [11] P. U. Jepsen, D. G. Cooke, and M. Koch, "Terahertz spectroscopy and imaging - Modern techniques and applications," *Laser & Photonics Reviews*, vol. 5, no. 1, pp. 124–166, 2011.
- [12] D. H. Auston, K. P. Cheung, and P. R. Smith, "Picosecond photoconducting hertzian dipoles," *Applied Physics Letters*, vol. 45, no. 3, pp. 284–286, 1984.
- [13] P. R. Smith, D. H. Auston, and M. C. Nuss, "Subpicosecond photoconducting dipole antennas," *IEEE Journal of Quantum Electronics*, vol. 24, pp. 255–260, Feb 1988.
- [14] R. Ulbricht, E. Hendry, J. Shan, T. F. Heinz, and M. Bonn, "Carrier dynamics in semiconductors studied with time-resolved terahertz spectroscopy," *Reviews of Modern Physics*, vol. 83, no. 2, pp. 543–586, 2011.
- [15] A. D. Koulouklidis, *Intense Broadband THz Fields from Laser-Plasma Interactions*. PhD thesis, University of Crete, 2016.
- [16] Y. Cai, I. Brener, J. Lopata, J. Wynn, L. Pfeiffer, J. B. Stark, Q. Wu, X. C. Zhang, and J. F. Federici, "Coherent terahertz radiation detection: Direct comparison between free-space electro-

-
- optic sampling and antenna detection," *Applied Physics Letters*, vol. 73, no. 4, pp. 444–446, 1998.
- [17] Y. C. Shen, P. C. Upadhyay, H. E. Beere, E. H. Linfield, A. G. Davies, I. S. Gregory, C. Baker, W. R. Tribe, and M. J. Evans, "Generation and detection of ultrabroadband terahertz radiation using photoconductive emitters and receivers," *Applied Physics Letters*, vol. 85, no. 2, pp. 164–166, 2004.
- [18] A. Nahata, D. H. Auston, T. F. Heinz, and C. Wu, "Coherent detection of freely propagating terahertz radiation by electro-optic sampling," *Applied Physics Letters*, vol. 68, no. 2, pp. 150–152, 1996.
- [19] K. Reimann, "Table-top sources of ultrashort THz pulses," *Reports on Progress in Physics*, vol. 70, pp. 1597–1632, sep 2007.
- [20] X. Yang, K. Yang, Y. Luo, and W. L. Fu, "Terahertz spectroscopy for bacterial detection: opportunities and challenges," *Applied Microbiology and Biotechnology*, vol. 100, no. 12, pp. 5289–5299, 2016.
- [21] W. L. Chan, J. Deibel, and D. M. Mittleman, "Imaging with terahertz radiation," *Reports on Progress in Physics*, vol. 70, no. 8, pp. 1325–1379, 2007.
- [22] W. Withayachumnankul, B. Ferguson, T. Rainsford, S. P. Mickan, and D. Abbott, "Simple material parameter estimation via terahertz time-domain spectroscopy," *Electronics Letters*, vol. 41, no. 14, p. 800, 2005.
- [23] F. G. Lionel Duvillaret and Jean-Louis Coutaz, "A Reliable Method for Extraction of Material Parameters in Terahertz Time-Domain Spectroscopy," *IEEE Journal of Selected Topics in Quantum Electronics*, vol. 2, no. 3, pp. 739–746, 1996.
- [24] F. G. Lionel Duvillaret and Jean-Louis Coutaz, "Highly precise determination of optical constants and sample thickness in terahertz time-domain spectroscopy," *Applied Optics*, vol. 38, no. 2, pp. 409–415, 1999.
- [25] W. Withayachumnankul, B. Ferguson, T. Rainsford, S. P. Mickan, and D. Abbott, "Material parameter extraction for terahertz time-domain spectroscopy using fixed-point iteration," 2005.

-
- [26] R. W. Ioachim Pupeza and Martin Koch, "Highly accurate optical material parameter determination with THz time-domain spectroscopy," *Optics Express*, vol. 15, no. 7, pp. 4335–4350, 2007.
 - [27] M. Scheller, "Real-time terahertz material characterization by numerical three-dimensional optimization," *Optics Express*, vol. 19, no. 11, pp. 10647–10655, 2011.
 - [28] U. Møller, *Terahertz spectroscopy applied to food model systems*. PhD thesis, 12 2009.
 - [29] T. I. Jeon and D. Grischkowsky, "Characterization of optically dense, doped semiconductors by reflection THz time domain spectroscopy," *Applied Physics Letters*, vol. 72, no. 23, pp. 3032–3034, 1998.
 - [30] E. Dadrasnia, F. Garet, D. Lee, J. L. Coutaz, S. Baik, and H. Lamela, "Electrical characterization of silver nanowire-graphene hybrid films from terahertz transmission and reflection measurements," *Applied Physics Letters*, vol. 105, no. 1, 2014.
 - [31] E. Dadrasnia and H. Lamela, "Terahertz conductivity characterization of nanostructured graphene-like films for optoelectronic applications," *Journal of Nanophotonics*, vol. 9, no. 1, p. 93598, 2015.
 - [32] P. R. Whelan, K. Iwaszczuk, R. Z. Wang, S. Hofmann, P. Boggild, and P. U. Jepsen, "Robust mapping of electrical properties of graphene from terahertz time-domain spectroscopy with timing jitter correction," *Optics Express*, vol. 25, no. 3, pp. 2725–2732, 2017.
 - [33] A. J. Fitzgerald, E. Pickwell-MacPherson, and V. P. Wallace, "Use of finite difference time domain simulations and Debye theory for modelling the terahertz reflection response of normal and tumour breast tissue," *PLoS One*, vol. 9, no. 7, p. e99291, 2014.
 - [34] K. Shiraga, T. Suzuki, N. Kondo, K. Tanaka, and Y. Ogawa, "Hydration state inside HeLa cell monolayer investigated with terahertz spectroscopy," *Applied Physics Letters*, vol. 106, no. 25, p. 5, 2015.
 - [35] Y. Zhou, Y. E, L. Zhu, M. Qi, X. Xu, J. Bai, Z. Ren, and L. Wang, "Terahertz wave reflection impedance matching properties of graphene layers at oblique incidence," *Carbon*, vol. 96, pp. 1129–1137, 2016.

-
- [36] D. van Mechelen, “An Industrial THz Killer Application?,” *Optics & Photonics News*, vol. 26, no. 11, pp. 16–18, 2015.
- [37] J. Z. J. Dai W. Zhang, and D. Grischkowsky, “Terahertz time-domain spectroscopy characterization of the far-infrared absorption and index of refraction of high-resistivity, float-zone silicon,” *Journal of Optical Society of America B*, vol. 21, no. 7, pp. 1379–1386, 2004.
- [38] C.-Y. Jen and C. Richter, “Sample Thickness Measurement with THz-TDS: Resolution and Implications,” *Journal of Infrared, Millimeter, and Terahertz Waves*, vol. 35, no. 10, pp. 840–859, 2014.
- [39] P. U. Jepsen, U. Møller, and H. Merbold, “Investigation of aqueous alcohol and sugar solutions with reflection terahertz time-domain spectroscopy,” *Optics Express*, vol. 15, no. 22, p. 14717, 2007.
- [40] S. Fan, E. P. J. Parrott, B. S. Y. Ung, and E. Pickwell-MacPherson, “Calibration method to improve the accuracy of THz imaging and spectroscopy in reflection geometry,” *Photonics Research*, vol. 4, no. 3, p. A29, 2016.
- [41] W. E. Lai, H. W. Zhang, Y. H. Zhu, and Q. Y. Wen, “A novel method of terahertz spectroscopy and imaging in reflection geometry,” *Applied Spectroscopy*, vol. 67, no. 1, pp. 36–39, 2013.
- [42] F. Huang, J. F. Federici, and D. Gary, “Determining thickness independently from optical constants by use of ultrafast light,” *Optics Letters*, vol. 29, no. 20, pp. 2435–2437, 2004.
- [43] M. Naftaly, “Metrology Issues and Solutions in THz Time-Domain Spectroscopy: Noise, Errors, Calibration,” *Ieee Sensors Journal*, vol. 13, no. 1, p. 10, 2013.
- [44] D. Choi, H. R. Park, and G.-s. Park, “Focused beam effect on measuring precise optical parameters of liquid water with terahertz time domain spectroscopy,” in *36th International Conference on Infrared, Millimeter, Terahertz Waves*, pp. 1–2, 2011.
- [45] M. A. C. de Araujo, R. Silva, E. de Lima, D. P. Pereira, and P. C. de Oliveira, “Measurement of Gaussian laser beam radius using the knife-edge technique: improvement on data analysis,” *Applied Optics*, vol. 48, no. 2, pp. 393–396, 2009.

-
- [46] J. Magnes D. and Hartke, J. and Fountain, M. and, Odera, L. Florence V., and Davis, “Quantitative and Qualitative Study of Gaussian Beam Visualization Techniques,” *ArXiv Physics e-prints*, 2008.
- [47] W. Withayachumnankul, H. Lin, S. P. Mickan, B. M. Fischer, and D. Abbott, “Analysis of measurement uncertainty in THz-TDS,” *Photonic Materials, Devices, and Applications II*, vol. 6593, no. June 2007, p. 659326, 2007.
- [48] W. Withayachumnankul, B. M. Fischer, H. Lin, and D. Abbott, “Uncertainty in terahertz time-domain spectroscopy measurement,” *Journal of the Optical Society of America B*, vol. 25, no. 6, p. 1059, 2008.
- [49] W. E. Lai, H. W. Zhang, Y. hua Zhu, Q. ye Wen, and Y. B. Ma, “Influence of Window Function on Characterization of Materials in Terahertz Spectroscopy,” *Spectroscopy Letters*, vol. 47, no. 8, pp. 590–596, 2014.
- [50] F. J. Harris, “On the Use of Windows with the Discrete Fourier Transform,” *Proceedings of the IEEE*, vol. 66, no. 1, pp. 51–83, 1978.
- [51] M. Naftaly and R. E. Miles, “Terahertz time-domain spectroscopy: A new tool for the study of glasses in the far infrared,” *Journal of Non-Crystalline Solids*, vol. 351, no. 40-42, pp. 3341–3346, 2010.
- [52] F. Pedrotti, L. A. Pedrotti, and L. S. Pedrotti, *Introduction to Optics*. Pearson, 3 ed., 2006.
- [53] K. J. Willis, S. C. Hagness, and I. Knezevic, “A generalized Drude model for doped silicon at terahertz frequencies derived from microscopic transport simulation,” *Applied Physics Letters*, vol. 102, no. 12, p. 4, 2013.
- [54] T. I. Jeon and D. Grischkowsky, “Nature of conduction in doped silicon,” *Physical Review Letters*, vol. 78, no. 6, pp. 1106–1109, 1997.
- [55] K.-S. L. Samuel P. Mickan Toh-Ming Lu, Jesper Munch, Derek Abbott, and X. C. Zhang, “Double modulated differential THz-TDS for thin film dielectric characterization,” *Microelectronics Journal*, vol. 33, pp. 1033–1042, 2002.
- [56] F. Ulaby and U. Ravaioli, *Fundamental of Applied Electromagnetics*. Pearson, 7 ed., 2014.

-
- [57] N. N. Rao, *Fundamentals of Electromagnetics for Electrical and Computer Engineering*. Pearson, 2009.
- [58] D. Zhou, E. P. J. Parrott, D. J. Paul, and J. A. Zeitler, “Determination of complex refractive index of thin metal films from terahertz time-domain spectroscopy,” *Journal of Applied Physics*, vol. 104, no. 5, p. 53110, 2008.
- [59] F. Vandrevala, A. Karmakar, J. M. Jornet, and E. Einarsson, “Graphene characterization using time-domain terahertz spectroscopy for plasmonic antenna design,” in *Proceedings of the 5th ACM International Conference on Nanoscale Computing and Communication - NANOCOM '18*, pp. 1–2, 2018.
- [60] P. Tassin, T. Koschny, and C. M. Soukoulis, “Graphene for terahertz applications,” *Science*, vol. 341, no. 6146, pp. 620–621, 2013.
- [61] A. K. Geim and K. S. Novoselov, “The rise of graphene,” *Nature Materials*, vol. 6, pp. 183–191, Mar. 2007.
- [62] E. H. Hwang and S. Das Sarma, “Dielectric function, screening, and plasmons in two-dimensional graphene,” *Physical Review B*, vol. 75, p. 205418, May 2007.
- [63] T. Otsuji, S. A. B. Tombet, A. Satou, H. Fukidome, M. Suemitsu, E. Sano, V. Popov, M. Ryzhii, and V. Ryzhii, “Graphene-based devices in terahertz science and technology,” *Journal of Physics D: Applied Physics*, vol. 45, no. 30, p. 303001, 2012.
- [64] A. Karmakar, F. Vandrevala, F. Gollier, M. A. Philip, S. Shahi, and E. Einarsson, “Approaching completely continuous centimeter-scale graphene by copolymer-assisted transfer,” *RSC Advances*, 2018.
- [65] L. A. Falkovsky and A. A. Varlamov, “Space-time dispersion of graphene conductivity,” *European Physical Journal B*, vol. 56, no. 4, pp. 281–284, 2007.
- [66] G. W. Hanson, “Dyadic Green’s functions and guided surface waves for a surface conductivity model of graphene,” *Journal of Applied Physics*, vol. 103, no. 6, p. 8, 2008.
- [67] P. Boggild, D. M. A. Mackenzie, P. R. Whelan, D. H. Petersen, J. D. Buron, A. Zurutuza, J. Gallop, L. Hao, and P. U. Jepsen, “Mapping the electrical properties of large-area graphene,” *2d Materials*, vol. 4, no. 4, p. 32, 2017.

-
- [68] J. D. Buron, D. H. Petersen, P. Boggild, D. G. Cooke, M. Hilke, J. Sun, E. Whiteway, P. F. Nielsen, O. Hansen, A. Yurgens, and P. U. Jepsen, “Graphene conductance uniformity mapping,” *Nano Lett*, vol. 12, no. 10, pp. 5074–5081, 2012.
- [69] N. Smith, “Classical generalization of the Drude formula for the optical conductivity,” *Physical Review B*, vol. 64, no. 15, 2001.
- [70] M. Y. Sho Ikeda and Chiko Otani, “Complex Optical Conductivity of Graphene Measured by Ultra broadband THz Time-domain Spectroscopic Ellipsometry,” in *39th International Conference on Infrared, Millimeter, and Terahertz waves*, IEEE, 2014.
- [71] J. D. Buron, F. Pizzocchero, B. S. Jessen, T. J. Booth, P. F. Nielsen, O. Hansen, M. Hilke, E. Whiteway, P. U. Jepsen, P. Boggild, and D. H. Petersen, “Electrically continuous graphene from single crystal copper verified by terahertz conductance spectroscopy and micro four-point probe,” *Nano Lett*, vol. 14, no. 11, pp. 6348–6355, 2014.
- [72] J. D. Buron, D. M. A. Mackenzie, D. H. Petersen, A. Pesquera, A. Centeno, P. Boggild, A. Zurutuza, and P. U. Jepsen, “Terahertz wafer-scale mobility mapping of graphene on insulating substrates without a gate,” *Optics Express*, vol. 23, no. 24, pp. 30721–30729, 2015.
- [73] N. Sule, K. J. Willis, S. C. Hagness, and I. Knezevic, “Terahertz-frequency electronic transport in graphene,” *Physical Review B*, vol. 90, no. 4, p. 45431, 2014.
- [74] F. Vandrevala and E. Einarsson, “Decoupling substrate thickness and refractive index measurement in THz time-domain spectroscopy,” *Optics Express*, vol. 26, no. 2, pp. 1697–1702, 2018.